A MULTISCALE ALMA STUDY OF PROTOPLANETARY DISKS IN OPHIUCHUS:
FROM OUTFLOWS TO SUBSTRUCTURES

A THESIS SUBMITTED BY

CAMILO IGNACIO GONZÁLEZ RUILOVA

TO THE

FACULTAD DE INGENIERÍA Y CIENCIAS
INSTITUTO DE ESTUDIOS ASTROFÍSICOS

In partial fulfillment of the requirements for the degree of
Doctor in Astrophysics

Supervisor: Lucas Cieza González
Co-Supervisor: Itziar de Gregorio-Monsalvo
Co-Supervisor: Alice Zurlo Alberton
Co-Supervisor: Álvaro Ribas Gómez

UNIVERSIDAD DIEGO PORTALES
Santiago, Chile
2024

ii

INSTITUTO DE ESTUDIOS ASTROFÍSICOS udp

FACULTAD DE INGENIERÍA Y CIENCIAS

Acta de Deliberación
Defensa de Tesis Doctoral

En Santiago, el 15 de Mayo de 2024 el Tribunal de Defensa de Tesis Doctoral compuesto por el profesor Lucas Cieza (UDP), Dra. Alice Zurlo (UDP), Dr. Carlo Manara (ESO, Alemania), Dra. Amelia Bayo (ESO, Alemania) y Dr. Alvaro Ribas (Universidad de Cambridge, Inglaterra), sobre la base del texto del proyecto, la exposición del doctorando y sus respuestas a las intervenciones de los miembros del tribunal, ha resuelto aprobar la tesis doctoral "A MULTISCALE ALMA STUDY OF PROTOPLANETARY DISKS IN OPHIUCHUS: FROM OUTFLOWS TO SUBSTRUCTURES", del doctorando Camilo Gonzalez.

Los miembros del Tribunal firman para constancia.

Lucas Cieza
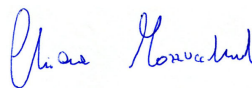
Supervisor, UDP

Alice Zurlo, UDP

Carlo Manara, ESO

Amelia Bayo

ESO

Alvaro Ribas

Universidad de Cambridge

Chiara Mazzucchelli

Ministro de Fe, UDP

UNIVERSIDAD DIEGO PORTALES

Abstract

Facultad de Ingeniería y Ciencias
Instituto de Estudios Astrofísicos

Doctor of Philosophy

A multiscale ALMA study of protoplanetary disks in Ophiuchus: from outflows to substructures

by Camilo González Ruilova

Los significativos avances tecnológicos de la última década han permitido un progreso sustancial en las observación y entendimiento de las proto estrellas y el disco de material que las rodea, consecuentemente dilucidando la formación planetaria y el potencial origen del sistema solar. Incluso sin observaciones claras o datos respecto de la formación estelar y planetaria, los humanos hemos estado analizando y proponiendo escenarios para el nacimiento y evolcuión de objetos cósmicos durante siglos. Sin embargo, según obtenemos mejores images e información de las proto estrellas jóvenes cercanas al sistema solar, muchos modelos e ideas teóricas han sido desafiadas. En esta tesis discutiremos varios escenarios de formación estelar y planetaria, para diferentes tipos de objetos jóvenes hayados en la región de formación estelar de Ofiuco, tales como proto enanas marrones y discos de transición. Utilizando datos de radio interferometría, estudiaremos el polvo y gas molecular que rodea estos objetos, observando diferentes escalas espaciales y midiendo, y describiendo, estructuras que alcanzan las miles de au. Estas observaciones revelarán la interacción de las proto estrellas con la nube molecular que las contiene, como también analizaremos en profundidad los fenómenos que ocurren dentro del disco protoplanetario a pocas au de la proto estrella.

En este estudio presentaremos la muestra más larga observada a la fecha de candidatas a proto enanas marrones. Con un total de 21 objetos, 16 exhiben discos de polvo, y 10 presentan extensas estructuras de gas molecular en las líneas de ^{12}CO, ^{13}CO, y $C^{18}O$ (2-1). Mientras que previos estudios han examinado los parámetros estelares o del disco con grandes muestras de estos objetos, solo existen estudios de objetos individuales en diferentes nubes moleculares con estructuras de gas > 500 au. Estas observaciones proveerán evidencia sólida para la comparación de variados modelos de formación de enanas marrones, y la posible formación de planetas alrededor de estas.

Adicionalmente, presentaremos el estudio del sistema estelar con las cavidades más grande y pequeña en la nube molecular de Ofiuco. El sistema ISO-Oph 2 presenta un disco de transición con dos anillos concéntricos no axisimétricos, una morfología poco común en est tipo de objetos. Además esta fuente se encuentra con una compañera lejana, a una separación de 240 au.

Esta compañera exhibe una cavidad de aproximadamente 2 au de diámetro, y la proto estrella huésped está en el régimen sub estelar, con una masa de ~ 0.08 M$_\odot$. Ambas fuentes comparten un puente de gas que las conecta, entregando evidencia de una posible interacción cercana previa.

Finalmente presentaremos futuros proyectos y observaciones relacionadas a las investigaciones ya mencionadas, con proyecciones para los telescopios e instrumentos que vendrán en el futuro.

UNIVERSIDAD DIEGO PORTALES

Abstract

Facultad de Ingeniería y Ciencias
Instituto de Estudios Astrofísicos

Doctor of Philosophy

A multiscale ALMA study of protoplanetary disks in Ophiuchus: from outflows to substructures

by Camilo González Ruilova

The significant technological advancements of the last decade have enabled substantial progress in the observation and understanding of protostars and the surrounding material disks, consequently shedding light on planetary formation and the potential origins of the solar system. Even without clear observations or data regarding stellar and planetary formation, humans have been analyzing and proposing scenarios for the birth and evolution of cosmic objects for centuries. However, as we obtain better images and information from young protostellar systems near the solar system, many models and ideas have been challenged. In this thesis, we will discuss various scenarios of stellar and planetary formation for different types of young object found in the star-forming region of Ophiuchus, such as proto-Brown dwarfs and transition disks. Utilizing radio interferometric data, we will study the dust and molecular gas surrounding these objects, observing different spatial scales and measuring and describing structures spanning thousands of au. These observations will reveal the interaction of protostars with the molecular cloud hosting them, as well as analyze in-depth the phenomena occurring within protoplanetary disks a few au from the protostar.

We will present the largest sample observed to date of proto-Brown Dwarf candidates. With a total of 21 objects, 16 exhibit dust disks, and 10 feature extended molecular gas structures in ^{12}CO, ^{13}CO, and C^{18}O (2-1) lines. While previous studies have examined stellar or disk parameters with large samples of these objects, individual studies in different molecular clouds with gas structures > 500 au exist. These observations will provide strong evidence for comparison with various models of Brown Dwarf formation and the possible formation of planets around them.

Furthermore, we will present the study of the system with the largest and shortest cavities in the Ophiuchus molecular cloud. The system ISO-Oph 2 features a transition disk with two non-axisymmetric concentric rings, an uncommon morphology for such objects. Additionally, it is accompanied by a wide companion at a separation of 240 au. This companion exhibits a cavity of approximately 2 au in diameter, and the host protostar is in the sub-stellar regime, with a mass of $\sim 0.08\,\mathrm{M}_\odot$. Both sources share a gas bridge connecting them, providing evidence of a possible closer previous interaction.

Finally, we will present future projects and observations for the aforementioned research, with projections for telescopes and instruments yet to come.

Contents

List of Figures

List of Tables

List of Abbreviations

ACA = **A**tacama **C**ompact **A**rray
ALMA = **A**tacama **L**arge **M**illimeter/submillimeter **A**rray
BD = **B**rown **D**warf
CMF = **C**ore **M**ass **F**unction
CPD = **C**ircum**P**lanetary **D**isk
CTTS = **C**lassical **T**-**T**auri **S**tar
DSHARP = **D**isk **S**ubstructures **H**igh **A**ngular **R**esolution **P**roject
FS = **F**lat **S**pectrum
HST = **H**ubble **S**pace **T**elescope
IMF = **I**nitial **M**ass **F**unction
ISM = **I**nter**S**tellar **M**edium
IR = **I**nfra**R**ed
JWST = **J**ames **W**ebb **S**pace **T**elescope
LCO = **L**as **C**ampanas **O**bservatory
MHD = **M**agneto**H**ydro**D**ynamics
NIR = **N**ear **I**nfra**R**ed
ODISEA = **O**phiuchus **DI**sc **S**urvey **E**mploying **A**LMA
PPD = **P**roto**P**lanetary **D**isk
rms = **r**oot **m**ean **s**quare
SED = **S**pectral **E**nergy **D**istribution
SFR = **S**tar-**F**orming **R**egion
SNR = **S**ignal-to-**N**oise **R**atio
SpT = **S**pectral **T**ype
VLA = **V**ery **L**arge **A**rray
VLT = **V**ery **L**arge **T**elescope

Physical Constants

Astronomical Unit	$au = 1.49598 \times 10^{11}\,\mathrm{m}$
Speed of Light	$c_0 = 2.99792 \times 10^{8}\,\mathrm{m\,s^{-1}}$
Mass of Jupiter	$M_{Jup} = 1.89813 \times 10^{27}\,\mathrm{kg}$
Mass of Sun	$M_{\odot} = 1.9891 \times 10^{30}\,\mathrm{kg}$
Mass of Earth	$M_{\oplus} = 5.9722 \times 10^{24}\,\mathrm{kg}$
Parsec	$pc = 3.0857 \times 10^{16}\,\mathrm{m}$
Boltzmann constant	$k = 1.380649 \times 10^{-23}\,\mathrm{J\,K^{-1}}$
Mass of Hydrogen atom	$m_H = 1.6735575 \times 10^{-27}\,\mathrm{kg}$
Pi	$\pi = 3.14159265...$
Jansky	$Jy = 1 \times 10^{-26}\,\mathrm{W\,m^{-2}\,Hz^{-1}}$

Dedicated to my brother, Cristóbal. . .

Chapter 1

Introduction

1.1 Overview

Stellar formation, and specifically the subsequent planetary formation, has been a hot topic for several decades. These gas and dust-filled environments in which planetary systems like the solar system form are challenging to observe without the pertinent technology that has been developed since the late twentieth century. A more terrestrial analogy for the challenges of observing and analyzing protostars and Young Stellar Objects (YSOs) is akin to trying to see through a sandstorm in the desert or identify living beings amidst a forest fire—scenarios much more dire than understanding the formation of stars and planets in the universe, but which entail similar technological challenges on different scales.

The development of telescopes and instruments capable of seeing through these optically diffuse environments has allowed for a significant leap in the understanding of early celestial object formation processes. Examples of these megaprojects across different wavelengths, not only installed on Earth's surface, include the Very Large Telescope (VLT, 1998), the Spitzer Space Telescope (Spitzer, 2003), and the James Webb Space Telescope (JWST, 2022) in the Infrared (IR), as well as the Karl G. Jansky Very Large Array (VLA, 1980), the SubMillimeter Array (SMA, 2003), and the Atacama Large Millimeter/submillimeter Array (ALMA, 2013) in (sub)millimeter (mm) wavelengths.

There are still many unanswered questions and physical phenomena to understand about stellar evolution in early stages and planetary formation. However, there has been a consensus on the big picture of these processes for many years, and future observations and new technologies will help refine and complete our understanding. In Figure 1.1, an illustrative scheme of the evolutionary stages of planetary systems is shown, starting from the dense gas and dust cloud. Through gravitational and viscous phenomena, clumps of material with overdensities are generated, where these primordial building blocks will join to form the first dense cores. After accruing sufficient material, they will initiate combustion, forming the first stars. After several intermediate steps, the protostars will have obtained most of their final mass, leaving only a circumstellar or protoplanetary disk (PPDs), where the first protoplanets will form, sharing the remaining material with the protostar. Finally, almost all the dust and gas in the disk will become trapped in the star, the planets, comets, and asteroid belts, culminating in an evolved and stable system analogous to the solar system.
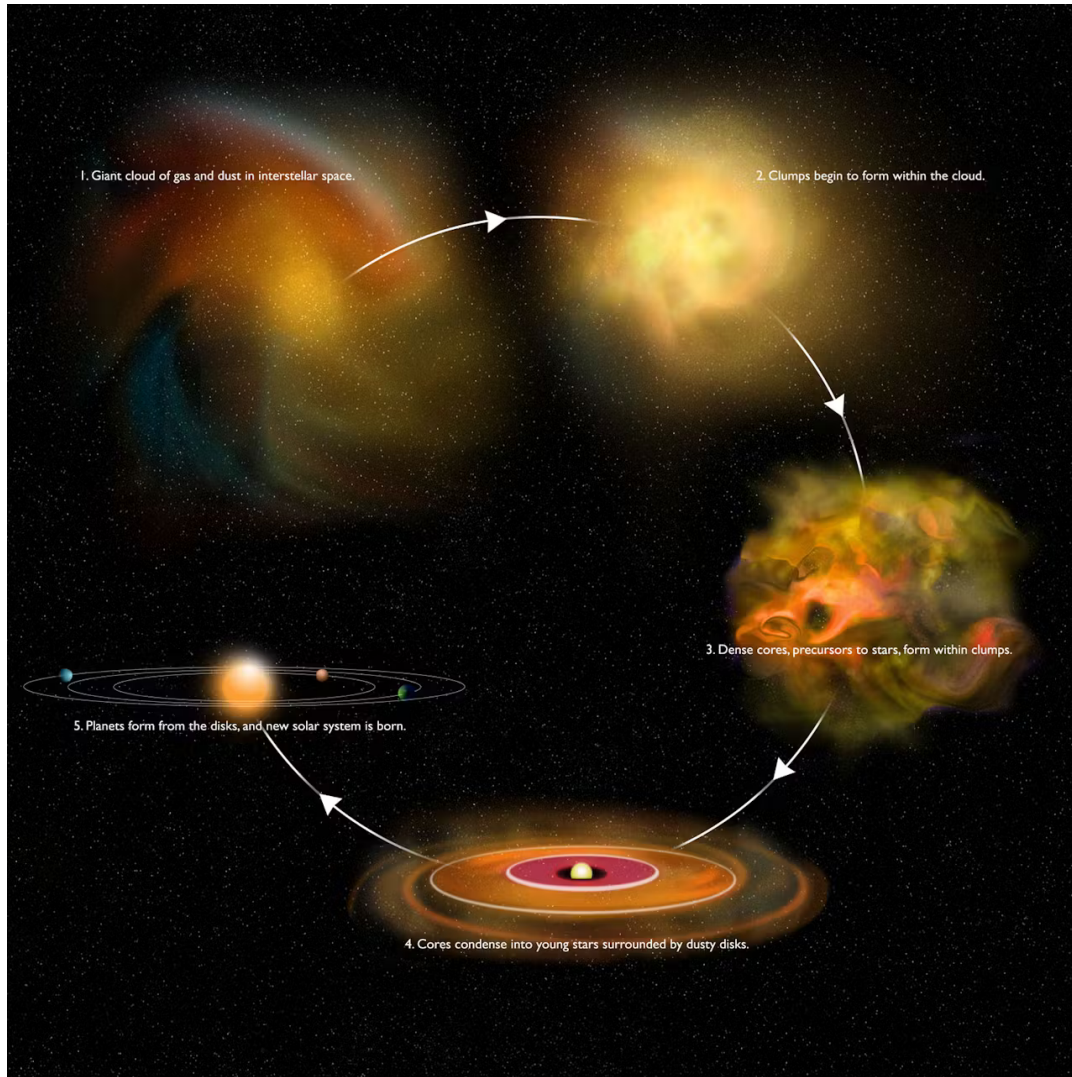
FIGURE 1.1: Scheme for multiple phases, from molecular cloud, passing by proto-star formation, finishing with evolved planetary systems. This big picture of planet formation represents, in part, the same spatial multiscale analysis in this thesis. All the evolutionary stages are briefly described, in white, in front of each artistic representation. Credit to Bill Saxton/NRAO/AUI/NSF

1.2 Star Formation

1.2.1 Low Mass Regime

The molecular clouds of star formation, or star-forming regions (SFRs), are regions of space that extend on the order of $\sim 10^3$-10^4 pc. These clouds of material with irregular morphologies originate from supernova explosions, which release all the material contained in the giant stars that produce them, filling the interstellar medium with dust and gas. Within our galaxy, the Milky Way, there are approximately 23 known and studied (Avedisova, 2002). Due to technological and observational limitations, the most studied clouds correspond to those closest to our planet, such as Lupus (at $\sim$150 pc), Chameleon (at $\sim$180 pc), Ophiuchus (at $\sim$140 pc), Orion (at $\sim$400 pc), Taurus (at $\sim$145 pc), etc (Zucker et al., 2019).

Molecular clouds, or SFRs, are also known as stellar "maternity wards," as these regions of the interstellar medium concentrate a greater quantity and/or density of material that will eventually become the raw material for forming the first stellar embryos, which in turn will evolve by accreting material to become proto-stars.

We know that stellar formation is a process that lasts on the order of 0.1-1 mega-years (Myrs), meaning the material takes that time at various points in the cloud to form objects of increasingly larger masses and sizes. These objects will begin to accrete more material at an increasingly faster rate until they reach the limit of $\sim$80 Jupiter masses (M_{Jup}), where the gravity and the weight of the upper layers of these bodies will press with sufficient force on the core for it to collapse, and atoms in its interior will begin to fuse, generating atomic reactions that heat this stellar embryo, serving as the first spark to transform into what we call a proto-star.

The interaction of forces exerted by the gravity of the proto-star and the radiative pressure generated by the atomic fusions in its core will reach a

dynamic equilibrium, where nuclear fusions will continue to occur based on the material that the star continues to accrete. This is why, broadly speaking, the mass of stars is proportionally related to their brightness and temperature when their formation is complete.
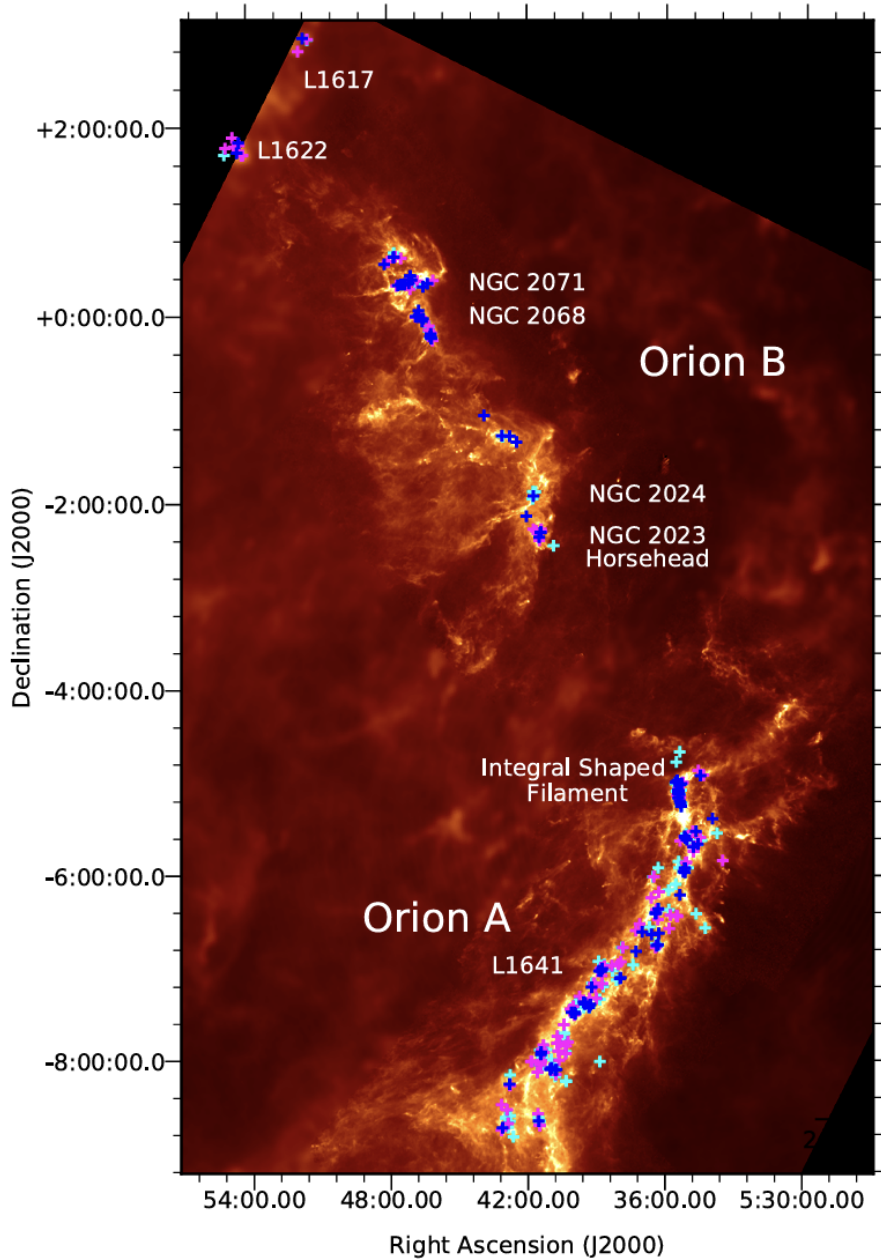
FIGURE 1.2: Census of the protostars, observed by ALMA and VLA, present in Orion SFR. The backgrou-Planck (Lombardi et al., 2014). This work is similar to this thesis, about the study of young objects, Class 0 (blue crosses), I (Magenta crosses), and FS (Cyan crosses). Figure extracted from Tobin et al. (2020).

These processes of material accumulation and proto-star formation occur

in different zones of the cloud simultaneously, producing stars of various characteristics, particularly of different masses, throughout the SFR. It is still not entirely clear how various physical mechanisms, such as the interaction of proto-stars with the cloud or the distribution of mass or position of proto-stars in the region, influence this process. One of the most accepted theories proposes a hierarchical collapse for SFRs, where those cores that form first and become more massive will attract streams of material from more distant areas in the same cloud, generating flows of gas and dust, similar to space rivers, that connect to this early generation of massive proto-stars (Vázquez-Semadeni et al., 2019). The increase in material density thanks to these streams will aid and accelerate the formation of stellar embryos and less massive proto-stars in these regions (Pineda et al., 2023).

The purpose of this thesis is not to study stellar formation in depth, but as mentioned in the title of this section, it is of interest to try to understand the formation and subsequent evolution of low-mass stars in the vicinity of the solar system. Therefore, we will continue to focus only on this type of stars (or proto-stars), without delving further into the physical phenomena related to the spatial scale of the cloud itself or massive stars ($> 8\,\mathrm{M_\odot}$) forming within it. If the reader wishes to explore these topics further, we recommend visiting the following articles on the formation of massive stars and their interactions with their respective SFRs: Tan et al. (2014), Motte, Bontemps, and Louvet (2018), and Rosen and Krumholz (2020).

1.2.2   Substellar Regime

Objects within the sub-stellar regime, particularly Brown Dwarfs (BDs), represent sources of exceedingly low mass, ranging from 13 to 80 $\mathrm{M_{Jup}}$, and hence exhibit temperatures as low as 2200 K to $\sim$ 250 K in their atmospheres

(Beamín et al., 2014). The inaugural observation of a BD, Teide 1, was documented by Rebolo, Zapatero Osorio, and Martín (1995), marking the confirmation of previously hypothesized very low mass objects elucidated by Kumar (1963), and named by Tarter (1976). These entities have garnered significant attention among astronomical circles, serving as a transitional link between giant planets and very low mass stars.

Characteristic of BDs is their spectral type (SpT), typically equal to or later than M6, rendering them exceedingly faint and posing challenges for observational studies. The mass regime of these objects precludes sustained nuclear fusion of ordinary hydrogen (^{1}H) within their cores, thus relying on deuterium (^{2}H) combustion as their primary energy source. In instances of higher mass, exceeding 65 M_{Jup}, lithium (Li) fusion may also occur.
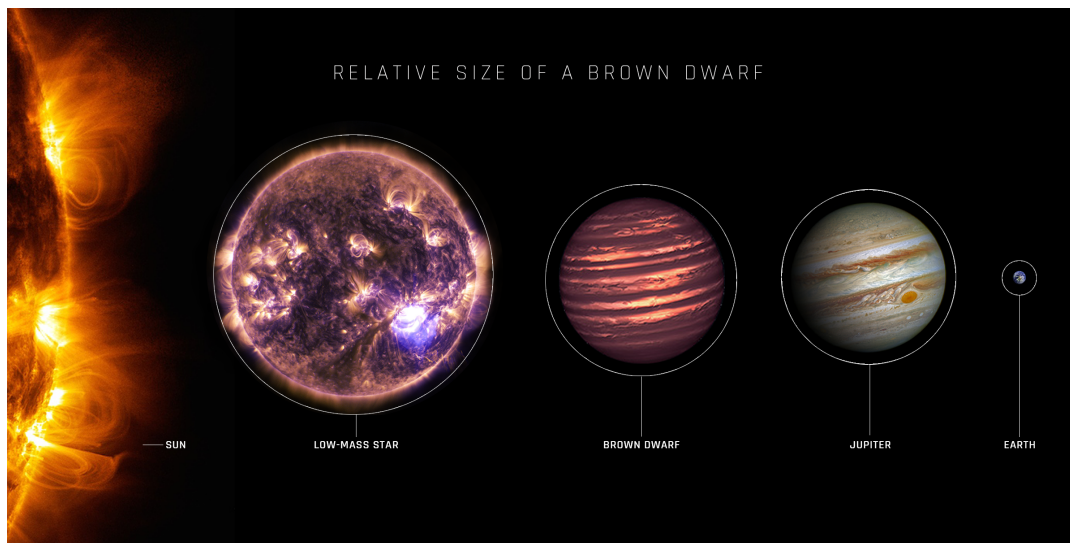
FIGURE 1.3: Artistic representation and size comparison for the Sun, a Low Mass Star, a Brown Dwarf, Jupiter, and the Earth. Credits: Jupiter: NASA, ESA, and A. Simon (NASA, GSFC). Sun and Low-Mass Star: NASA, SDO. Brown Dwarf: NASA, ESA, and JPL-Caltech. Earth: NASA. Infographic: NASA and E. Wheatley (STScI).

A significant mystery surrounding Brown Dwarfs (BDs) lies in understanding where and how they form. The most accepted hypotheses in this regard are as follows:

1) Ejection from molecular cloud filaments: In this scenario, large-scale

filamentary structures within molecular clouds fragment, leading to interactions among bodies within the region. As a result, a significant portion of lower-mass objects are ejected to regions of lower material density (Reipurth and Clarke, 2001).

2) Formation as companions within circumstellar disks: BDs may form as companions within circumstellar disks around more massive proto-stars (similar to the Sun). Gravitational fragmentation within unstable disks can lead to their separation from the central proto-star. Simulation studies suggest that approximately 70% of proto-BD companions within the disk would be ejected, while the remainder could remain gravitationally bound to the central proto-star and potentially form their own dust and gas disks (Stamatellos and Whitworth, 2009).

3) Photoevaporation due to nearby massive stars: Like other low-mass proto-stars, BDs may form initially in a similar manner. However, during their growth, much of the surrounding material could be photoevaporated due to radiation from nearby massive stars (Stamatellos and Whitworth, 2009; Whitworth and Zinnecker, 2004).

4) Decreased accretion rate due to protostellar outflows: This scenario suggests an analogous formation process between proto-BDs and proto-stars, but on a smaller scale. Presence of jets and outflows from the proto-BD would further diminish the amount of material available in the envelope, resulting in an abrupt decreasing in the accretion rate, from $\sim 10^{-6}$ M$_\odot$ yr^{-1} to 10^{-9}-10^{-12} M$_\odot$ yr^{-1}, at a critical time of $t_c \sim 10^4$ years, and ultimately leading to the formation of a sub-stellar mass object (Machida, Inutsuka, and Matsumoto, 2009).

Even the different nature of possible formation scenarios, they are not exclusive and may occur for the same sources, complimentary.

1.3 Classification of Young Stellar Objects

Given that at birth, proto-stars are highly embedded within the molecular cloud, it is virtually impossible to directly observe the light emanating from them. Photons emitted by these proto-stars are captured by the material, dust and gas, heating up to approximately 20 K for the dust, and re-emitting that light at longer wavelengths, such as infrared (IR) or sub-millimeter (sub-mm). In reality, there is a wider range of wavelengths in which circumstellar material shines, but in this case, we will refer to the observable spectral windows from the Earth's surface. This is how these bright sources began to be observed in the IR, within nebulae (or molecular clouds). These sources, which, compared to evolved stars (the stellar black body spectrum), show an excess of IR emission, are associated with the amount of surrounding dust and gas. Thus, by studying the Spectral Type Distributions (SEDs), it was confirmed that these sources were young stellar objects, prior to the main sequence. This is how they were termed Young Stellar Objects (YSOs).

After several observations of different YSOs, it was discovered that the excess IR emission varied in each case. Lada and Wilking (1984) observed sources in the molecular cloud of Ophiuchus, measuring the emission slope at wavelengths between 4 to 20 μm. The parameterization of these slopes, present in the SEDs of these objects, is given by the following equation:

$$\alpha_{IR} = \frac{d\log(\nu F_\nu)}{d\log(\nu)} = \frac{d\log(\lambda F_\lambda)}{d\log(\lambda)} \tag{1.1}$$

Where α_{IR} represents the the spectral index of IR emission in each YSO. Other studies began to observe and measure these slopes in different star-forming regions (e.g., Myers et al., 1987; Adams, Lada, and Shu, 1987; Kenyon et al., 1990, classifying the YSOs into Infrared Classes: I, II, and III (Lada, 1987). With the improvements in the instrumentation on detection of faint sub-mm emissions, Andre, Ward-Thompson, and Barsony (1993) added Class

0 to the classification of previous IR spectral index Classes, related to YSOs in high-extinction regions, and in a stage of evolution prior to Class I.

Finally, Greene et al. (1994), continuing the trend of Andre, Ward-Thompson, and Barsony (1993), with increasingly precise SED observations, defined an intermediate class between Class I and II objects. The sources of this new class exhibited a "flat" emission excess above the black body spectrum, leading to the naming of this new class as Flat Spectrum (FS).

The physical interpretations regarding the excess of infrared emission across different classes are determined by the quantity of diffuse material surrounding the YSO. In Figure 1.4, the morphology and quantity of dust and gas forming the proto-stellar system are depicted according to their respective classes.

Taking into account the scheme presented in Figure 1.4, and following the evolutionary order presented therein, the qualitative description of each IR Class would be as follows:

a) Class 0 (No emission for $\lambda < 20\mu$m): This classification is for the youngest sources among YSOs. As shown in the respective panel, there is no detectable emission in the same IR range as the rest of the Classes. Therefore, they are primarily studied in the sub-mm. Regarding the material surrounding Class 0 sources, they are surrounded by a gas and dust envelope, which interacts with jets originating from the central protostar (Kwon et al., 2009; Shirley et al., 2011). The jets start to excavate the envelope and heat the material on the interaction walls, generating mainly gas outflows. Since these outflows are young, they have opening angles $\phi_{op} < 90^o$ (e.g. van't Hoff et al., 2023). Additionally, Keplerian rotation disks have been observed in Class 0 YSOs (e.g. Tobin et al., 2012; Maret et al., 2020), indicating early disk formation, probably simultaneous with the protostar. Dust disks in Class 0 lack prominent substructure, exhibiting a smooth radial decay of the flux (Ohashi et al., 2022).
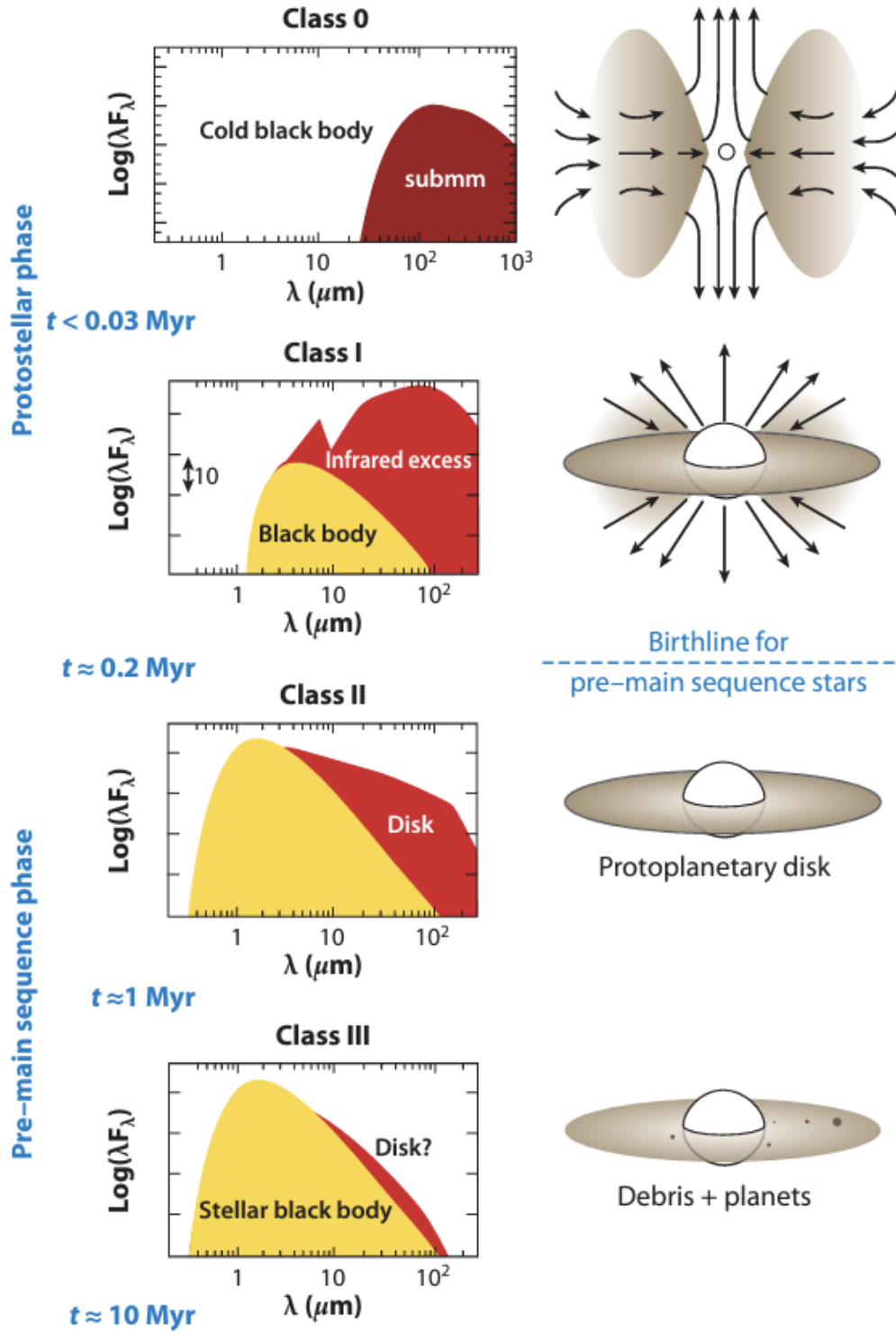
FIGURE 1.4: Schematic panels of different Classes (0, I, II and III), with the SED representation of each Class and their respective model of black body emission (Left column). In addition there are visual representations of the material interacting with the circumstellar disk and protostar, corresponding to the respective Class (Right column). This figure is adapted from Zhang (2015).

b) Class I (α_{IR} > 0.3): For these sources, the envelope remains present around the YSO, but much of the material has either fallen onto the circumstellar disk or been expelled from the system by outflows. There is a greater variety in the morphology of outflows observed in the sub-mm for this class (e.g. Hsieh et al., 2023), and examples of these different large-scale spatial structures will be shown and discussed in Chapter 2. Circumstellar disks are also observed for these objects, where they begin to be more observationally clear in lines with optically thin behavior due to the decrease of material in the envelope (e.g. Harsono et al., 2014). In the continuum, disks of these YSOs begin to show substructures such as rings and gaps (e.g. Segura-Cox et al., 2020).

c) Class FS (-0.3 < α_{IR} < 0.3): Being an intermediate class between Class I and II, they exhibit extended gas structures similar to those observed in Class I, such as outflows, but with smaller angular scales (discussed in 2). Generally, Class FS YSOs present a continuum flow closer to Class I than to Class II (e.g. Williams et al., 2019).

d) Class II (-1.6 < α_{IR} < -0.3): These objects are the most abundant in nearby SFRs (Evans et al., 2009) and have been studied extensively to date (e.g. Ansdell et al., 2016; Cieza et al., 2019; Barenfeld et al., 2016; Barenfeld et al., 2017). For these objects, the envelope has finished dissipating, leaving all material accreted by the disk and the protostar. Observations of these disks reveal a wide variety of substructures, such as spiral arms (e.g. Huang et al., 2018b), axial asymmetries (e.g. Casassus et al., 2015), and multiple rings and gaps (e.g. Andrews et al., 2018; Cieza et al., 2021). The observed gas is found in the disk, with Keplerian rotations (e.g. Pinte et al., 2020), with the gaseous disk being spatially equal to or larger than the dust disk (e.g. Antilen et al., 2023).

e) Class III (α_{IR} < -1.6): These are the most evolved YSOs of all, also known as Debris Disks. They are also considered main sequence sources

surrounded by dusty rings, equivalent to the kuiper belt. In this class of objects, gas has almost completely dissipated in the disk, being accreted by planets and the central star. Despite this theoretical paradigm, observations with high sensitivity show the presence of gas around these objects (Moór et al., 2017). These sources present at least one dust ring in the disk (Hughes, Duchêne, and Matthews, 2018), but the origin of these dusty structures is not entirely clear. Most works regarding dust in Debris Disks propose continuous emission of second generation, that is, material produced by collisions of exocomets (Wyatt et al., 2015).

Between Class II and III YSOs, there exists a transitional classification known as transition disks (Strom et al., 1989). Moreover, in recent years, the first detections of protoplanets in formation within the cavity of a transition disk have been observed (Figure **??**).
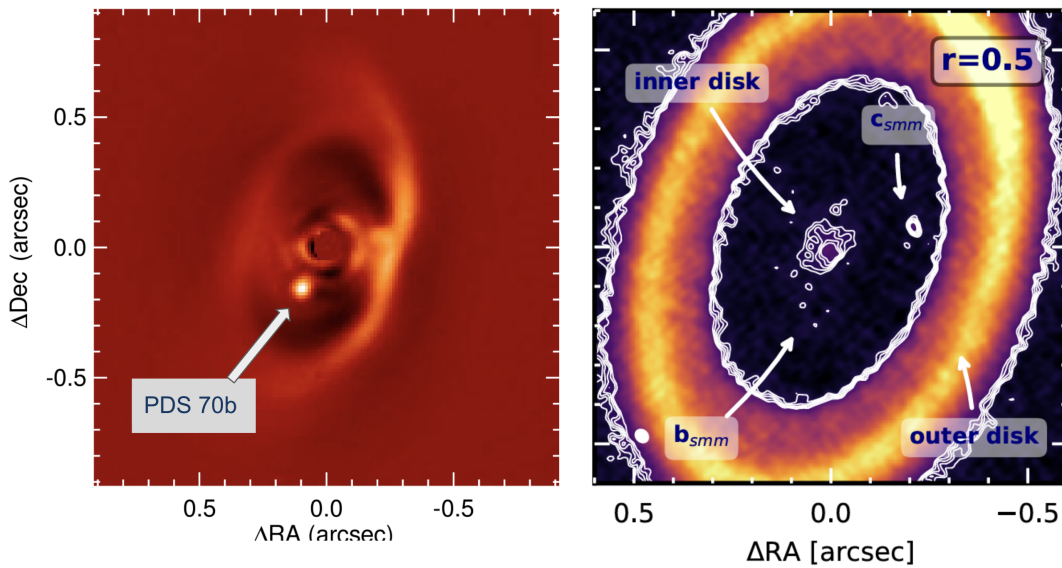
FIGURE 1.5: Left: First dettection of protoplanet PDS 70 b, using the SPHERE/IRDIS instrument at VLT, at NIR wavelenghts. Plot from Müller et al. (2018). Right: First detection of a circumplanetary disk inside the cavity of a transition disk. In this case, the protoplanet corresponds to PDS 70 c, and the observation were made by ALMA observatory at 0.8 mm wavelenght. Plot from Benisty et al. (2021).

These disks, studied based on their SEDs, do not exhibit excess infrared emission for the near and mid-IR ($< 20 \ \mu$m), but there is an excess for longer wavelengths in the far-IR ($> 20 \ \mu$m). Given this, a depletion of material from

the disk was postulated, where the material closer to the star, and therefore at higher temperatures, diminishes over time (Calvet et al., 2005; D'Alessio et al., 2006).

Spatially resolved images from VLT and ALMA show the initial morphologies of transition disks, with large cavities and compact inner disks of a few au in radius, confirming what was previously observed in the SEDs, with little hot material in the inner part of the disk, but material prevailing in external zones of the disks (Casassus, 2016).

Using the VLT telescope, the protoplanet PDS 70b was observed in the PDS 70 source (Keppler et al., 2018; Müller et al., 2018). Subsequently, using ALMA, the circumplanetary disk surrounding the protoplanet PDS 70c was observed (Benisty et al., 2021). While detecting protoplanets within the cavities of transition disks is not trivial, it is expected that in the coming years, observations with high sensitivity will provide us with more detections and properties of these protoplanets. An example of such disks, which could potentially harbor protoplanets, is ISO-Oph 2, discussed and analyzed in Chapter 3 of this thesis.

1.4   Jets and Outflows

As outlined in Section 1.2, the gravitational collapse within the clumps of the cloud gives rise to a complex system comprising a nascent proto-star, enveloped by a circumstellar disk, and surrounded by a shell of gas and dust (e.g., Shu, Adams, and Lizano, 1987; Allen et al., 2007; Dunham et al., 2014a). During their early developmental phase, proto-stars remain deeply embedded within their envelopes, which, in turn, are embedded within the molecular cloud.

Once the protostar initiates its nuclear reactions, along with the interaction of the circumstellar disk, magnetohydrodynamic (MHD) activity is generated in the protostar. Similar to other astronomical phenomena on larger scales, this MHD reaction produces the emission of jets of ionized material at high velocities, reaching distances of several hundred km s^{-1}. The first observation of the interaction of these jets with the hosting molecular clouds was given by compact clumps of bright emission in nearby star-forming regions (Herbig, 1951; Haro, 1952). These objects exhibited collinear emissions extending over thousands of au close to de NGC 1999 molecular region. This is how they were termed Herbig-Haro objects (HH), encompassing all observations of similar phenomena in molecular clouds. It was only decades later that this phenomenon was discovered to be associated with YSOs in their respective clouds (Schwartz, 1977). With the development of new instruments and observations across various wavelengths, the nature of such emissions was ultimately confirmed. Figure 1.6 displays a sample of observations for jets around YSOs, showcasing extensive spatial lengths and bright hot material from the cloud interacting with the jets. It is possible to note that there is no visible central protostar, but the presence of diffuse bipolar outflows close to the central positions of the jets.

The morphologies, sizes, and velocities of outflows are contingent upon various factors, including the specific tracer employed, as well as the luminosity, mass, evolutionary stage, and age of the young stellar object (YSO). Additionally, they depend on the durations of active accretion and outflow-driving phases, and the properties of the environment through which the flow traverses. Among the available tracers, the low-J rotational transitions of CO have been extensively utilized for molecular outflow studies. CO is abundant (with N(CO) $\sim 10^{-4}$ N(H$_2$)), and its lowest energy levels are readily populated by collisions with H$_2$, aligning with the typical densities
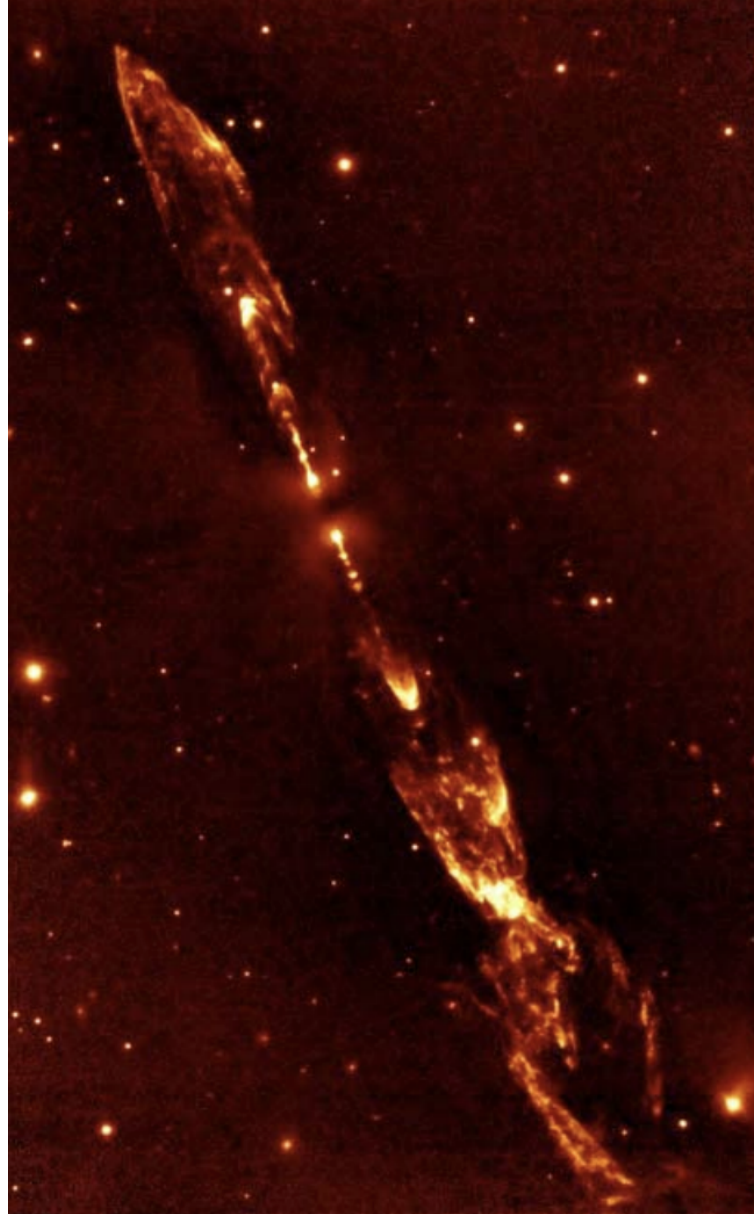
FIGURE 1.6: Spectacular colored image of the jet HH 212 in the L1617 region. This observation was taken by VLT telescope, at the wavelenght $\lambda = 2.1$ μm, corresponding to the emission of H_2 molecular line. This structure extend by $> 4 \times 10^4$ au from each extreme of the jets. This Figure is presented in Bally, Reipurth, and Davis (2007), but originally in black and white in Zinnecker, McCaughrean, and Rayner (1998).

and temperatures of molecular clouds. These CO emission lines are detectable from ground-based observatories in the 3, 1.3, and 0.85-mm atmospheric windows. However, higher-J transitions of CO, as well as species like SiO and H2O, whose abundances may increase in shock environments, and shock-excited H_2, are more indicative of the accelerated warm and hot gas present in molecular outflows.

Outflows are pivotal in dispersing protostellar cores, terminating the infall phase, and facilitating the removal of disk angular momentum crucial for accretion (Machida and Hosokawa, 2013; Frank et al., 2014; Offner and Arce, 2014; Bally, 2016). They significantly impact the mass assembly process, final star masses, and the initial mass function (IMF; Alves, Lombardi, and Lada, 2007; Arce et al., 2007; Pascucci et al., 2023). Comparative studies between the core mass function (CMF) and the IMF suggest a strong correlation, with a core-to-star efficiency of approximately 30% (e.g., Alves, Lombardi, and Lada, 2007; André et al., 2010; Motte et al., 2022). Observations indicate that outflows possess sufficient energy and momentum to disperse the material in surrounding parent cores within 1 Myr (Dunham et al., 2014b; Zhang et al., 2016). While some studies suggest that outflow opening angles widen over time, facilitating gas clearing in the surrounding envelope (Arce and Sargent, 2006; Velusamy, Langer, and Thompson, 2014; Hsieh, Lai, and Belloche, 2017), others argue that outflow mass-loss rates are insufficient to be the primary agent of core dispersal (Curtis et al., 2010). Recent observations using Hubble Space Telescope (HST) near-infrared (NIR) images found no evidence for the widening of outflow cavities as protostars evolve (Habel et al., 2021), challenging the notion that outflows are the main driver of the low star formation efficiency of 30%.

As previously mentioned, the presence of outflows depends on the evolutionary state of YSOs, primarily being found in sources of Classes 0, I, and FS. Figure 1.7 showcases an image of the exciting future for studying outflows around young sources. This image was recently obtained with the JWST and displays outflows of large spatial scale around a very YSO, with an age of just 0.1 Myr, located in the Taurus star-forming region. The significance of such structures in the evolution of protostars and protoplanetary disks will be discussed in Chapter 2, along with future observations related to this thesis presented in Appendix A.

FIGURE 1.7: Observation from the JWST using the NIRCam instrument, and the filters F200W, F335M, F444W, and F470N. The target corresponds to IRAS 04368+2557 in the Taurus constellation. This image shows the presence of very extended bipolar outflows around a YSO. Credits to: Joseph DePasquale (STScI), Alyssa Pagan (STScI), Anton M. Koekemoer (STScI)

1.5   Planet Formation

Over recent decades, advancements in telescope technology have revolutionized our understanding of planetary formation processes within protoplanetary disks encircling proto-stars. However, the roots of conceptualizing planetary formation from small solid materials trace back nearly three centuries.

In 1734, Emanuel Swedenborg proposed that planets in our solar system formed from a surrounding structure fragmenting around the Sun, an idea

inspired by Newton's work on gravity. Immanuel Kant expanded on this concept in 1755, suggesting that stars and their planets formed from slow-rotating nebulae under gravitational forces.

Similarly, in 1796, Pierre-Simon Laplace proposed a model involving a vast solar pseudo-atmosphere, cooling and shedding material that coalesced into planets. Despite initial acceptance, Laplace's model faced challenges, particularly regarding angular momentum distribution within the solar system, leading to its eventual abandonment.

In the early 20th century, alternative theories emerged but failed to gain traction. Andrew Prentice revisited Laplace and Kant's ideas in 1978, formulating the "modern Laplace theory," which faced challenges from subsequent simulations revealing turbulence's dissipative nature.

In 1972, Safronov formulated a seminal theory positing that planets formed from collisions and accretion of asteroid-like bodies in a disk-shaped system around the Sun. His work emphasized collision dynamics and gravitational forces' role in particle aggregation, leading to the formation of planetary bodies over millions of years.

Safronov's theory provided insights into planetary rotation rates and axial tilts, highlighting collision dynamics' fundamental importance in shaping planetary systems.

Given the lack of a comprehensive explanation for the regulation of angular momentum and the kinetic and dynamic barriers in the interaction between gas, dust, and larger bodies within the protoplanetary disk, two theories emerge to address these theoretical limitations. These theories, known as Core Accretion (Reviewed by Lissauer (1993)) and Gravitational Instabilities (Boss, 1997), remain the primary models in the study of planetary formation.

1.5.1   Core Accretion

Essentially stemming from the aforementioned accretion models, this idea entails the accumulation of refractory solid material, where micron-sized dust grains coexist within the same regions of the disk, clumping and sticking together to form increasingly larger and more massive bodies. Within the disk, not only is there hot dust of dense elements, but also, beyond the snowlines, these granules of material include ice-water solidifications. Over periods of thousands of years, these material grains interact by colliding at low velocities, merging, and gaining increasingly more mass, reaching sizes on the millimeter/centimeter scale, and decoupling from the gas also rotating in the disk, ultimately accreting towards the proto-star. As the mass of these grains begins to increase (to meter and/or kilometer diameters), gravity becomes an important factor in driving collisions, initiating a "run-away" process for the mass growth of the grains, which begin to collide and merge ever more rapidly. As gravity becomes the driving mechanism for the growth of these bodies, an oligarchic growth process begins, where protoplanets begin to accrete smaller-sized material, leaving almost exclusively the objects of greater mass, culminating in the formation of rocky planets (Earth-like), and the cores of ice giants (Neptune-like) and gas giants (Jupiter-like). In the event that rocky or icy cores continue to accrete material and reach a mass between 5-10 M$earth$, while the disk remains gas-rich, then these cores will accrete the available gas around their orbits, obtaining increasingly massive and dense atmospheres. Finally, if these protoplanets surpass the threshold of ~ 30 M$_\oplus$, then a "run-away" process will begin in the gas accretion from the disk, culminating in the formation of gas giant planets within the planetary system. The theoretical timescales for these processes are as follows: (1) 10^4 years for the dust sticking of micrometer-sized dust. (2) 10^5 years for the "run-away" growth of planetary embryos. (3) 10^6-10^7 years for the oligarchic

growth of protoplanets. (4) 10^7-10^8 years for the final formation of rocky planets, where they undergo the last collisions of great impact prior to system stability. In the case of the cores of giant planets (of ice and/or gas), when they reach the "run-away" stage in gas accretion, they accelerate their formation and growth process, ultimately reaching their final mass between 10^5-10^7 years. Figure 1.8 shows an scheme for the theoretical timescales with previously mentioned formation stages, and the timeline for the different planet types.

This model exhibits some limitations or barriers in certain aspects of its processes, particularly where the mechanisms or estimations for gas and dust values are inaccurately estimated or significantly deviate from recent observational data. Subsequently, we will provide a brief overview of the most prominent barriers within this planetary formation model.
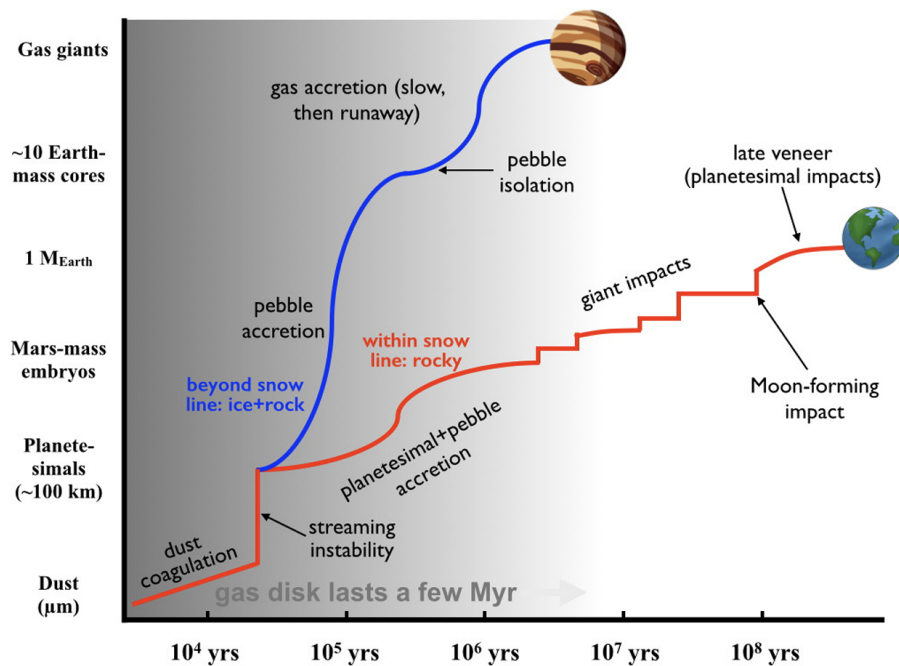
FIGURE 1.8: In blue line the Giant Gas Planet timeline representation, for all the evolutionary stages. Same for the rocky planets in red line. X axis represents the time range estimations for the different processes, and Y axis corresponds to a representative size scale for the material that participates in every physical evolutionary track. Figure from Raymond and Morbidelli (2022).

1.5.2 Gravitational Inestabilities

Within the physical phenomena affecting objects in space, the most significant is gravity. Generally, we associate gravity among different bodies, which interact with each other through it, depending on the masses and distances of the objects forming part of the system. An interesting behavior to study is when objects become massive enough to not only interact with other distant objects but also gravitationally interact with themselves. This phenomenon is called self-gravity.

Suppose a thin and axisymmetric gaseous disk; it can be subject to gravitational instabilities due to its interaction with the central proto-star, leading to the fragmentation of the disk into dense gas clumps distributed radially, mainly in the form of spiral arms (Rice et al., 2003; Zhu et al., 2012). These clumps are subject to self-gravity, collapsing in on themselves and producing the first planetary embryos (Boss, 1997).

For disk fragmentation to occur, there is a criterion formulated by Toomre (1964), where by studying the stability of axisymmetric and infinitesimally thin disks, he arrives at the following equation:

$$Q = \frac{c_s \Omega}{\pi G \Sigma_{\text{gas}}} \tag{1.2}$$

Where c_s corresponds to the gas sound speed, Ω is the orbital frequency, Σ_{gas} is the surface density distribution along the disk, and G is the universal gravitational constant. So, for the disk to become unstable, a critical value of the Toomre parameter is needed, given by $Q_{\text{critical}} = 1$. That is, as long as the disk has a parameter $Q > Q_{\text{critical}}$, it will be gravitationally stable. Despite this theoretical critical value, numerical simulations for gaseous disks have shown that for values $Q \leq 1.7$, spiral arms with gas overdensities clumps begin to form (e.g., Durisen et al., 2007). Although we mentioned that reaching the $Q \leq Q_{\text{critical}}$ is necessary for Gravitational Instabilities (GIs) to occur, this

is not a sufficient requirement to generate core fragmentation.

Figure 1.9 shows a capture, from a whole simulation, modeling the fragmentation of the PPD due Gravitational Inestabilities. In difference with sub-mm observations, models present several spiral arms, at least at the first stages of the fragmentation. Also dense cores are forming at large distances from the protostar, > 10 au in this case. This contrasts with the existence of massive exo-planets detected at short distances from their host stars (few au), like Hot Jupiters.
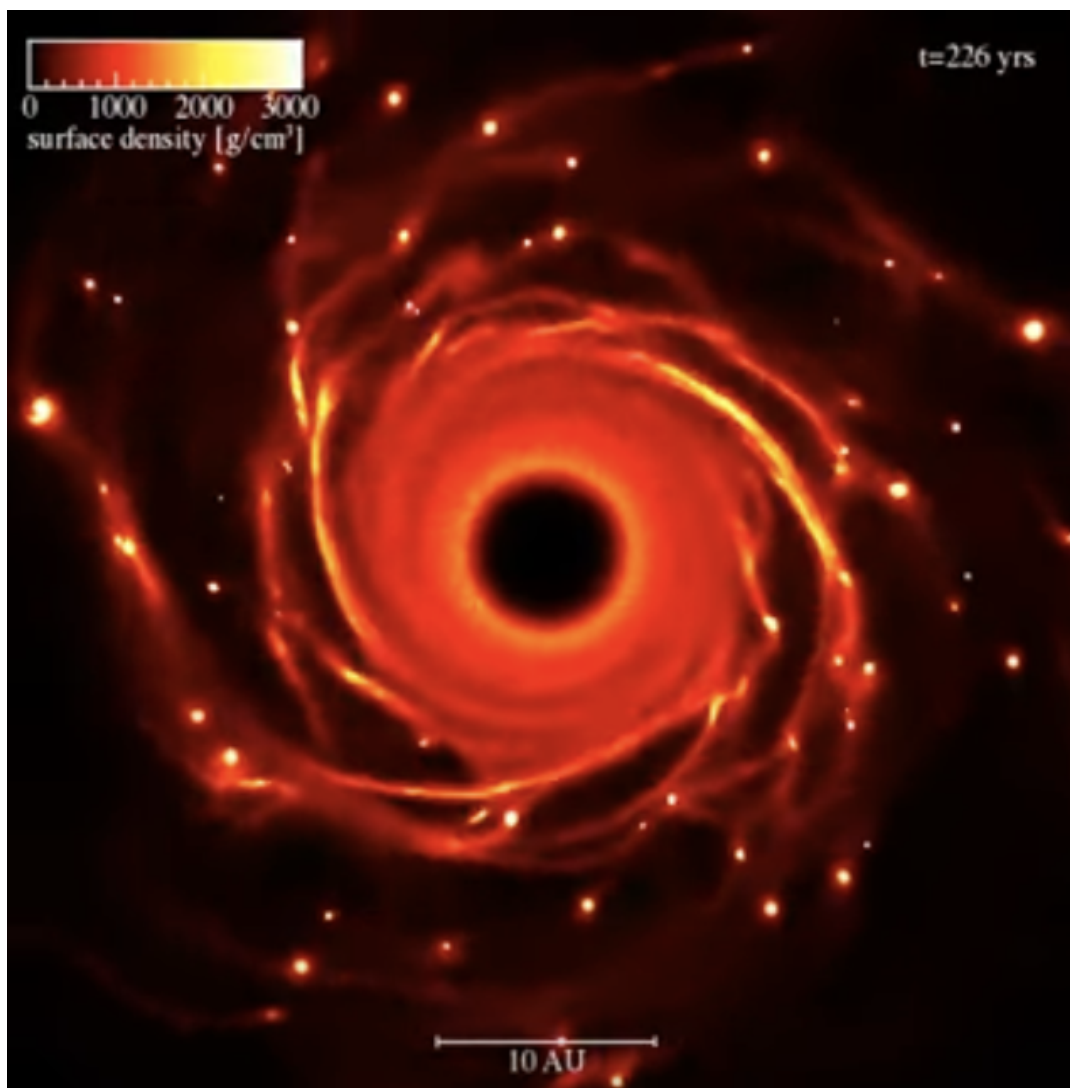
FIGURE 1.9: Simulations of spirals patterns produced by Gravitational Inestabilities in a circumstellar disk, around a YSO. Dense cores of material form at different distances from the protostar, driven by the spiral arm structures accumulating the material, and changing the dust and gas density distribution within the disk. Credits to Daniel J. Price (video).

1.5.3   Barriers in Planet Formation Theories

Radial Drift

In the early stages of planetary formation, micrometer-sized dust particles (μm) embedded within the protoplanetary disk are coupled to the motion and pressure of gas molecules, thus unable to move or float freely. The forces acting on the dust particles depend not only on the relative motion between the dust and gas but also on the size of the particles. When the dust particles are sufficiently small, $a \ll \lambda$, with a being the radius of the particles and λ the mean free path of gas molecules, then the system can be assumed to be in the "Epstein drag regime". In this case, the drag force ($\mathbf{F}_{\text{drag}}$) is given by the following equations:

$$\mathbf{F}_{\text{drag}} = -\frac{3\pi}{4}\rho_g a^2 v_{\text{th}} \mathbf{v} \quad ; \quad v_{\text{th}}^2 = \frac{8kT}{\pi\mu m_{\text{H}}} \tag{1.3}$$

where ρ_g is the gas density, v_{th} is the thermal velocity, $\mathbf{v}$ is the velocity of the particle relative to the bulk motion of the gas, k is the boltzmann constant, T the temperature of the system, μ is the mean molecular weight, and m_{H} is the mass of the hydrogen atom.

When dust particles begin to agglomerate and increase in size such that they reach a size similar to the mean free path of gas molecules, $a \gtrsim \lambda$, a flow pattern emerges around the dust particle, and the drag force ($\mathbf{F}_{\text{drag}}$) is characterized as being in the "Stokes drag regime". In this case, the drag force included now a friction time parameter (τ_f), due the interaction with the particles and gas. The Stokes drag force is given by the following equation:

$$\mathbf{F}_{\text{drag}} = \frac{m\mathbf{v}}{\tau_f} \quad ; \quad \tau_f = \frac{4}{9}\frac{a^2\rho_d}{c_s\rho_g\lambda} \tag{1.4}$$

In these equations m and v represent the mass and velocity of the particles, ρ_d is the density of the particles, and c_s the speed of sound in the system.

In the Stokes regime, a useful parameter emerges to simplify the behavior of floating particles interacting in gaseous mediums. The Stokes number is a dimensionless value representing the aerodynamic efficiency of different materials in various mediums. In this particular case, it denotes the friction time (τ_f) relative to the orbital period (Ω_K) of particles in the disk. The Stokes parameter is given by the following formula:

$$St = \tau_f \, \Omega_K \tag{1.5}$$

This dimensionless value proves highly beneficial for such problems as it standardizes the aerodynamic capabilities of diverse bodies in different materials. Hence, regardless of the medium or particle properties, if two objects share the same St number, they will exhibit equivalent aerodynamic efficiency in their respective mediums.

The existence of these drag forces gives rise to the phenomenon of radial drift by dust particles, which, depending on their Stokes numbers, and consequently their sizes and masses, could lead them to fall towards the proto-star at a speed greater than necessary to form planetary embryos or proto-planets. To clearly understand how radial drift affects dust particles, one must first comprehend the force balances within the gaseous disk, considering gravitational, centrifugal, and pressure forces. Gravity, exerted by the central proto-star, points towards the interior of the disk, whereas centrifugal force naturally pushes the gas towards the outer region of the disk. The pressure experienced by the gas also points towards the outer part of the disk. This is because the higher gas density at higher temperatures is found in the inner disk, near the proto-star, resulting in sub-Keplerian velocities in the gas motion, as explained by the following equation:

$$\mathbf{v}_{\text{gas}} = \mathbf{v}_{\text{K}} - \Delta\mathbf{v} \quad ; \quad \Delta\mathbf{v} = \frac{1}{2}\left(\frac{H}{r}\right)^2 \frac{\partial\ln P}{\partial\ln r}\mathbf{v}_{\text{K}} \tag{1.6}$$

Where v_K is the keplerian velocity and Δv is the sub-Keplerian velocity difference. For the logarithmic pressure radial gradient, usually is considered $\partial \ln P/\partial \ln r$ = -3.5 in the mid-plane of the disk. Also in the minimum mass solar nebula (MMSN), the aspect ratio H/r is proportional to $1/r^4$, estimating a sub-Keplerian velocity difference of $\Delta v \sim 50$ m s^{-1}.

Finally, combining the last two equations, we obtain the following expression for the radial velocity v_r of dust particles:

$$\mathbf{v}_r = -\frac{2\Delta\mathbf{v}}{\mathrm{St} + \mathrm{St}^{-1}} \tag{1.7}$$

With this, we can study different scenarios for the Stokes number (*St*) for various types of dust particles. For smaller particles, which are fully coupled to the gas, $St \ll 1$, and thus $v_r \ll 1$. For larger particles, the same phenomenon occurs as they are completely decoupled from the gas motion, so if $St \gg 1$, it also implies that $v_r \ll 1$. The most complex case arises for particles with $St \approx 1$, where the radial velocity takes values $v_r \approx -\Delta v$, causing this material to rapidly fall towards the center of the disk, and consequently towards the proto-star.

Although the radial drift for the dust, there are porposed mechanisms to retain the dust orbiting the proto-star, and stopping the radial drift. We will discuss those mechanisms in next sections.

Fragmentation

When dust particles accumulate and form pebbles of sizes greater than XX, their interaction with gas turbulence ceases to be significant, and the growth of dust will depend solely on the interaction between these pebbles. In this size regime, two additional barriers to pebble growth through accretion appear due to collisions between them, namely bouncing or fragmentation of

these bodies upon mutual collision (Blum and Wurm, 2000; Birnstiel et al., 2010; Krijt et al., 2015).

Fragmentation, as its name clearly illustrates, occurs when two solid material granules collide, but instead of undergoing a plastic collision resulting in a pebble larger than the two prior ones, they fragment into smaller granules, thus preventing the formation of increasingly larger bodies.

The outcome of collisions between dust granules depends on the size, velocity, and mass of the participating bodies in the collision (e.g. Wada et al., 2007; Wada et al., 2008). Therefore, studies on grain growth based on accretion propose a velocity range of $\sim$0.1-50 m s^{-1}, given the turbulence of the grain medium, suggesting a grain growth over millimeter sizes just considering a threshold velocity of $v > 30$ m s^{-1} (Brauer, Dullemond, and Henning, 2008). Laboratory experiments have shown that fragmentation velocity is much lower than that proposed by aggregation growth models, concluding that only collisions at velocities $v_c < 1$ m s^{-1} could prevent the fragmentation of initial micron-sized silicate monomers (Güttler et al., 2010). This pertains to solid and dry dust granules (mainly silicates), but there are also studies proposing more promising conditions for icy grains. In these types of granules, due to the physical properties of ice, they could couple together in collisions with higher velocity ranges, $v_c < 9.6$ m s^{-1}, allowing for a greater chance of success in icy grains (Gundlach and Blum, 2015).

The other barrier, also related to collisions between granules, is bouncing. For velocities smaller than those causing fragmentation, it happens that dust granules withstand collisions without fragmenting but do not have the ideal structure to generate plastic collisions, bouncing off each other, resulting in nearly elastic collisions.

1.5.4   Solving the barriers

To address the barriers of grain growth, it is necessary to prevent grains from having a high radial velocity, thus allowing them enough time to couple and adhere to each other before being accreted by the star. In addition to reducing the turbulence of the disk, avoiding grains from colliding at high speeds and ending up fragmented or bounced.

One of the most successful solutions among the community, for maintaining regions of high dust density while avoiding radial drift, are pressure bumps. These regions of the disk have a positive pressure gradient, causing dust grains to feel a push towards the outer part of the disk, counteracting radial drift. The ways to generate these gas and dust overdensities (dust trapping) in the disk are mainly as follows:

Dead Zones: These regions of the disk are associated with the outer part of the mid-plane, presenting low levels of ionization, and therefore, low turbulence. Given the low ionization of the medium, there is no action from magnetorotational ionization (MRI), being one of the first explanations and candidates for zones of dust trapping. Additionally, in these external regions of the disk, up to 20 au, there are variations in the viscosity of the medium, allowing grains to grow and greatly reducing radial drift. Hydrodynamic simulations have shown that Dead Zones are capable, by themselves, of producing gaps and structures present in transition disks (Pinilla et al., 2016; Delage et al., 2023).

Snow Lines: These regions correspond to radial limits, where the temperature allows the condensation of volatiles, thus obtaining a region where both volatiles in solid and gaseous states coexist. In general, the majority of volatiles present in the protoplanetary disk correspond to H_2O, CO, and CO_2. By coexisting in different states, the addition of these volatiles to dust grains

becomes fundamental in altering the physical properties of the grains, allowing for better coupling between them. Additionally, the multiple changes of physical states that occur in the Snow Lines increase the surface density of these regions, increasing the viscosity of the medium, decreasing the radial drift of the material, and consequently, producing zones of dust trapping (Pinilla et al., 2017). These material accumulation zones have been observed in accordance with CO (Guidi et al., 2016) and H_2O (Cieza et al., 2016) Snow Lines.

Photoevaporation: Given the interaction between the disk and the central proto-star, solid particles falling radially towards the central source increase in temperature; depending on the star's luminosity, they would evaporate, generating viscosity gradients in the disk, with the same material coexisting, similar to what occurs in the Snow Lines, in liquid and gaseous states. Thus, negative pressure changes would be produced, generating dust trapping. This Photoevaporation of the inner disk would move radially, as the disk front, exposed to the highest amount of radiation from the proto-star, would evaporate radially, opening an increasingly larger cavity, until reaching the thermal limit given by the brightness of the proto-star, and eventually forming bright rings of accumulated material (Pascucci et al., 2023, in a review).

Presence of a Giant Planet: Here lies the dilemma of the chicken and the egg since various studies have shown that the presence of Neptune-type planets can generate pressure bumps in the disk (e.g., Rice et al., 2006; Pinilla et al., 2012). Depending on the scale-height, density distribution, and viscosity of the disk, the mass necessary for a protoplanet to open a gap wide and/or deep enough to be visible in current observations is determined. Additionally, the presence of a sufficiently massive, Saturn-type planet can even generate more than one pressure bump in the disk (Bae, Zhu, and Hartmann, 2017), thus allowing the accumulation of material and reduction of radial

drift in multiple locations of the disk. Not only have models been shown to allow dust trapping in disks interacting with massive planets, but it is also possible to find an increase in grain growth for millimeter-sized particles, depending on the disk conditions, coalescing into larger particles (Bi, Lin, and Dong, 2021).

An schematic representation of some of mentioned dust trapping mechanisms, it is presented in Figure 1.10. In this particular case, each diagram represent a possible mechanism to form transition disks, with bright rings in the external region of the PPDs, and a cavity of sub-mm emmiting material around the protostar.
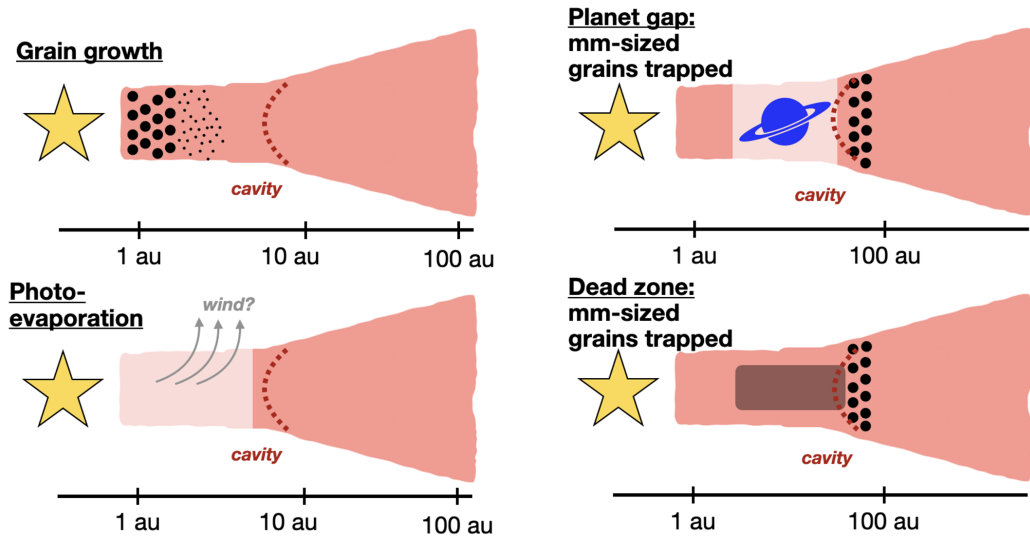
FIGURE 1.10: Some of possible mechanisms forming transition disks, and dust trapping. Each panel labeled the respective mechanism. Figure from van der Marel (2023)

1.5.5 Pebble Accretion

In the preceding sections, we have listed and described various arguments and models that would address the barriers to the growth of solid bodies or planetary embryos, overcoming both radial drift and fragmentation in collisions. However, it remains unclear how planetesimals begin to grow into cores of giant planets. In this context, the theory of pebble accretion emerges,

where planetary embryos start to accrete pebbles in gaseous environments violently and rapidly to quickly reach a critical size and mass to begin accreting gaseous material in the disk.

Ormel and Klahr (2010) propose 2D models for the interaction of dust of different sizes and St with protoplanets radius $R_p \gtrsim 100$ km. Using the Hill Radius (R_{Hill}), presented in equation 1.8, where a_0 is the semi-major axis of the orbit, and M_p the mass of the protoplanet, they analyze the behavior of the dust in different gas interaction regimes, interacting with the protoplanet and its vicinity.

$$R_{Hill} = a_0 \left(\frac{M_p}{3M_*} \right)^{1/3} \tag{1.8}$$

Thus, they analytically study three possible scenarios for the trajectories of pebbles due to the influence of giant planet cores:

Settling Encounters: In this case, particles have direct falling trajectories towards the protoplanet, where pebble accretion is independent of the protoplanet's R_{Hill}.

Hyperbolic Encounters: Here, particles fall tangentially to the gravitational influence of the protoplanet, similar to what would be an unstable orbit, ultimately accreting onto the larger body. In this case, the velocity of descent towards the protoplanet is mainly influenced by gas drag.

Three-body Encounters: The gravitational attraction given by the R_{Hill} attracts pebbles around the protoplanet's orbit, which, together with gas drag, allows some of the pebbles within R_{Hill} to accrete onto the protoplanet. The main conclusion of these models shows that when protoplanets reach a size $R_p \sim 10^3$ km, they can rapidly and effectively accrete pebbles with a St ~ 1, being a simple and efficient way for hurried protoplanet growth.

Despite efforts to explain the existence of giant planets in short timeframes within the protoplanetary disk, it still takes too long for protoplanets

that are dozens of AU away from the star, contradicting current observations. This is why new pebble accretion models showed that giant planets could indeed form rapidly, both at ~ 5 AU and at ~ 50 AU from the proto-star, providing support for the core accretion theory, as the cores of gaseous giant planets could now reach the critical mass of $m_{crit} \sim 10$ $M_{\oplus}$, necessary to begin the rapid gas accretion phase. This m_{crit} would form in timeframes of $\lesssim 1$ Myr, a time shorter than estimated observationally for gas dissipation within protoplanetary disks. For these models to work, a large quantity of pebbles in the midplane of the disk is needed, ideally with $\tau_f \sim 0.1$ (Lambrechts and Johansen, 2012).

1.5.6   Runaway Accretion

Once the pebble accretion stage is surpassed, and the heavy cores of giant planets reach their m_{crit}, then the next evolutionary stage begins, the runaway gas accretion. This process, where protoplanets begin to primarily enrich themselves with Hydrogen and Helium, was proposed by Pollack et al. (1996). However, the core accretion mechanisms known up to that point required much longer time ranges than those observed subsequently (Alibert et al., 2005). This barrier is overcome by pebble accretion models, providing much more realistic ranges, compared to observations, for the formation of gas giants.

This gas accretion period is divided into different stages. Firstly, the core of the future gas planet forms an envelope of material around it, all driven by the influence of gravity through the Hill sphere, or the possible type I migration of the protoplanet within the disk (Crida and Bitsch, 2017). The growth of this envelope of material surrounding the protoplanet is generally assumed to be within a hydrostatic regime in the vicinity of the protoplanet. Additionally, the continuous accretion of planetesimals and pebbles towards

the protoplanet generates a high-temperature system and greater luminosity on the surface of the protoplanet. Once a mass quantity is reached in the envelope, similar to that of the protoplanet's core, the atmosphere's Kelvin-Helmholtz cooling time begins. Essentially, this is the time it takes for the gas present in the envelope to fall towards the core, making room for more gas from the disk to fill the envelope in the Hill sphere (Piso and Youdin, 2014). At the same time, as the protoplanet begins to generate a massive gas envelope, it opens gaps or cavities wide enough to mitigate the accretion of planetesimals and pebbles, so it only interacts with the remaining gas within the gap in its orbit. When the atmosphere reaches a mass similar to or greater than the heavy core, this cooling stage reaches its peak, beginning a rapid gas accretion process, where the material passes directly from the envelope to the protoplanet's atmosphere (Ikoma, Nakazawa, and Emori, 2000). This runaway process lasts depending on the amount of gas available in the vicinity of the protoplanet's Hill sphere influence, obtaining a final mass once the gas present in the gap is depleted (Goodman and Rafikov, 2001).

1.6   Protoplanetary Disks

1.6.1   Substructures in Protoplanetary Disks

Since the inception of the Atacama Large Millimeter Array (ALMA) radio telescope, investigations into planet formation and protoplanetary discs have undergone an exponential surge. ALMA's exceptional angular resolution, achieving $\theta_{\mathrm{res}} < 0.1"$, coupled with its extensive frequency coverage spanning from 40 GHz to 870 GHz in 10 bands, enables unprecedentedly detailed observations of both continuum and spectral lines. Moreover, the 66 antennas comprising the interferometer endow ALMA with productivity and efficiency orders of magnitude higher than previous instruments, facilitating

observations with equivalent sensitivity in mere minutes, a task that would
have taken hours or even days with previous telescopes.

This study harnesses ALMA's ultra-high angular resolution and exceptional sensitivity to scrutinize protoplanetary discs within exposure times of
less than a minute. Notably, the pioneering observation of the proto-star HL
Tau by ALMA (ALMA Partnership et al., 2015) marks a significant milestone
in the field. HL Tau, classified as Class I-II, presented humanity with unprecedented morphological details of a protoplanetary disc, unveiling multiple rings, gaps, and a luminous inner disk characterized by heightened material density. This seminal image laid the foundation for the comprehensive
understanding of planet formation that has evolved over the ensuing decade.

Subsequently, building upon the success of HL Tau, the Disk Substructures at High Angular Resolution Project (DSHARP) conducted the first largescale observation program of protoplanetary discs (Figure 1.11), specifically
targeting Class II sources (Andrews et al., 2018). The DSHARP survey produced high-resolution (3 au) continuum images of 20 protoplanetary discs,
revealing a plethora of substructures including gaps, rings, spiral arms, asymmetries, and dense dust clumps. Detailed analysis by Huang et al. (2018a)
elucidated that many of these observed substructures likely arise from interactions between protoplanets and the disc in a low-viscosity regime, affirming theoretical predictions.

1.6.2   Evolutionary Path for Protoplanetary Disks

In section 1.4.1, we presented examples of a significant portion of the Protoplanetary Disks (PPDs) observed with high angular resolution, detecting the
presence (or absence) of well-defined substructures, and spatially resolving
their morphology, size, or distance from the central source.
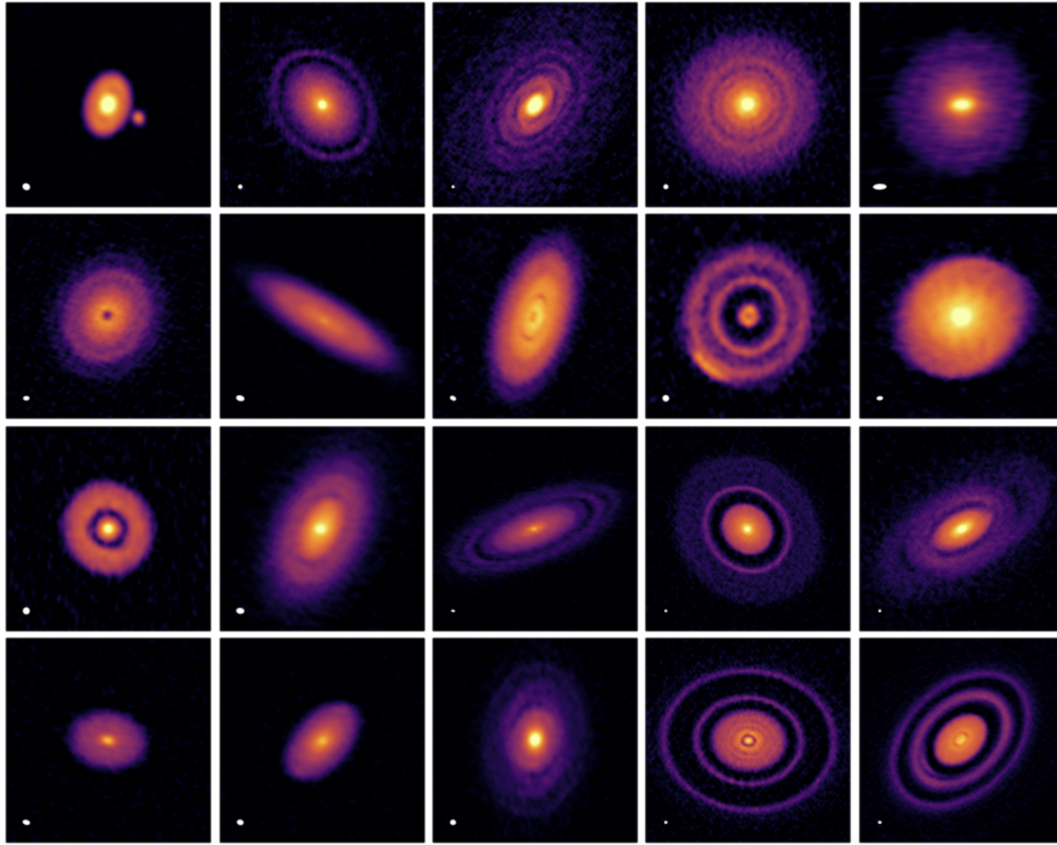
FIGURE 1.11: Continuum images for the 20 disks present in the DSHARP survey. It is possible to observe a big variety of sub structures, like spiral arms, bright clumps, ring, gaps, cavities, and multiple systems. This was the first ALMA large program of PPDs in high angular resolution. Figure from Andrews et al. (2018).

Most observational projects have aimed to understand the physical phenomena capable of shaping disk substructures, primarily focusing on Class II objects. These objects exhibit a greater variety of morphologies and have less contaminating material from envelopes or outflows, making them preferable targets for study.

Despite efforts, our understanding of PPD evolution remains limited, with a lack of high-angular-resolution observations ($\lambda_{\text{res}} < 0.1"$) for Class 0, I, or FS sources. Additionally, the proportion of these young sources is considerably lower compared to Class II sources in nearby Star Forming Regions (distances ≤ 300 pc).

As part of the ODISEA project, Cieza et al. (2021) present a sample of 10 Young Stellar Objects (YSOs) in the Ophiuchus molecular cloud, spanning

Classes I, FS, and II. Their observations, conducted at a spatial resolution of 3-5 au, provide valuable insights into bright disks at various evolutionary stages, proposing an evolutionary sequence for substructures within proto-planetary disks (Figure 1.12).

Assuming that most substructures are generated by protoplanets, Figure 1.9 proposes a sequence where Class I disks typically lack discernible sub-structures, such as rings, gaps, or spiral arms (also observed by Ohashi et al., 2023), due to the absence or insufficient mass of protoplanets to carve the disk. However, evidence suggests that bodies such as mini-Neptunes or Earth-mass planets could produce detectable structures (Pérez et al., 2019; Rosotti et al., 2016; Dong et al., 2017).

As planets accrete material from the disk and increase in mass, they open larger gaps and produce dense accumulations of material (bright rings) in the outer disk regions (Casassus et al., 2013). Multiple rings in early stages merge into a single ring with a halo of material, while the inner disk cavity shrinks with material accretion towards the central source (e.g., Elias 2-24 and DoAr 44).

Ultimately, only a bright ring of material remains, with an indiscernible inner compact disk, trapping material from the disk's periphery. Material between the ring and the source is accreted by the star or planets, akin to rocky bodies in the Solar System. This morphology persists until Class III disks, debris disks, where the ring's material compacts, forming a structure analogous to the Kuiper belt (e.g. White et al., 2017; Matrà et al., 2019).

1.7   Thesis Outline

Using ALMA observations at band 6 (1.3 mm), at angular resolutions of 1.1", 0.2", and 0.03" ($\sim$ 154, 28, and 5 au, respectively), the objective of this thesis is to study structures at different spatial scales around Young Stellar Objects
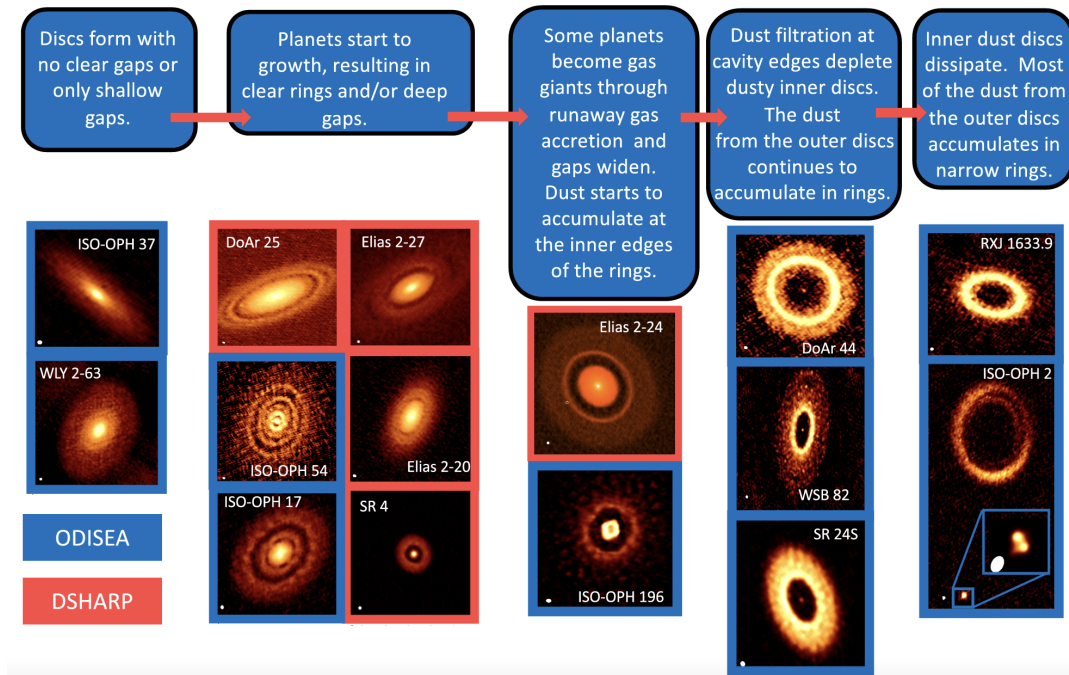
FIGURE 1.12: Proposed evolutionary path for the observable substructures, in the continuum, present in PPDs. At the begining, there are disks with not evident gaps or rings, moving to formation of first substructures, ending with bright rings and large cavities. Figure from Cieza et al. (2021).

(YSOs) of Class I, FS, and II disks. These structures, previously described in this introduction, are observed both on large scales (envelopes, outflows, and/or streamers) and on disk dimensions (rings, gaps, cavities, etc.). For more extended material structures, mainly molecular line observations will be used, including ^{12}CO, ^{13}CO, C^{18}O (2-1). For substructures related to protoplanetary disks, wavelengths relative to continuum emission will be utilized. The details of each observation and the methodology used for their analysis are described in each chapter. The different topics are organized as follows:

Chapter 2 discusses continuum observations for circumstellar disks around sources in the sub-stellar regime, present in the ODISEA survey. It also discusses and analyzes the morphological and physical properties of large-scale structures observed in molecular lines in these proto-Brown Dwarf Candidates. Additionally, it compares the emission properties, both dust and gas, among sub-stellar sources of different IR classes.

Chapter 3 analyzes in-depth the ISO-Oph 2 system, consisting of a wide

binary at a distance of 240 au. This system is composed of the longest and shortest cavity observed in the Ophiuchus cloud to date. Using available observations at different angular resolutions for the continuum, the sizes of the cavities, the asymmetries of the rings, and all possible morphological parameters for each source are measured. In the case of lines, various image processing methods are employed to avoid contaminating cloud emission and to observe the gas related to each source and the entire system.

Chapter 4 summarizes and concludes the most impactful results of each chapter and discusses the current premises regarding the evolution of material around YSOs based on the discussions of each chapter. Additionally, it reflects on and proposes future observations and analyses to better understand the evolution of YSOs in different galaxy SFRs, as well as to link these projects with potential new discoveries related to planet formation.

Chapter 2

The Ophiuchus DIsc Survey Employing ALMA (ODISEA)-IV: Analysis of Young Proto-Brown Dwarf Candidates

2.1 Abstract

The formation of brown dwarfs (BDs) remains an unresolved puzzle. Several BDs formation scenarios have been proposed in the literature. In order to better understand those mechanisms and the predominant one we need to study young BDs, when they are still embedded in their parental cloud, in a phase analogous to the protostar stage in the low-mass stars regime. In the context of the "Ophiuchus Disc Survey Employing ALMA" (ODISEA), we selected a subsample containing all class I and Flat Spectrum proto-brown dwarf (proto-BD) candidates to study the distribution of gas and dust surrounding them. As a result we found that out of a total of 21 objects, 16 exhibit extended continuum emission. Additionally, 12 sources show molecular emission in ^{12}CO, ^{13}CO, and/or C^{18}O (2-1), close to the central source, either tracing rotating disks, outflows, or possible streamers or envelopes. Compared to Class II proto-BDs within the Ophiuchus region, we observe a higher detection rate among younger classes (I and FS) relative to the total young stellar object (YSO) population. This prevalence of material surrounding proto-BD candidates suggests an extended lifetime, particularly during early substellar stages. Our findings shed light on the evolutionary timescales and formation mechanisms of substellar objects within Ophiuchus star-forming region.

2.2 Introduction

In recent years, the study of protoplanetary disks (PPDs) has undergone exponential growth. High-resolution observations have provided unprecedented insights into these objects, revealing structures and features (ALMA Partnership et al., 2015) that were previously beyond observational reach

(Kwon, Looney, and Mundy, 2011) just over a decade ago. Much attention has been directed towards achieving very high angular resolution images of young stellar objects (YSOs) (e.g., Andrews et al. 2018; Cieza et al. 2021; Garufi et al. 2022; Rich et al. 2022) and conducting statistical analyses across various star-forming regions (SFRs) such as Lupus (Ansdell et al., 2016), Chameleon (Pascucci et al., 2016), Taurus (Andrews et al., 2013), Upper Sco (Barenfeld et al., 2016), σ-Orionis (Ansdell et al., 2017), among others.

Within this context, the ODISEA project (Cieza et al., 2019) emerged, leveraging the capabilities of the Atacama Large Millimeter/submillimeter Array (ALMA) radio telescope to survey all YSOs previously cataloged in the c2d project (Evans et al., 2009) within the Ophiuchus molecular cloud. Notably, Ophiuchus stands out due to its proximity to our solar system (140 pc on average) and its relatively young age of 1-2 Myr (Wilking, Gagné, and Allen, 2008), and observable by ALMA in the southern hemisphere, making it a valuable target for understanding YSO and protoplanetary disk evolution. It is noteworthy that Ophiuchus hosts one of the highest concentrations of IR I and Flat Spectrum (FS) class objects among nearby SFRs (Evans et al., 2009).

The prevalence of early-stage YSOs in Ophiuchus offers a unique opportunity to study the primordial environments where protostars and protoplanetary disks first form. According to current star formation theories, prestellar cores initially coalesce in dense regions of molecular clouds (Ward-Thompson et al., 1994), gradually accreting material to form a protostar with surrounding gas and dust circumstellar disk and envelope (Shu, Adams, and Lizano, 1987). As nuclear fusion ignites within the protostar, powerful jets emerge, piercing through and shaping the surrounding envelope (Bally, Reipurth, and Davis, 2007). Over time, these jets heat the envelope material, triggering the generation of bright outflows (Ray et al., 2007), which progressively carve out larger and denser structures as they excavate the envelope

(Arce et al., 2007). Despite the apparent coherence of this evolutionary process, the linearity and duration of its stages remain subject to ongoing investigation (Takami et al., 2018; Takami et al., 2019), necessitating further scrutiny of YSOs in their early formation stages and the large-scale spatial structures (> 1000 au) enveloping them.

The material enveloping YSOs not only influences the formation and evolution of protoplanetary disks, but also dictates the accretion process onto the protostar, consequently impacting the final stellar mass (Hartmann, Herczeg, and Calvet, 2016). Various mechanisms regulate the accretion rates onto protostars (e.g.,Tsukamoto et al. 2023), dispersing material (Hasegawa et al., 2022) or inflowing it (Mottram et al., 2013), with a comprehensive understanding of these mechanisms enabling extrapolation of the final masses of YSOs and, by extension, the amount of material within protoplanetary disks capable of forming planetary systems. Studies have revealed correlations between accretion rates and protostellar masses (e.g., Lodato et al. 2017; Somigliana et al. 2022), offering insights into future stellar properties such as temperature, luminosity, and mass. Moreover, protostellar properties play a crucial role in understanding their interaction with surrounding material envelopes, thereby facilitating the precise interpretation of related observations, including envelopes, infalling streamers, disk winds, outflows, and inflows, that have been previosly modelled with stellar population interacting simulations (Hirano and Yoshida, 2013).

Despite the predominance of YSOs within certain mass ranges in observational studies, significant numbers of very low mass sub-stellar sources, including Brown Dwarfs (BDs), with masses $\lesssim 0.1$ M$_\odot$, have been identified in the Milky Way (e.g. Mužić et al., 2017). These objects, incapable of sustaining hydrogen fusion due to their low masses (below 0.07 M$_\odot$), only undergo deuterium fusion, resulting in extremely low temperatures (2200 - 250 K) that render them almost undetectable in the optical range. The origin

of BDs remains a topic of active debate, with proposed scenarios suggesting either a scaled-down version of the star formation process or the ejection of sub-stellar objects from protoplanetary disks due to gravitational fragmentation (Reipurth and Clarke, 2001; Stamatellos and Whitworth, 2009; Machida, Inutsuka, and Matsumoto, 2009). Regardless of the specific formation mechanism, observations of exoplanets orbiting BDs suggest the possibility of sub-stellar objects having their own circumstellar material disks at some point during their formation.

Recent investigations have shown proto-BDs accompanied by protoplanetary disks (e.g. Testi et al., 2016; Santamaría-Miranda et al., 2021; Riaz and Bally, 2021) and extended material structures such as outflows and jets (e.g. Santamaría-Miranda et al., 2020; Riaz and Machida, 2021). However, despite these findings, conclusive evidence supporting a specific formation scenario for sub-stellar objects remains elusive.

Within the framework of the ODISEA project, we have identified 21 candidate proto-BDs of classes I and FS (Section 2.3). These candidates were analyzed using observations at varying angular resolutions (Section 2.4), with image synthesis parameters modified from those originally published by Cieza et al., 2019. Our analysis includes the detection of continuum emission (1.3 mm or 228 GHz) from 16 of these sources (Section 2.5.1), and the identification of gas emissions in lines of ^{12}CO, ^{13}CO, and C^{18}O (2-1) in 12 proto-BD candidates (Section 2.5.2). Furthermore, we estimated disk masses ($M_{disk} = M_{dust} + M_{gas}$) for sources with continuum detections, described the observed gas structure morphologies by measuring all available physical parameters, and compared these measurements with those of class II proto-BDs (Testi et al., 2016) also present in Ophiuchus (Section 2.6).

2.3 Sample selection

Starting from the YSOs in Ophiuchus, detected and cataloged in the c2d program (Evans et al., 2009), with their respective measured infrared classes, the ODISEA survey (Cieza et al., 2019) observed ∼300 sources with the 12m array of the ALMA observatory. Using the same proto-brown dwarfs selection criteria employed by Testi et al. (2016), and based on the spectral definition of brown dwarfs (BDs), we have selected all sources with a spectral index equal to or later than M6 as possible proto-BD candidates within the ODISEA survey. Additionally, using infrared data from the FIRE instrument at Las Campanas Observatory (LCO), we applied the BT-Settl spectral models for low-mass stellar objects, obtaining estimations of their spectral indices (Ruíz-Rodríguez et al. in prep).

In table 2.1, we present the source selection parameters, along with their respective literary references and spectral estimates from FIRE's spectrum observations. The final sample consists of 21 potential sub-stellar object candidates, where the majority of the spectral indices are consistent between the literature and the estimates from Ruíz-Rodríguez et al. (in prep). In some cases, a precise spectral index estimate was not found, but objects previously classified as proto-BDs, BD candidates (BDc), and likely substellar were included.

For the Class II sources present in the ODISEA survey that follow the criteria mentioned as proto-BDc, all of them are already described in Testi et al. (2016) and Ruíz-Rodríguez et al. (2022), and it was not possible to obtain additional lines or continuum detections beyond those already mentioned in the literature.

Fig.2.1 displays the observed column density map obtained by the Herschel Space Telescope. This figure is analogous to the one published by Ladjelate et al. (2020), with the positions of each source from this study overlaid.

It is noticeable that a significant number of sources are immersed in regions of high column density. Therefore, one can anticipate observing substantial contamination or absorption originating from the cloud in the channels corresponding to the systemic velocity of the Ophiuchus molecular cloud (André et al., 2007).

2.4   Observations and data reduction

The observations presented here are part of ODISEA project (Cieza et al., 2019) observed by ALMA (PID: 2016.1.00545.S). The data is divided into two different array configurations, which provided $\sim 0.2''$ and $\sim 1.1''$ angular resolutions. Both antenna's configurations include 5 spectral windows, 2 dedicated to observe continuum emission, centered at 218.998 and 232.014 GHz, and 3 more for detecting molecular emission from the transitions ^{12}CO, ^{13}CO and C^{18}O (2-1) at 230.544, 220.404 and 219.566 GHz respectively, with 30 kHz (~ 0.04 km s^{-1}) spectral resolution. Data reduction was made entirely using the CASA software (McMullin et al., 2007) version 5.8.0. Continuum and line imaging were performed with the task TCLEAN, using the multiscale deconvolver. Self-calibration process was not applied, because there is not improvement in SNR for the continuum images and line cubes. For the continuum results we used both spectral windows centered at 218.998 and 232.014 GHz, the C40-5 antenna's configuration data, and natural 2.0 weighting to improve the sensitivity, and to confirm disk detections in Cieza et al. (2019), at higher SNR (Table 2.2). For the molecular emission lines, the dataset's combination of different array configurations decreased the SNR, and diluted the extended emission surrounding the central source. Therefore in this paper we just considered the data from the C43-2 antenna's configuration (Table 2.2). Natural weighting, robust 2.0 and 0.1 km s^{-1} channel width were used to produce the final data cubes. A high percentage

TABLE 2.1: Sourcenames; Right ascension; Declination; Distances from Gaia DR3, and for sources without Gaia parallaxes, an average distance of 140 pc from Ortiz-León et al. (2018); IR classes from c2d survey (Evans et al., 2009); Spectral type from references; Effective temperature from references; Mass of the star from references; References: (1) Ruíz-Rodríguez et al. (in prep), (2) Alves de Oliveira et al. (2012), (3) Doppmann et al. (2005), (4) Esplin and Luhman (2020), (5) Manara et al. (2015), (6) Geers et al. (2011), (7) Riaz and Bally (2021).

Source name	α (J2000)	δ (J2000)	Distance (pc)	IR Class	Spectral type	T_{eff} (K)	M_{star} M_*	References
2MASS J16230686-2257367	16:23:06.867	-22:57.36.75	137±20	FS	M8	2800	-	(1)
BKLT J162546-242337	16:25:46.629	-24:23.36.11	140	FS	L5 / Polluted	2000	-	(1) / (2)
BKLT J162610-243353	16:26:09.932	-24:33.54.08	141±5	I	M6	2800	-	(1)
CRBR 2315.8-1700	16:26:17.229	-24:23.45.37	140	I	M8 / M2	1700/3600	-	(1) / (3)
CRBR 2317.5-1729	16:26:18.982	-24:24.14.26	140	FS	M6	-	0.135	(4)
[RR90] Oph 2320.8-1721	16:26:22.269	-24:24.07.06	140	FS	M8 / M8	2600/2700	0.037	(1) / (5)
[GY92] 154	16:26:54.771	-24:27.02.25	140	FS	M6 / M6.5	2800	0.064	(1) / (4)
[GY92] 197	16:27:05.246	-24:36.29.79	140	I	L8	1600	-	(1)
WLY 2-35	16:27:15.514	-24:30.53.68	140	FS	L9	1500	-	(1)
ISO-Oph 150	16:27:30.912	-24:27.33.20	140	I	L6	1800	-	(1)
BBRCG 58	16:27:32.138	-24:29.43.57	140	FS	M6	-	0.115	(4)
2MASS J16274178-2442346	16:27:41.788	-24:42.34.60	140	FS	Likely substellar / L7	1700	-	(1) / (6)
[GY92] 344	16:27:45.787	-24:44.53.86	140	I	M6 / M6	2800	0.033	(1) / (2)
2MASS J16274825-2442256	16:27:48.25	-24:42.25.6	140	I	Likely substellar	-	-	(6)
BKLT J162858-244054	16:28:57.869	-24:40.54.92	140	I	L2-BDc	1700	-	(1)
2MASS J16312923-2404311	16:31:29.24	-24:04.31.1	134±7	FS	M8	2700	-	(1)
2MASS J16313383-2404466	16:31:33.83	-24:04.46.6	140	I	M6	2800	-	(1)
2MASS J16313679-2404200	16:31:36.80	-24:04.20.1	140	I	Proto BD	-	-	(7)
ISO-Oph 200	16:31:43.763	-24:55.24.548	140	I	Proto BD	-	-	(7)
ISO-Oph 204	16:31:52.111	-24:56.15.67	140	FS	M8	-	-	(1)
WLY 2-69	16:32:21.052	-24:30.35.83	140	FS	L1	-	-	(1)
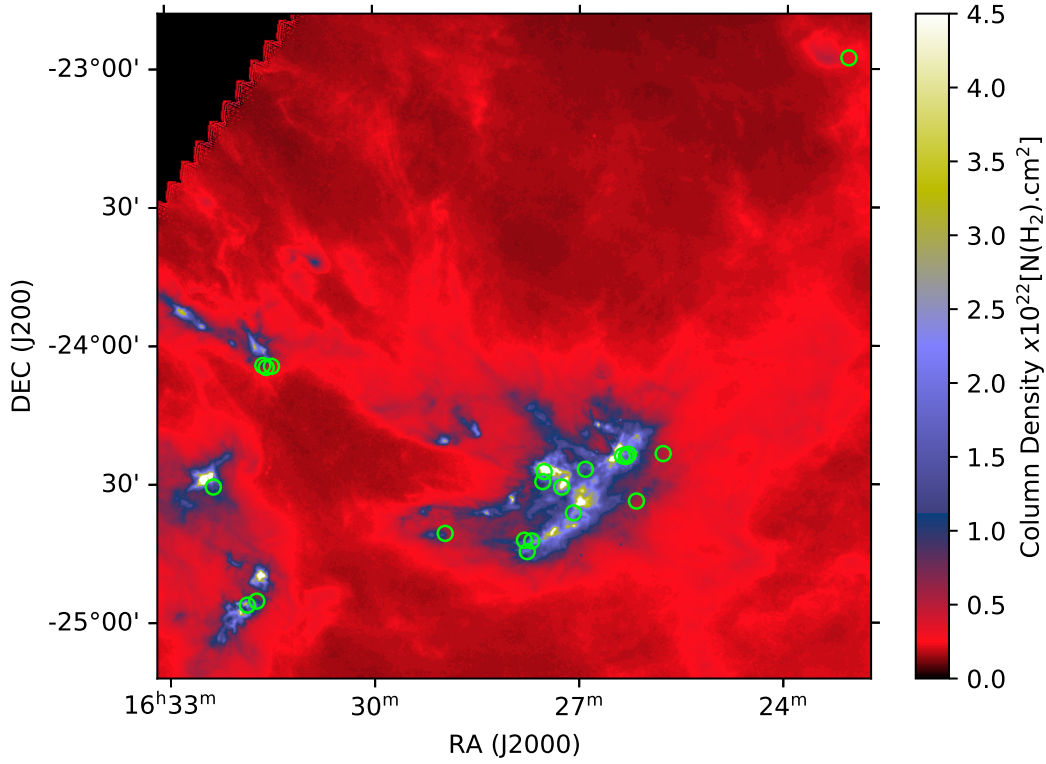
FIGURE 2.1: Coordinates of proto brown dwarfs candidates in the sample (green circles), within Ophiuchus molecular cloud. The background corresponds to H_2 column density map, from Herschel Gould Belt Survey, for the L1688 (Ophiuchus) region.

of sources exhibit significant contamination at speeds associated with the molecular cloud, between ~ 2 and 4 km s^{-1}. Consequently, various strategies were employed to mitigate this emission. These included the application of UVTAPPER and UVRANGE tools. However, the outcomes did not align with expectations. Not only did these interventions decrease the detection sensitivity of extended emissions within the field of view (FoV) originating from the cloud, but they also diminished the contrast of extended emissions associated with the sources. Consequently, the resultant products derived from the utilization of these CASA tools were deemed unsuitable for further analysis.

TABLE 2.2: Observational information from the QA2 ALMA report, considering the execution block, array configuration (Array Config.), number of antennas (N Ant.), date, time on source for the complete 147 sources (ToS), average elevation (Avg. Elev.), mean precipitable water vapor (Mean PWV), baselines length range, angular resolution (AR) and maximum recoverable scale (MRS)

Execution Block	Array Config.	N Ant.	Date	ToS [sec]	Avg. Elev. [deg]	Mean PWV [mm]	Baselines [m]	AR ["]	MRS ["]
uid://A002/Xc20718/X353	C40-5	45	13-Jul-2017	5020	-	1.9	16.7 - 2647.3	0.2	2.0
uid://A002/Xc20718/Xb1c	C40-5	45	13-Jul-2017	4467	74.6	1.8	16.7 - 2647.3	0.2	2.0
uid://A002/Xc20718/X4a8c	C40-5	42	14-Jul-2017	4489	-	1.1	16.7 - 2647.3	0.2	2.0
uid://A002/Xcde1cf/X3966	C43-2	45	26-May-2018	4550	73.1	1.1	15 - 313.7	1.1	10.7

2.5 Results

2.5.1 Continuum

From the complete sample of 21 young substellar candidates, 16 of them were detected in the continuum (Fig.3.2). It can be observed that the vast majority exhibit bright emission (>10× SNR), with green contours starting from 3× rms in each panel of Fig.3.2. Using the IMFIT tool from CASA to the continuum images (Fig.3.2), we obtained the results shown in table 2.3. In contrast to what might be observed in the continuum images (Fig.3.2), only 2 sources are spatially resolved at this resolution with the deconvolved beam, 7 are unresolved but with estimated sizes, and the remaining 7 do not have sufficient size or SNR for IMFIT to find values for the size, so they are defined as point sources.

In this case, degrading the angular resolution and increasing the SNR, Fig.2.3 shows the detection of two wide binary systems that were not detected nor published by Cieza et al. (2019). For ISO-Oph 204, its faint companion GBS-VLA J163151.93-245617.4 is already detected in different wavelengths (Ratzka, Köhler, and Leinert, 2005; Cieza et al., 2009; Zurlo et al., 2020), it is classified as a YSO, part of the Ophiuchus molecular cloud (Ortiz-León et al., 2018). On the other hand, WLY 2-69 has a companion, 2MASS J16322081-2430290, which is a YSO previously detected by Spitzer (Gutermuth et al., 2009) and ALMA (Cox et al., 2017). However, the 2MASS J16322081-2430290 source is not bright enough to be detected with the imaging parameters used in Cieza et al. (2019). The literature information is insufficient to classify either of those companions, GBS-VLA J163151.93-245617.4 and 2MASS J16322081-2430290, in the substellar regime.

In order to estimate the mass evolution of these proto-brown dwarf candidates, we determined estimates for the mass of the dust surrounding the host source. Similarly to the approach taken by Williams et al. (2019), the

simplest way to obtain a dust mass value is by assuming an optically thin behavior of the emission, a homogeneous temperature, T_{dust} = 20 K, across the disk, and an opacity coefficient of $\kappa_\nu = (\nu/100$ GHz$)$ cm^{2}g^{-1}. Given the above, and assuming the submillimeter regime of the observations presented in this work, the equation for M_{dust} would be as follows:

$$M_{dust} = \frac{F_\nu d^2}{\kappa_\nu B_\nu(T_{dust})} = 0.592 M_\oplus \left(\frac{F_{225\text{GHz}}}{1 \text{ mJy}}\right) \left(\frac{d}{140 \text{ pc}}\right)^2 \qquad (2.1)$$

where the $F_{225\text{GHz}}$ corresponds to the continuum flux from the concatenation of both, 218.998 and 232.014 GHz, spectral windows, and d the distances in table 2.1. Then, considering equation 2.1, the estimated masses for the dust, within protoplanetary discs in the sample, vary from <1 to ~45 $M_\oplus$. The undetected sources in the continuum have a flux < 0.2 mJy, so despite they are not included in Table 2.3, we consider an upper limit on mass of 0.12 $M_\oplus$ for the dust around non detections.

2.5.2   Molecular lines

In the context of our sample, a total of 12 proto BD candidates manifest discernible line emissions interacting with the main source, with 11 exhibiting continuous emission and a solitary target demonstrating only the emission of ^{12}CO ([GY92] 344). The quantified flux values corresponding to the distinct molecular lines (^{12}CO, ^{13}CO, and C^{18}O) are tabulated in table 2.4. These values are derived through the integration of channels that show line emission $\geq 3 \times$ rms. We only considered structures surrounding the central source, excluding features associated to cloud contamination.

Appendix figures (Fig. 2.19 to 2.30) portray channel maps associated with ^{12}CO emission related to the central sources. Contoured in white are the delineated zones deemed pertinent for gauging the total integrated line flux showed in 2.4.

TABLE 2.3: Measurements for continuum detections. All parameters presented were obtained using the IMFIT tool.

Source name	F_{peak} [mJy Beam^{-1}]	rms [mJy Beam^{-1}]	SNR	F_{total} [mJy]	M_{dust} [$M_\oplus$]	M_{gas} [M_{Jup}]	Bmaj × Bmin [$'' \times ''$]	PA [deg]	Beam Size [$'' \times ''$]
2MASS J16230686-2257367	0.46 ± 0.05	0.08	5.8	0.46 ± 0.1	0.24	0.07	-	-	0.33 × 0.25
BKLT J162546-242337	7.63 ± 0.09	0.08	95	27.1 ± 0.4	16.04	5.05	0.94 × 0.16	114	0.33 × 0.25
CRBR 2315.8-1700	42.4 ± 0.2	0.16	265	75.9 ± 0.5	44.93	14.13	0.31 × 0.19	142	0.33 × 0.25
CRBR 2317.5-1729	21.5 ± 0.1	0.09	239	30.7 ± 0.2	18.17	5.72	0.21 × 0.16	123	0.33 × 0.25
[GY92] 154	1.34 ± 0.05	0.09	15	1.34 ± 0.08	0.64	0.2	-	-	0.33 × 0.25
[GY92] 197	25.7 ± 0.2	0.17	151	54.6 ± 0.5	32.32	10.17	0.42 × 0.13	168	0.33 × 0.25
WLY 2-35	0.52 ± 0.06	0.08	6.5	0.62 ± 0.11	0.37	0.12	0.15 × 0.09	121	0.33 × 0.25
BBRCG 58	4.02 ± 0.07	0.09	45	4.2 ± 0.1	2.49	0.78	0.07 × 0.04	88	0.33 × 0.25
2MASS J16274825-2442256	0.84 ± 0.15	0.14	6	1.4 ± 0.4	0.83	0.26	-	-	0.33 × 0.25
BKLT J162858-244054	2.72 ± 0.1	0.14	19	2.9 ± 0.2	1.72	0.54	0.09 × 0.07	135	0.33 × 0.25
2MASS J16312923-2404311	0.84 ± 0.11	0.14	6	1 ± 0.2	0.54	0.17	-	-	0.33 × 0.25
2MASS J16313383-2404466	1.5 ± 0.1	0.14	11	1.7 ± 0.2	0.96	0.3	-	-	0.33 × 0.25
2MASS J16313679-2404200	10.6 ± 0.1	0.14	76	14.2 ± 0.2	8.41	2.65	0.27 × 0.04	78	0.33 × 0.25
ISO-Oph 200	8.9 ± 0.1	0.14	64	9.4 ± 0.2	6.39	2.01	-	-	0.33 × 0.25
ISO-Oph 204	39.4 ± 0.2	0.18	219	45.6 ± 0.4	32.24	10.14	0.12 × 0.1	5	0.33 × 0.25
WLY 2-69	15 ± 0.14	0.15	100	15.7 ± 0.3	11.25	3.54	-	-	0.33 × 0.25
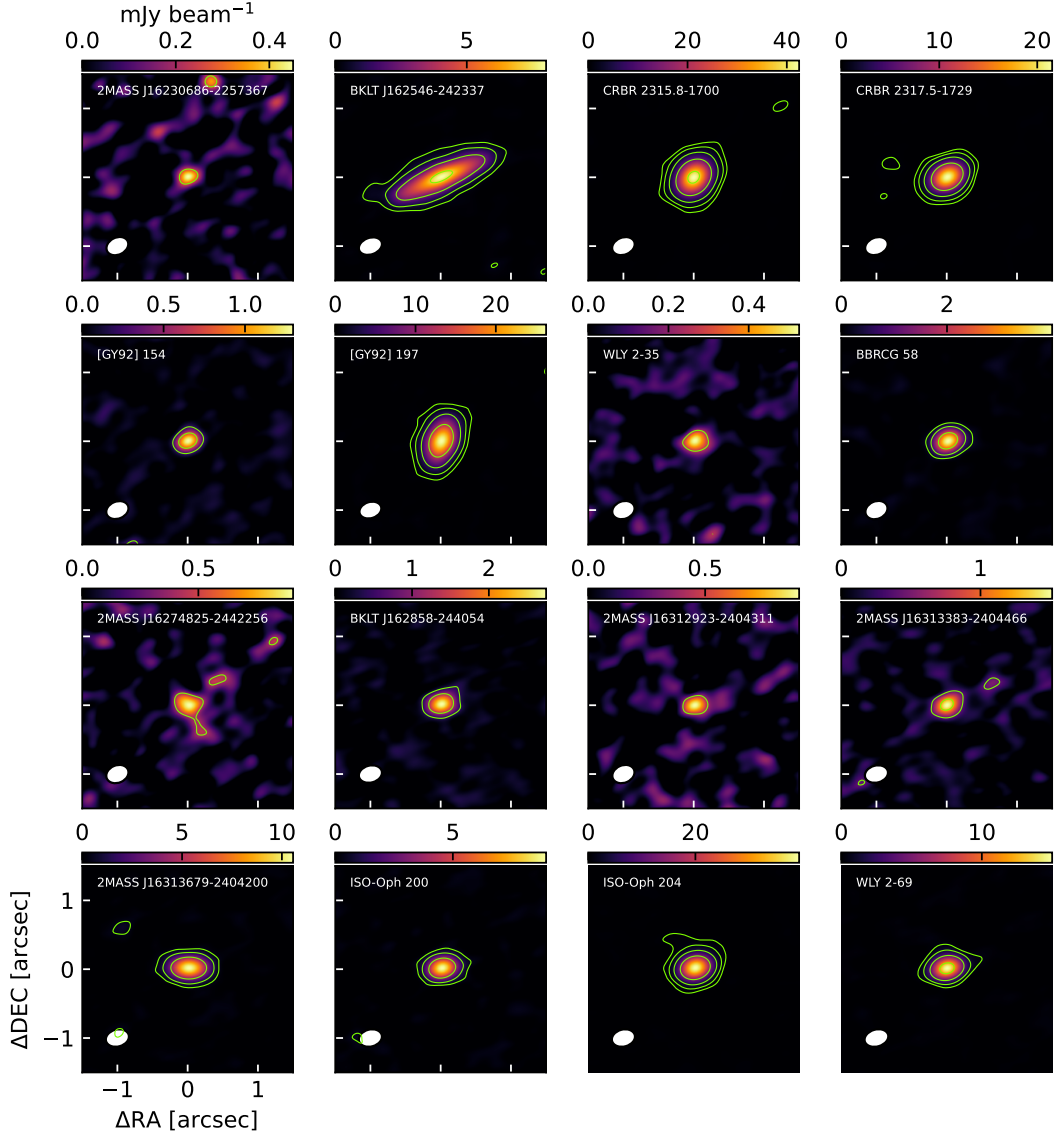
FIGURE 2.2: Continuum ALMA images for 16 detected proto brown dwarfs candidates at 1.3 mm. The synthesized beam size (in white) is presented in the left bottom corner of each panel. The green contours correspond to $[3, 9, 27, 81, ...]\times$ rms for each image.

To discuss the morphology and kinematics of the gas structures, integrated flux maps (moment 0) and velocity maps (moment 1) are presented for each source with associated line emission. These maps were generated using the BETTERMOMENTS library (Teague and Foreman-Mackey, 2018), employing a smoothing of 3 channels wide for the cubes, and a clipping procedure in the moment 1 maps, to remove all pixels with values below $[10, 5, 3] \times$
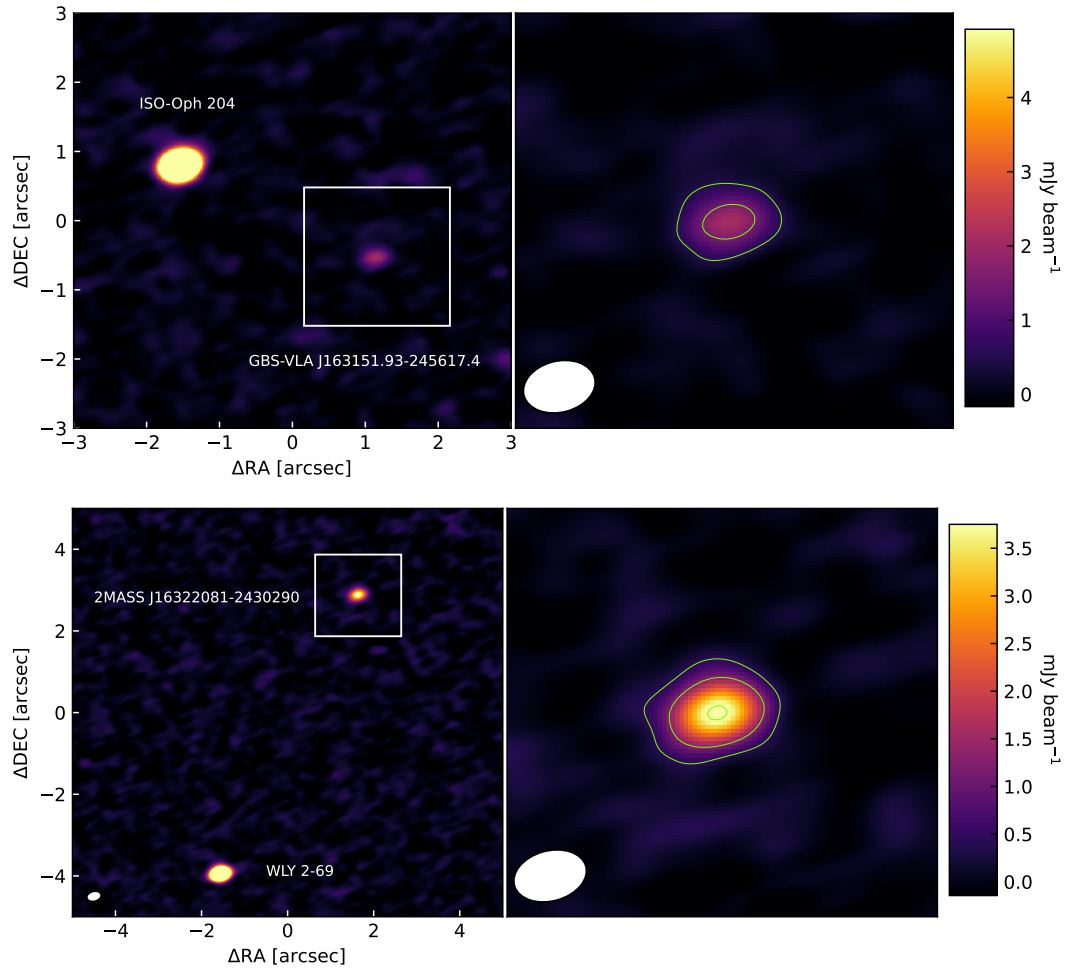
FIGURE 2.3: Multiple systems from the same observations pre-
sented in Fig. 3.2. Left panels: Wide binary systems. Right
panels: Zoom in corresponding to white squares in for the re-
spective left panel. Green contours have the same levels than
Fig. 3.2. The synthesized beam size (in white) is presented in
the left bottom corner of right panels.

rms for ^{12}CO, ^{13}CO and C^{18}O lines respectively.

The calculated gas masses, outlined in table 2.3, represent an estimated ratio of the dust mass, scaled by a ratio of $M_{gas}/M_{dust} = 100$, assuming same proportions than ISM (Bohlin, Savage, and Drake, 1978). For instances where the detection of ^{13}CO and C^{18}O is viable, and assuming an optically thin behavior for these lines, grid models derived from Williams and Best (2014) are applied to estimate the gas mass, considering the ^{13}CO/ C^{18}O ratio pertinent to the corresponding ^{12}CO flux regime.

This section is compartmentalized into a morphological elucidation of observed structures for each source, accompanied by a detailed description of measurable gas parameters unique to each case within the respective subsection.

BKLT J162546-242337

In figure 3.4, the ^{12}CO emission is strongly contaminated for a cloud stream, crossing the fov north-east to south-west (e.g: Fig.2.19 at 1.7 km s^{-1}). Cloud emission could easily be confused by a monopolar extended outflow in the plane of the sky in the blue shifted velocities, due the short velocity range of mentioned extended emission ($\sim$2 to 2.5 km s^{-1}) is consistent with the cloud systematic velocity, we keep just flux with longer range velocity, mainly related to the gaseous disk. Posterior channels show no emission $> 3\times$rms associated with the central source, with a range between 2.2 and 4.0 km s^{-1}. The red shifted velocities show the complementary side of the disk, and the possible inner part of an outflow.

Considering the redshifted velocities ranging from 4.2 to 5.1 km s^{-1} and the positions of the star and both ends of the extended emission, the opening angle of the outflow corresponds to 116º, and an extension of 4.2$''$ ($\sim$600 au) from the central object. For the blueshifted velocities between 0.8 and 1.2

TABLE 2.4: Measurements from the data cubes for the molecular lines ^{12}CO, ^{13}CO, and $C^{18}O$ (2-1). For the integrated fluxes (F_{line}), the units are [Jy km s^{-1}], for the root mean square (rms) it is [Jy beam^{-1} km s^{-1}], and for the velocity range [km s^{-1} - km s^{-1}].

Source name	$F_{^{12}CO}$	rms (^{12}CO)	$F_{^{13}CO}$	rms (^{13}CO)	$F_{C^{18}O}$	rms ($C^{18}O$)	Velocity range (^{12}CO)
BKLT J162546-242337	9.7	0.15	1.9	0.1	0.45	0.07	-0.1 - 6.4
CRBR 2315.8-1700	74.6	0.15	7.8	0.1	1.1	0.06	-0.6 - 2.5
CRBR 2317.5-1729	56.6	0.16	4.9	0.12	-	0.07	0.2 - 7.2
[GY92] 197	31.2	0.15	2.9	0.1	-	0.06	-1.0 - 8.8
[GY92] 344	7.5	0.11	-	0.09	-	0.07	0.9 - 6.6
2MASS J16274825-2442256	9.9	0.1	-	0.07	-	0.06	0.8 - 6.4
BKLT J162858-244054	1.4	0.1	0.2	0.09	-	0.06	1.8 - 3.1
2MASS J16313383-2404466	14.2	0.09	-	0.08	-	0.06	-0.5 - 4.8
2MASS J16313679-2404200	88.8	0.16	1.5	0.09	-	0.06	-2.0 - 6.2
ISO-Oph 200	120.3	0.1	10.4	0.06	2.2	0.04	-3.5 - 12.0
ISO-Oph 204	65.7	0.2	-	0.1	-	0.06	-1.4 - 6.8
WLY 2-69	34.5	0.12	7.4	0.05	-	0.03	1.1 - 7.8

km s^{-1}, in the contours of fig.2.19, tentative extended emission can be observed, which could correspond to the northern component of the outflows. However, it is not sufficiently bright, subsequently combined with cloud contamination, to measure the physical and morphological parameters of the outflow.

^{13}CO emission is related with the inner part of the gaseous disk. Similarly to the continuum, using the *imfit* tool, geometrical measurements for the gas disk are obtained, with parameters of 1.9" (bmaj), 0.78" (bmin), and a position angle of 92°. In fig.3.4, it can be observed that the 13CO disk emission aligns with the geometry of the continuum emission. Additionally, there is a clear gas rotation, with a peak emission at 2.1 km s^{-1} in the blueshift and another peak at 5.2 km s^{-1} in the redshift. The absence of emission and self-absorption of the cloud around the systemic velocity ($\sim$ 3.3 km s^{-1}) prevents the observation of a perfectly Keplerian rotation.

Unlike ^{13}CO, C^{18}O shows minimal emission $> 3\times$rms. In the velocity map (Fig.3.4; right-bottom panel), only a few channels in the blueshifted velocities exhibit emission, centered around 2 km s^{-1}. The detection of the blueshifted side of C^{18}O is morphologically and kinematically consistent with the gas disk of ^{13}CO (Fig.3.4; mid-bottom panel). In this case, due to the low emission, it is not possible to obtain geometric estimations of the C18O disk.

CRBR 2315.8-1700

Unlike most of the others gas-emitting sources, CRBR 2315.8-1700 exhibits a narrow range of emission velocities, between -0.6 and 2.5 km s^{-1}. Due to the aforementioned low sensitivity, there could be emission at higher velocities, but it is not detected in these observations.

In Figure 2.5 (left panels), extended emission in the ^{12}CO line associated with a rotating disk coinciding with the continuum emission is observed.

This extended structure is large-scale, extending beyond the field of view of the observations, i.e. >2800 au. For these observations, it is difficult to distinguish the nature of this large-scale spatial emission, but given its morphology, it resembles a gas streamer originating from the cloud (e.g. Pineda et al. (2020), Garufi et al. (2022), Gupta et al. (2023)). Kinematically, the gas emission in faster velocity channels (-0.6 to 0.5 km s^{-1}), it is in the vicinity of the dust disk (Fig.2.20), while the larger extended emission is closer to cloud velocities (0.7 to 1.7 km s^{-1} in this case). Those kinematics are consistent with what is expected for accreting material streamers from the molecular cloud to the protoplanetary disk and its host source (Gupta et al. (2024)). However, the velocities for this possible streamer are close to the cloud's velocity, so there could be emission unrelated to the system or a combination of contamination and an extended structure associated with the central source.

The rotation of the gas disk around CRBR 2315.8-1700 is clearly visible in the ^{13}CO line (Figure 2.5 ; middle-bottom panel), with a systemic velocity of 1.6 km s^{-1}. The gas disk has dimensions of 2.1" x 3.9" (200 au x 550 au) and a position angle of 117°, with a spatial orientation coinciding with the continuum emission. In addition to the disk, part of the extended emission similar to that present in the ^{12}CO line can also be observed, but it is less extensive and closer to the cloud's velocity, suggesting it might be partially cloud contamination.

Also present in the C^{18}O line, a more compact rotational disk is observed (Figure 2.5 ; right panels), spatially unresolved, with velocity ranges almost identical to the ^{13}CO emission.

CRBR 2317.5-1729

This source exhibits one of the most complex gas morphologies in the sample. For the case of ^{12}CO, it is possible to observe in fig.2.6 (left panels) that the
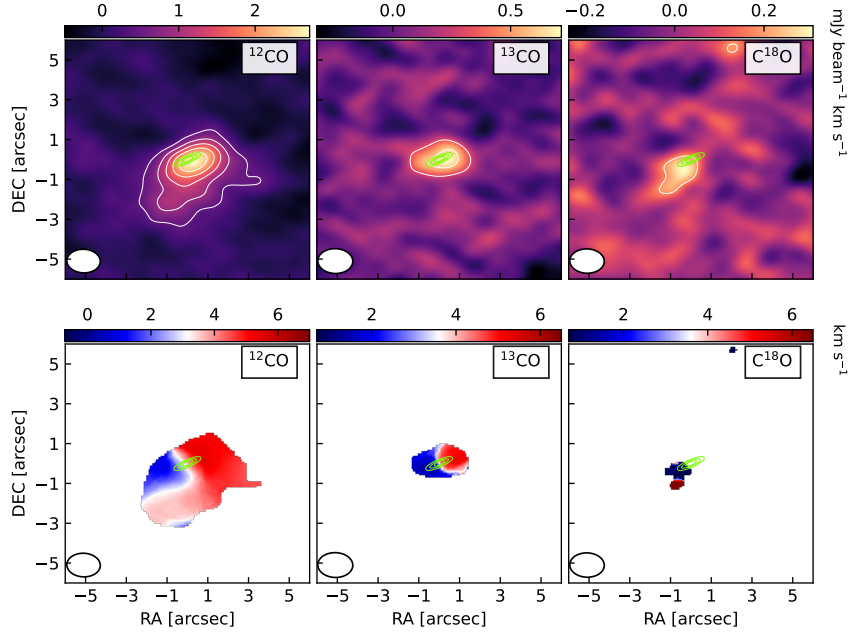
FIGURE 2.4: Top panels: Integrated intensity maps (moment 0). Bottom panels: Velocity maps (moment 1). Left to right: maps for ^{12}CO, ^{13}CO, and C^{18}O (2-1) lines. The maps correspond to the emission associated to BKLT J162546-242337 source. White countours represent the line emission at [3, 6, 9, 12, ...]× rms, and green contours are 100%, 75%, 50% and 25% of the peak, for the continuum (1.3 mm) emission. Beam sizes are presented in the bottom-left corner in each panel.
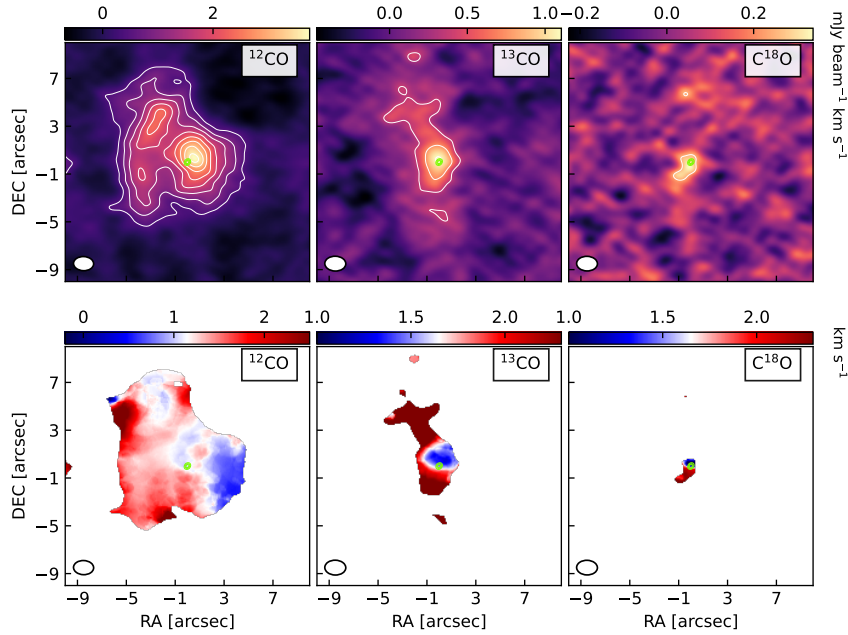
FIGURE 2.5: Maps of moments for CRBR 2315.8-1700, analogous to Fig. 3.4

line emission shows a possible bipolar outflow, detected with similar charac-
teristics for both the blueshifted and redshifted sides. In this case, the out-
flows have a narrow width of 3" or 520 au, and therefore, an opening angle
of 23°. Despite the thinness of the possible outflows, they have an extension
greater than 18" (> 2500 au). This morphology may suggest a young age for
the outflows, where the jets are just beginning to carve and interact with the
envelope (ref). A peculiarity of this extended emission is that there is a de-
crease in brightness between the compact emission, related to the disk, and
a distance of $\sim$4" (560 au) from the central source. This decrease in bright-
ness may be due to self-absorption of the cloud in those regions or periodic
material ejection pulses, generating non-uniform envelope heating (ref). The
velocity map (Fig.2.6; left-bottom panel) shows emission associated with the
disk, centered on the proto BD, only on the blueshifted side. The redshift
channels show the southwest component of the outflows, but only in its out-
ermost part, from $\sim$4" (560 au) away from the central source. In this case,
both outflows show an almost symmetrical morphology, with blueshifted
emission between 0.2 and 2.5 km s^{-1}, and then redshifted between 5.0 and
7.2 km s^{-1}. It is worth noting that there is significant contamination from the
cloud between the channels 4.4 and 5.2 km s^{-1}, west of the source (Fig.2.21).

In the ^{13}CO line, it is possible to observe the compact emission from the
disk (Fig.2.6; mid panels), which in this case is spatially unresolved and only
shows emission for the blueshifted velocities, between 0.8 and 2 km s^{-1}. The
spatial distribution, although unresolved, is consistent with the dust disk in
green contours. There is no emission > rms for C^{18}O (Fig.2.6; right panels).

[GY92] 197

Previously studied under different names (LFAM 26 and DCE 182), [GY92]
197 presents bipolar outflows observed in the H$_2$ lines (K$_s$ band; Hsieh, Lai,
and Belloche (2017)) and ^{12}CO (3-2) (sub-mm; Bussmann et al. (2007), van der
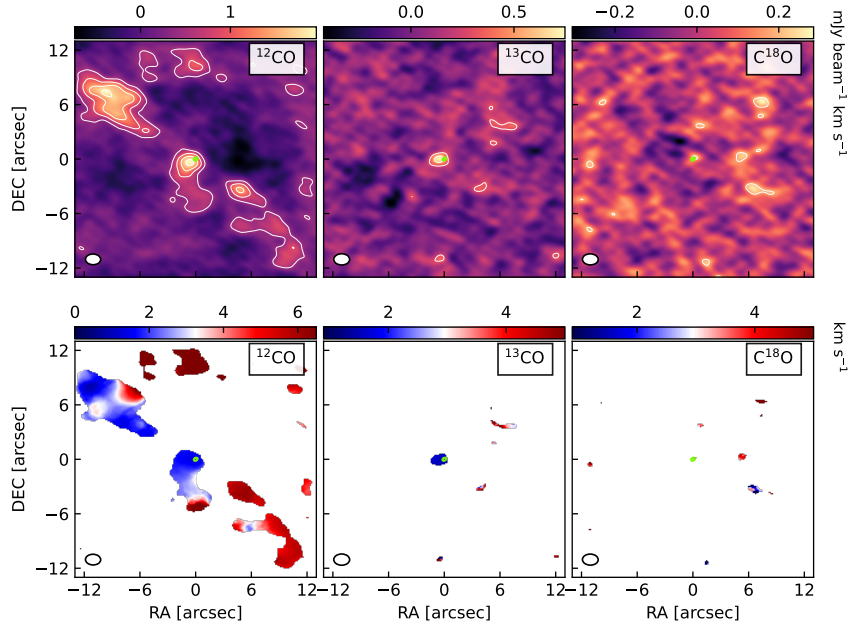
FIGURE 2.6: Maps of moments for CRBR 2317.5-1729, analogous to Fig. 3.4

Marel et al. (2013)). The measured geometric properties for these outflows are: an opening angle of 70º, an inclination of 5º, and an extent of >7.5" (1000 au) (Hsieh, Lai, and Belloche, 2017). In addition to kinematic properties, with velocities ranging from -0.7 to 1 km s^{-1} for the blueshift, and 6.7 to 11.5 km s^{-1} for the redshift emission (van der Marel et al., 2013).

Unlike previous observations, in this case, no extended emission similar to the previously mentioned bipolar outflows is observed (Fig.2.7). This may be due to self-absorption of the cloud around the central source at most velocities with line emission (Fig.2.22). Additionally, contamination of the cloud and/or diffuse emission from the outflows can be observed in the ^{12}CO line, as an emission column, between 5.8 and 8.4 km s^{-1}, vertically traversing (from north to south) the field of view, at a distance of 6" east of the central source (Fig.2.7; left panels). Furthermore, a pseudo streamer of material can be observed, interacting from the west with the source, between 6.4 and 8.4 km s^{-1}, but it coincides with the position of the outflow present in the literature, hence it may be a combination of cloud contamination with outflowing

material from the proto BD. Unlike the large-scale structure, emission related to the rotating gas disk around the central source can be observed (Fig.2.7; left-bottom panel). The disk has a geometry of 1.5"×1.2" (210 au × 168 au) and a position angle of 170º. The rotation and inclination of the disk are consistent with what is expected given the spatial position of the outflows (they are perpendicular), nevertheless, a discrepancy is observed between the emission of the continuum flux and the central azimuthal position of the rotating gaseous disk, with the dust disk situated in the blueshifted sector of the rotating gas. The velocity range for the disk is from -1 to 2.7 km s^{-1} in the blueshift, and from 6.5 to 7.9 km s^{-1} in the redshift (Fig.2.22).

In the case of emission in the ^{13}CO line, compact emission from the disk is observed, with possible rotation between 1 and 2.7 km s^{-1} (Fig.2.7; middle-bottom panel), but cloud absorption and possible contamination cause the absence of ^{13}CO detection for velocities beyond 4 km s^{-1}. The geometry of the disk for this line is... (Fig.2.7; middle-top panel). The dimensions and kinematics for the ^{13}CO disk are consistent with what is observed in ^{12}CO, with rotation centered on the continuum emission. In the case of C^{18}O, no emission >3×rms is detected.

[GY92] 344

The case of [GY92] 344 is distinctive within this sample due to its exclusive ^{12}CO line emission without any concurrent continuum emission. Morphologically, the observed gas structure manifests as central emission linked to the central source (Fig.2.8; left panels), accompanied by two bright, collinear knots situated at approximately 5" (700 au) from [GY92] 344. The extended emission across the field of view ranges from 0.8 to 2.2 km s^{-1} in the redshift and from 5 to 6.8 km s^{-1} in the blueshift. At 6.1 km s^{-1} (Fig.2.23), there is discernible evidence of what could correspond to the inner segment
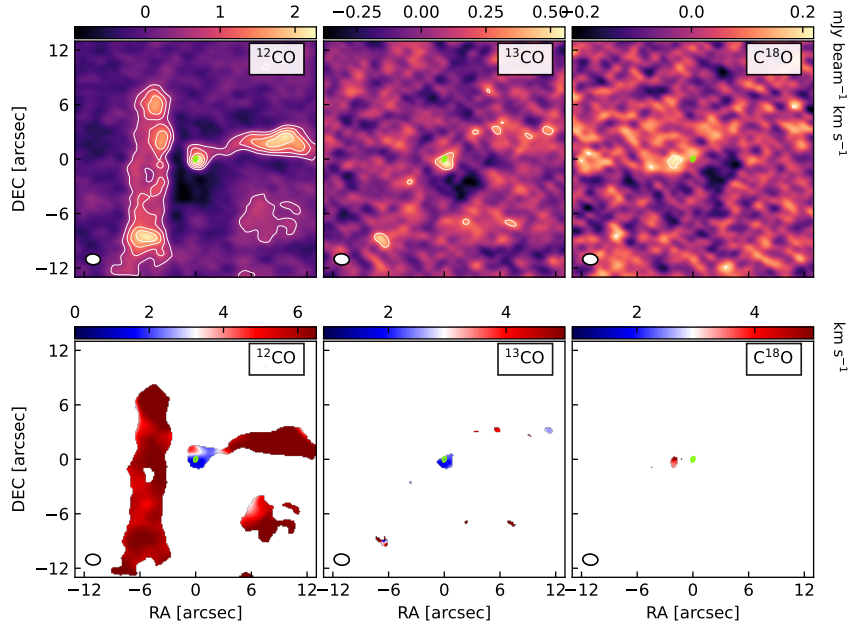
FIGURE 2.7: Maps of moments for [GY92] 197, analogous to Fig. 3.4

of bipolar outflows, emanating towards the northwest and southeast, respectively. Given the intricacies of the structure and potential cloud contamination effects (e.g., fig.2.23, channels 5.7 to 6 km s^{-1}), it remains impractical to determine geometric parameters for the extended emission. The measured dimensions for the central emission are 2.28"×0.8" (320 au × 112 au) with a position angle (PA) of 148°.

Previous near-infrared studies, focusing on the H$_2$ line emission for [GY92] 344 (or BKLT J162745-244454), have documented similar knots as depicted in fig.2.8, alongside bipolar outflows originating from this proto-brown candidate (Khanzadyan et al., 2004; Zhang et al., 2013). Furthermore, it is hypothesized that an edge-on continuum disk serves as the source of the aforementioned bipolar outflows, interacting with the envelope and thus leading to the emission of the knots. The current ^{12}CO observations serve to corroborate and support these proposed hypotheses.
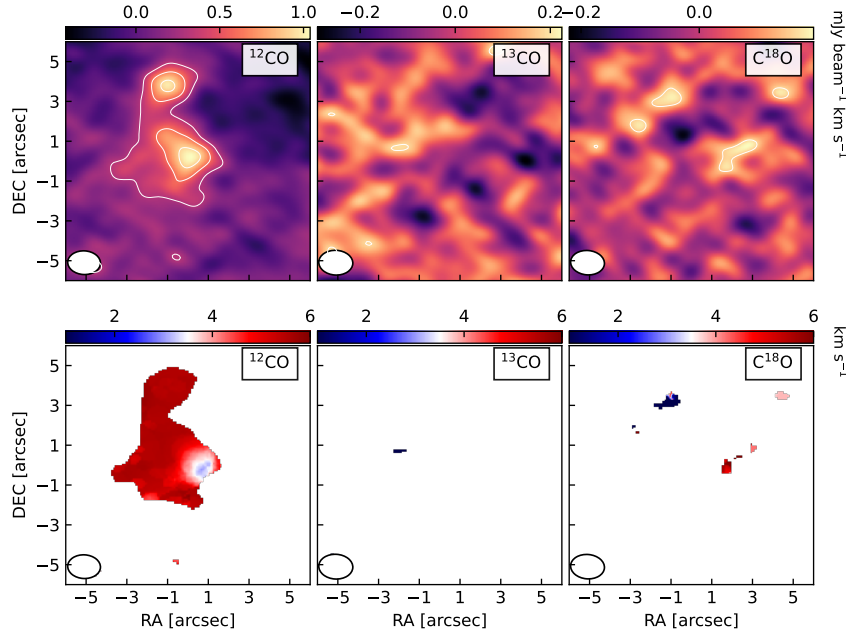
FIGURE 2.8: Maps of moments for [GY92] 344, analogous to
Fig. 3.4

2MASS J16274825-2442256

The source displays a faint continuum emission, approaching the detection threshold. Analogous to the dust content, gas lines such as ^{13}CO and C^{18}O, which are optically thin, elude detection within the sensitivity parameters of our observations. This suggests either highly concentrated emission of these lines at the disk center or a minimal gas mass surrounding the central source.

Nevertheless, despite the absence of the aforementioned lines, conspicuous and spatially extensive structure is discerned in the ^{12}CO line emission. Notably, in fig.2.9 (left panels), this emission exhibits a morphology reminiscent of an outflow, extending predominantly in an eastern direction from the source 2MASS J16274825-2442256. The observed structure spans a length of 15" (2100 au) with a projected thickness of 7" (980 au) on the plane of the sky. This configuration bears resemblance to structures previously documented in CRBR 2317.5-1729; however, a distinguishing feature is the utilization of a shared spatial domain in the celestial plane for both blueshift and redshift velocity regimes (Fig.2.24), suggestive of a monopolar outflow scenario. The
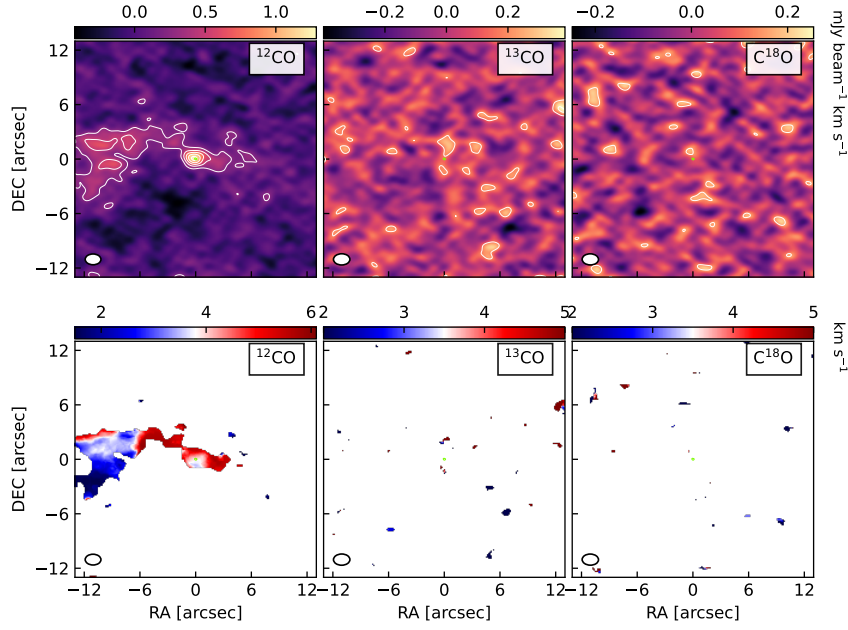
FIGURE 2.9: Maps of moments for 2MASS J16274825-2442256, analogous to Fig. 3.4

velocity span for the blueshifted emission ranges from 0.8 to 2.9 km s^{-1}, while for the redshifted component, it spans from 5.3 to 6.4 km s^{-1}.

Central to the field of view and aligned with the continuum emission, a more compact structure indicative of a protoplanetary disk is observed. Rotational velocities within this disk range from 1.1 to 2.7 km s^{-1} for the blueshifted component and from 5.1 to 6.2 km s^{-1} for the redshifted counterpart. Noteworthy is the presence of cloud absorption surrounding the disk, contributing to the non-detection of emissions around the systemic velocity. Measurements of the gas disk yield dimensions of 2.18" × 1.04" (equivalent to 305 au × 146 au) with a position angle of 73°. The continuum emission from the disk is centrally located between the redshifted and blueshifted gas emissions (Fig.2.9; left-bottom panel), further supporting the assertion that compact gas emissions associated with the central source are indeed attributable to the protoplanetary disk.

BKLT J162858-244054

Similar to other sources discussed earlier, BKLT J162858-244054 exhibits an absence of detectable emission in the ^{13}CO and C^{18}O lines above the noise threshold (>1× rms) associated with the central source.

Regarding the ^{12}CO emission, analysis of fig.2.10 (left panels) reveals central emission patterns consistent with those expected from the disk, aligning well with the position of continuum detection. Notably, unlike the majority of sources in our study, the ^{12}CO emission manifests solely within specific velocity channels, notably between 1.8 and 3 km s^{-1}, corresponding to the anticipated blueshifted component. Within the velocity range of 2.5 to 3 km s^{-1} (Fig.2.25), discernible signals suggestive of bipolar outflows emerge, emanating from the central source towards both the southern and northern directions. However, it's noteworthy that these velocity channels also coincide with the velocities associated with the Ophiuchus cloud, raising the possibility of this emission being a result of transposition from the cloud. Moreover, significant self-absorption is observed around the disk emission, particularly evident at velocities around 2.4 km s^{-1}, complicating the determination of the nature of the subsequently observed extended emission.

Geometric analysis of the central emission, attributed to the gas disk, yields dimensions of 1.06" × 2.05" (148 au × 287 au) with a PA of 28º.

In addition to its candidacy as a proto-brown dwarf, BKLT J162858-244054 is also identified as a potential "ExOr candidate" due to its propensity for eruptive events, as classified by Antoniucci et al., 2014. ExOr objects are characterized by periodic enhancements in their optical luminosity (Herbig, 1989). While ExOr sources typically exhibit only rotating disks around the central protostar, some instances may feature extended structures such as outflows or spiral arms (e.g., Hales et al., 2020, Huang et al., 2023). Despite the ambiguity surrounding the nature of the extended emission in BKLT
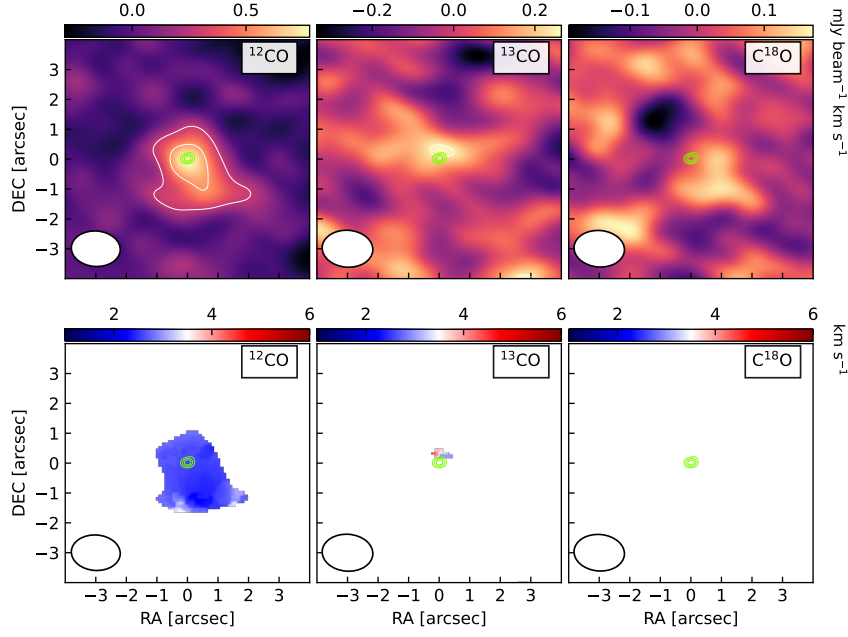
FIGURE 2.10: Maps of moments for BKLT J162858-244054, analogous to Fig. 3.4

J162858-244054, its designation as an ExOr candidate suggests the possibility of extended disk or bipolar outflow structures, as evidenced in fig.2.9.

2MASS J16313383-2404466

This source exhibits several discernible extended gas structures. In the moment 0 map of ^{12}CO presented in fig.2.11 (left panels), the base of bipolar outflows is evident, extending up to 3.1" (434 au) from the central source to their outermost regions, characterized by an opening angle of 113°. The corresponding moment 1 map delineates the velocity range for both the blueshift and redshift components of the outflows, spanning from -0.2 to 1.9 km s^{-1} and from 2.9 to 4.6 km s^{-1}, respectively. Notably, the center of the continuum emission coincides spatially with both the emission peak of the ^{12}CO line and the centers of the outflows, all converging at the systemic velocity (2.5 km s^{-1}).

In addition to the outflows depicted in the moment maps, intriguing features are observed within the velocity range of 1.4 to 1.8 km s^{-1}, including
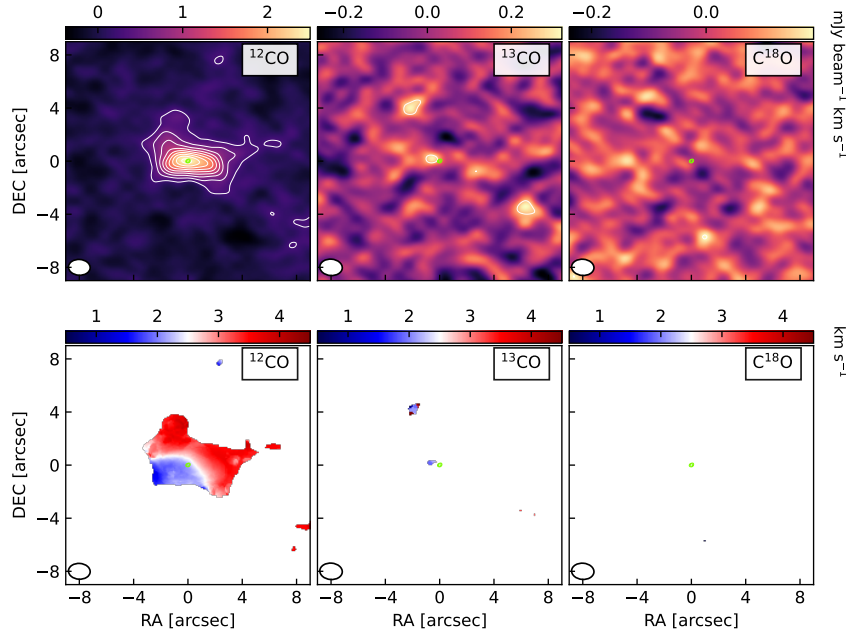
FIGURE 2.11: Maps of moments for 2MASS J16313383-2404466, analogous to Fig. 3.4

a column of emission extending from the disk towards the northern region of the field of view (Fig.2.26). This emission could potentially represent an accretion streamer, the inner segment of the extended outflow, or cloud contamination. However, conclusive determination of its nature is impeded by the observational depth and the presence of self-absorption along the eastern and western edges of the emission column. Subsequent channels, spanning from 3.2 to 3.8 km s^{-1}, reveal another noteworthy large-scale gas structure emerging westward from the central disk. This structure likely corresponds to the western segment of the north and south outflows, particularly at their slower blueshift velocities. Nonetheless, due to limitations in sensitivity, the observations fail to detect outflow emissions associated with velocities farther from the systemic velocity of 2MASS J16313383-2404466.

Furthermore, the depth of our observations precludes significant detection (> 3× rms) of the ^{13}CO and C^{18}O lines, with only sporadic emissions observed, likely attributable to noise within the field of view (Fig.2.11; middle and right panels).

2MASS J16313679-2404200

In the investigation of outflows surrounding proto-brown dwarfs, Riaz and Bally, 2021 utilized images obtained from the VLT/SINFONI instrument to study 2MASS J16313679-2404200, revealing the presence of outflows in the H_2 (2.12 μm) and [FeII] (1.257 μm) lines. These outflows exhibit extended emission, spanning approximately 6" (840 au), oriented diagonally from southeast to northwest across the field of view, intersecting the central source.

Our observations confirm and support the findings of Riaz and Bally, 2021 regarding the existence of prominent outflows in 2MASS J16313679-2404200. Fig.2.12 illustrates the bipolar outflows observed in the ^{12}CO line, extending throughout the entire field of view, with a measured extent exceeding 35" (4900 au). Notably, the opening angles of these outflows are smaller compared to those observed in the other sources of this sample, measuring 40° for the northern component and 30° for the southern component, suggesting an early evolutionary stage for this source (Arce and Sargent, 2006). Unlike typical outflows, 2MASS J16313679-2404200 exhibits both blueshifted and redshifted components, with velocity ranges spanning from -2 to 1.9 km s^{-1} and from 3 to 6.2 km s^{-1}, respectively (Fig. 2.27). Across all channels displaying 12CO emission, the northern outflow appears approximately 2.7 times brighter than its southern counterpart, resulting in a wider velocity range of detection for the former, ranging from -2 to 6.2 km s^{-1} for the northern outflow and from 0.3 to 5.4 km s^{-1} for the southern one. The inclination of the continuum disk aligns well with the spatial distribution of the outflows, centered at the base of these structures.

Furthermore, a central bulge surrounding the source is discernible in the ^{12}CO emission, likely associated with the circumstellar disk, also detected in the ^{13}CO line (Fig.2.12; middle panels). The dimensions of the gas material
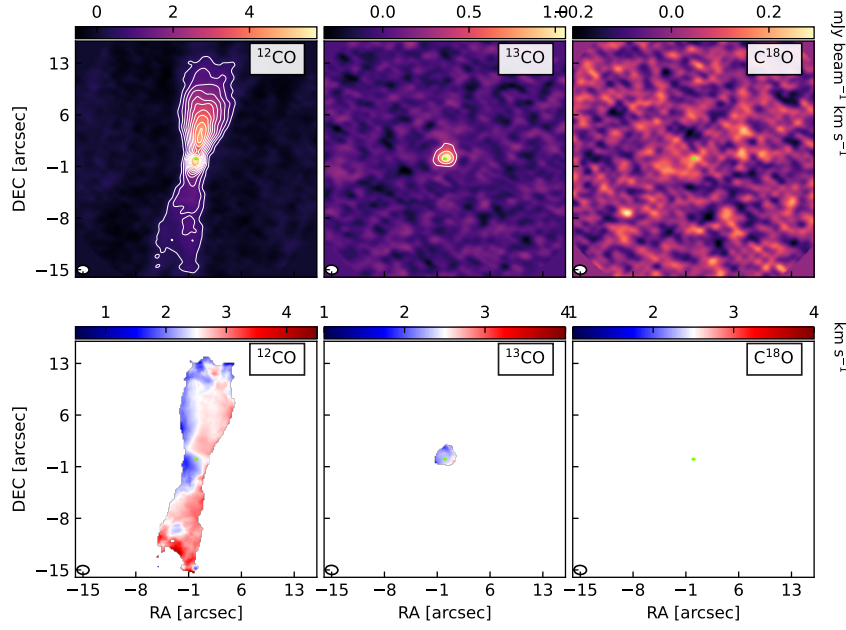
FIGURE 2.12: Maps of moments for 2MASS J16313679-2404200, analogous to Fig. 3.4

associated with the disk measure 1.4" × 2.2" (200 au × 300 au), with a position angle of 149°. Rotational features of the disk detected in ^{13}CO range from 1.2 to 2.1 km s^{-1} for blueshifted velocities and from 2.9 to 3.6 km s^{-1} for redshifted velocities. However, rotational signatures are not entirely distinct in the velocity map due to overlapping spatial areas of blueshifted and redshifted emissions.

Despite the pronounced outflow emission in ^{12}CO and the detected disk in ^{13}CO, no detectable emission is observed for C^{18}O above the noise level in these observations (Fig.2.12; right panels).

ISO-Oph 200

Utilizing the same dataset presented in this study, Riaz and Machida, 2021 conducted an exhaustive investigation of the outflow phenomena associated with the proto-brown dwarf candidate ISO-Oph 200. For completeness and comparative analysis, we have included our versions of the integrated flux

and velocity maps for this source (Fig.2.13), accompanied by a concise description of the observed spectral lines.

In the ^{12}CO emission line (Fig.2.13; left panels), a well-defined bipolar outflow structure is evident, extending over > 16" (2240 au) with an approximate symmetric opening angle of 65° for both outflow lobes. Velocity measurements for the blueshifted component range from -3.5 to 5.2 km s^{-1}, while for the redshifted component, they span from 5.3 to 10.5 km s^{-1}. Notably, the spatial origin of the outflows coincides with the location of continuum emission. Supplementary analysis in Figure A10 reveals combined emission from both outflows in select velocity channels, alongside potential edge contamination effects attributed to cloud interference.

In the case of ^{13}CO emission, our observations reveal a central flux pattern indicative of an extended, rotating gas disk surrounding ISO-Oph 200, orthogonal to the kinematic axis of the outflows, with continuum emission centered between blueshifted and redshifted components (Fig.2.13; middle panels). Additionally, discernible extended emission is observed in the redshifted direction, likely associated with inner wall cavities as elucidated by Riaz and Machida, 2021.

Furthermore, the presence of the gas disk associated with ISO-Oph 200 is corroborated by observations in the C^{18}O line (Fig.2.13; right panels). Analysis of the moment 0 map highlights a disparity in brightness between the northeastern and southwestern regions, indicative of potential spatial displacement between gas and dust disk emission. However, precise quantification of this displacement remains elusive with the current dataset. Unlike other observed lines, C^{18}O exhibits a narrower velocity range, spanning from 3.6 to 4.4 km s^{-1} for the blueshift and from 4.7 to 5.7 km s^{-1} for the redshift. Tentative estimations of the disk dimensions for C^{18}O yield dimensions of approximately 3.5" × 7.5" (490 au × 1050 au) with a position angle of 31°.
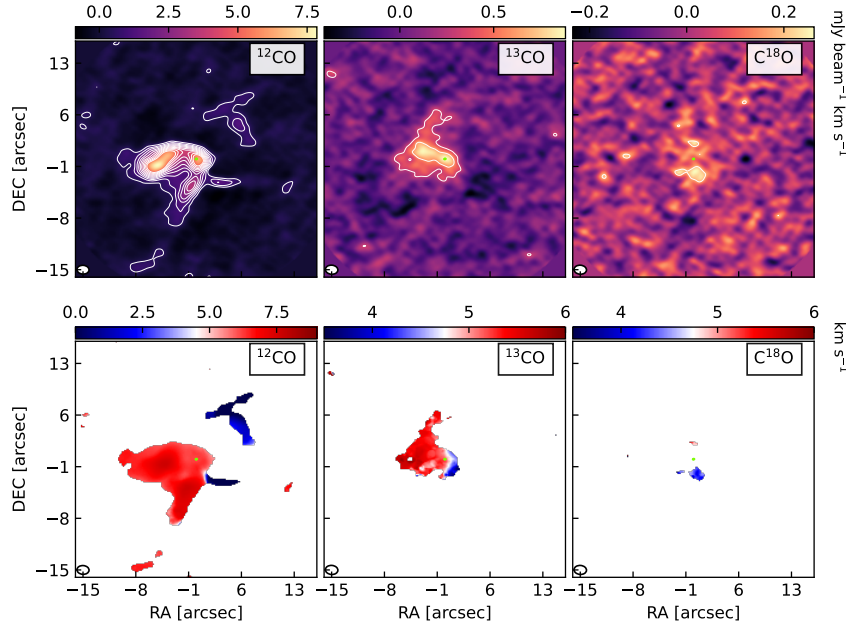
FIGURE 2.13: Maps of moments for ISO-Oph 200, analogous to
Fig. 3.4

ISO-Oph 204

In the binary system ISO-Oph 204, we observe conspicuous gas emission
distributed across the entire field of view, yet devoid of any discernible ex-
tended structures directly associated with either the central source (hereafter
referred to as ISO-Oph 204, or the primary) or the wide binary source (GBS-
VLA J163151.93-245617.4, or the secondary).

In the ^{12}CO spectral line, a prominent large-scale arched structure man-
ifests to the northwest of the binary system (see fig.2.14; left panels), span-
ning nearly half of the observational field. Redshifted line emissions range
between -1.4 and 2.2 km s^{-1}, while blueshifted emissions span 4.6 to 6.8
km s^{-1}. Notably, a blueshifted detection (Fig.2.29) exhibits a morphology
reminiscent of outflow emanating from the primary source, towards the north-
west of the celestial plane. However, emissions within the velocity range of
0.9 to 1.5 km s^{-1} coincide with expectations for possible cloud contamina-
tion, blurring the distinction between emissions directly attributable to the
system and those from the surrounding cloud. Redshifted emissions largely

correspond to the structure depicted in the moment maps (Fig.2.14; left panels). Similar to blueshifted emissions, redshifted emissions likely include a substantial component associated with cloud brightness, as indicated by negative values, indicative of cloud self-absorption, around the primary source position and in proximity to the secondary component. Additionally, compact brightness associated with the primary source, observed between velocities of 4.6 and 5.6 $km\,s^{-1}$, may correspond to blueshifted emission from the protoplanetary disk surrounding ISO-Oph 204.

In the case of ^{13}CO, we observe an extended structure closely resembling that seen in ^{12}CO (Fig. 2.14; middle panels). Line detections for ^{13}CO predominantly occur within the velocity range of 1.7 to 5.6 $km\,s^{-1}$, with emissions primarily aligning with expected velocities for potential cloud contamination (Fig. 2.14; middle-bottom panel), suggesting that much of the observed large-scale structure likely arises from contamination unrelated to the binary system. Unlike observations in ^{12}CO, ^{13}CO exhibits a spatially broader flow associated with the disk surrounding the primary source. Specifically, the velocity range for disk emission spans between 2.1 and 3.2 $km\,s^{-1}$ for blueshifted emissions and between 4.2 and 5.2 $km\,s^{-1}$ for redshifted emissions. The geometric parameters of the disk measure 1.6"×1.1" (224 au × 154 au), with a position angle of 73°. Similar to observations in ^{13}CO, cloud self-absorption is evident at the same position as continuum emission from the secondary source (Fig.2.14; middle-top panel).

Regarding $C^{18}O$, we observe structures akin to those discussed previously. Emission for this molecular line is concentrated predominantly between velocities of 2.9 and 4.1 $km\,s^{-1}$ (Fig.2.14; right panels), with a morphology reminiscent of a spiral or streamer of material flowing towards the primary component of the system. However, given the high likelihood of contamination from the surrounding cloud, we refrain from speculating on
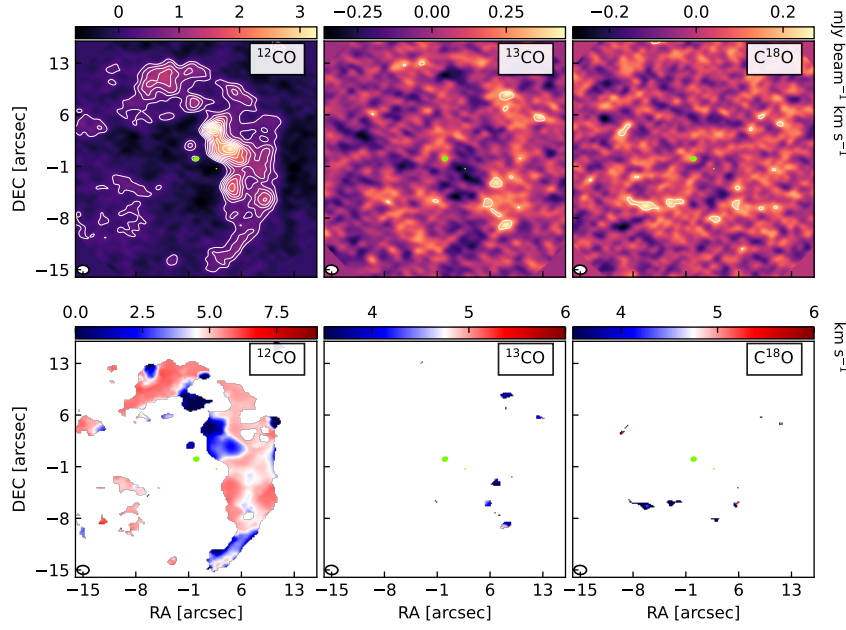
FIGURE 2.14: Maps of moments for ISO-Oph 204, analogous to
Fig. 3.4

specific interpretations. Consistent with earlier observations, emission related to the disk around ISO-Oph 204 is evident, albeit confined to a few channels centered around 4 km s^{-1}. The emission from the C^{18}O disk is sufficiently compact as to preclude measurement of geometric parameters using imfit.

WLY 2-69

The second binary system under investigation in this study comprises the sources WLY 2-69 (hereafter referred to as the primary) and 2MASS J16322081-2430290 (the secondary). This binary system exhibits a complex array of gas structures, which may be indicative of various physical phenomena including potential outflows, rotating disks, and/or material bridges between the two sources.

Fig.2.15 illustrates the gas emission between these sources across all observed molecular lines. In the case of ^{12}CO (Fig.2.15; left panels), the emission morphology aligns with that expected for bipolar outflows emanating
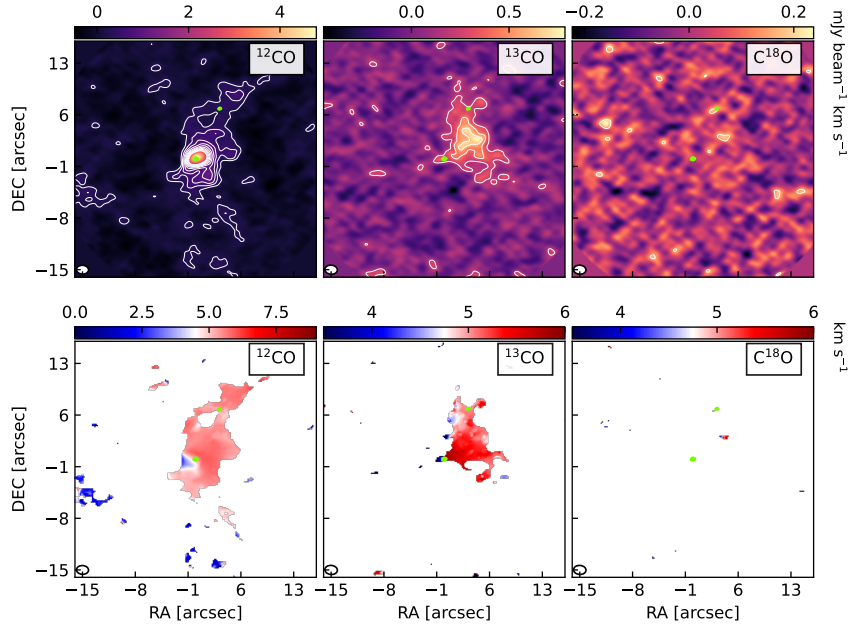
FIGURE 2.15: Maps of moments for WLY 2-69, analogous to Fig. 3.4

westward from the central source (primary), coinciding spatially with the position of the secondary source. Blueshifted emission is detected within velocities ranging from 1.1 to 3.1 km s^{-1}, while redshifted emission spans velocities from 4.8 to 7.8 km s^{-1}. Analysis of emission channels (Fig.2.30) reveals various interpretations for the observed structures in fig.2.15. Notably, weak detection of a potential southeastward outflow from the primary source is observed at blueshift velocities between 1.5 and 2.2 km s^{-1}, exhibiting an extension >17" (2380 au) and an estimated opening angle of 119°. Conversely, redshift detection suggests an outflow oriented entirely westward from the central source, thus deviating from the spatial symmetry observed in the blueshifted component. Further investigation reveals weaker emission northeast of the source at a velocity of 5.6 km s^{-1}, aligning with the spatial distribution of the blueshift component and its estimated opening angle. Hence, we propose that the outflow material may be influenced by the presence of the secondary source, resulting in an eastward outflow from the primary source, similar to recently reported by Ohashi et al., 2022, with an

extension >17" (2380 au) and an opening angle of 89º. Potential interactions or previous flybys between the sources cannot be dismissed, potentially leading to the observed gas bridge between them (e.g. Cuello et al., 2020; Cheng et al., 2022). Additionally, a bright and rotating accumulation associated with continuum emission from the primary source is observed, likely representing part of the protoplanetary disk surrounding the proto-brown dwarf candidate, in conjunction with the basal part of the outflows. This central bright region associated with the disk measures 2.5" × 1.9" (350 au × 266 au) with a PA of 129º.

In the ^{13}CO line, a structure akin to that observed in ^{12}CO (Fig.2.15; middle panels) is noted, with an emission peak associated with the primary source, indicative of rotation and consistent with the presence of a dust disk. Notably, the orientation of the outflow detected in the redshift differs from that observed in ^{12}CO, suggesting potential deformation influenced by the secondary component. Blueshifted emission for ^{13}CO is observed within velocities ranging from 2.9 to 3.5 km s^{-1}, with redshifted emission spanning velocities from 4.8 to 6.3 km s^{-1}.

Finally, for $C^{18}O$ (Fig.2.15; right panels), gas patches are exclusively detected within the bridge region between both sources, with emission concentrated between velocities of 4.4 and 5.7 km s^{-1}.

2.6 Discussions

2.6.1 Gas and dust masses

As discussed previously in section 4.2, initial estimates of gas masses relied on simplistic yet widely-used approximations to gauge the gas content based on continuum emissions. However, for sources where ^{13}CO and $C^{18}O$ were

detected, application of models proposed by Williams and Best, 2014 provided more refined estimates. Specifically, for BKLT J162546-242337, a gas mass of 3.7 ± 0.4 M_{Jup} (with a gas-to-dust mass ratio of 65) was obtained, while for CRBR 2315.8-1700, a gas mass of 13.6 ± 2 M_{Jup} (with a gas-to-dust mass ratio of 92) was derived. These ratios, alongside the limited validation from only two sources, suggest that the ratio used for the remaining sources ($M_{gas}/M_{dust} = 100$) serves as a reasonable approximation or, at most, represents an upper limit for gas mass in the disk.

In the case of ISO-Oph 200, emissions were detected across all spectral lines. However, differentiating emissions originating from outflows and stellar winds from those arising from the protoplanetary disk itself (as illustrated in Fig. 2.13) proved to be challenging. Consequently, flux measurements for ^{13}CO and $C^{18}O$ lines did not permit the application of the aforementioned models to estimate gas mass accurately. Nonetheless, Riaz and Machida, 2021 provided an estimate for the total disk mass ($M_{gas} + M_{dust}$) of ISO-Oph 200, ranging between 4 and 7 M_{Jup}.

For the remaining sources, disk masses ranged from 0.08 to 14.3 M_{Jup}, while the upper mass limit for brown dwarfs (BDs) stands at around 80 M_{Jup}. Therefore, the observed mass of proto-brown dwarf candidates in this study should not exceed 65 M_{Jup}, assuming complete accretion, in order to remain within the substellar regime throughout their evolutionary lifespan. It is anticipated that a portion of this material will eventually be photo-evaporated or accreted by planets forming within the protoplanetary disk (refs). However, for this sample of Class I and FS sources, continual accretion of material from the envelope is expected (refs), implying that the amount of gas and dust in later stages of evolution should exceed that described in this study. Nevertheless, the anticipated margins for proto-BD mass growth should remain consistent with those previously discussed.

2.1 provides a summary of stellar mass estimations from existing litera-
ture (refs), with estimations available for only five sources. Among these,
CRBR 2317.5-1729 has already surpassed the mass threshold for the substel-
lar regime, presenting the highest disk mass (14.3 M_{Jup}), thereby extend-
ing the margin for the remainder of the sources to approximately 70 M_{Jup}
to complete their evolutionary transition into BDs. Another source exceed-
ing the theoretical mass limit for the substellar regime is BBRCG 58, which
neither exhibits continuum nor line emissions; nonetheless, inclusion in this
sample is justified based on its M6 spectral type. Both of these sources can
be classified as very low-mass stars (VLMS, refs). Furthermore, [RR90] Oph
2320.8-1721 is estimated to have a mass of 39 M_{Jup}, without exhibiting any
continuum or line emissions, marking it as the first source confirmed as a
proto-BD in this study. Following suit, [GY92] 154 has a mass of 67 M_{Jup},
with weak continuum detections and no line emission, suggesting an esti-
mated disk mass of < 1 M_{Jup} and designating it as the second proto-BD
confirmed in this investigation. Lastly, source [GY92] 344, with a mass of 35
M_{Jup} and no continuum emission, exhibits ^{12}CO detection as described in
section 4.2.5. Given its low mass and marginal disk material, this source is
identified as the third confirmed proto-BD in this study.

All sources examined in Section 2.5.2 display line emission associated
with their disks, alongside extended emission of potentially diverse physical
origins. Figure 16 depicts the relationship between disk mass, inferred from
continuum flux, and the flux of ^{12}CO (2-1) emission, distinguishing between
Class I and FS sources. Interestingly, there is no discernible difference in the
gas detection rates between these classes, nor is there a significant distinc-
tion in the distributions of disk mass and extended gas emission. However,
a linear correlation between dust mass and gas flux is evident, suggesting a
potential evolutionary link between Classes I and FS, distinct from Class II
sources.
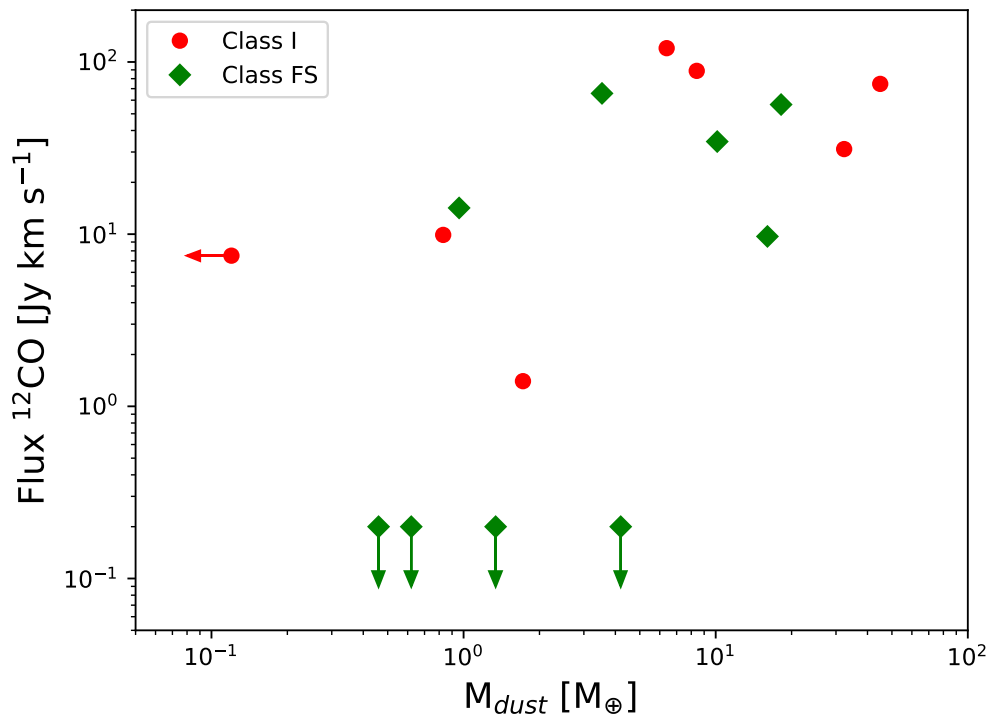
FIGURE 2.16: Plot of disk mass versus flux of ^{12}CO (2-1) line for sources with continuum and/or molecular line detections presented in this study. The plot points are categorized by class, with Class I (red circles) and Class FS (green diamonds) objects. Sources indicated by arrows represent upper limits for the respective axis of the arrow.

Nevertheless, the current sample size does not permit a robust demonstration of this correlation. To elucidate further, observations with increased sensitivity are imperative to detect and accurately measure flux values, particularly for proto-BD candidates lacking of faint (< 1 $M_\oplus$ and/or Jy km s^{-1})detections in these observations (some of which are indicated as upper limits in Figure 2.16). Such data would help to address the absence of detections below certain thresholds, enhancing our understanding of the spatial scales inherent to different proto-BDs relative to classical T-Tauri Stars (CTTSs).

2.6.2 Possible planet formation

The presence of exoplanets orbiting brown dwarfs has been well-established in scientific literature spanning several decades (Chauvin et al., 2005). These exoplanets exhibit a mass spectrum up to 7.5 M_{Jup}, with orbital distances extending up to 15 au from their respective host brown dwarfs (Bowler and Hillenbrand, 2015).

Within our surveyed sample of proto-brown dwarf candidates, a notable 76% of the sources display continuum emission (Fig. 3.2). The dust mass within these sources ranges from 0.24 to $\sim$ 50 $M_\oplus$ (Table 2.3), presenting conditions conducive to the formation of terrestrial planets, and for more massive disks, giant planets. Despite the youthfulness of these sources, discernible substructures within their disks are notably absent. This observation could be attributed to the early evolutionary stage of the disks, suggesting the possible absence of giant planets, or it may be a result of inherent limitations in angular resolution. Notably, prior studies employing ultra-high angular resolution techniques on Class 0-I disks similarly failed to detect substructures (e.g., Ohashi et al., 2023), supporting the former hypothesis.

High-angular resolution observations, particularly of Class II sources within

the substellar regime, have revealed substructures such as cavities (Pinilla, 2022), indicative of ongoing planetary formation within disks of similar masses observed in our study. Thus, the proto-brown dwarf candidates investigated in this study are well-endowed with the requisite material for planet formation, including giants in select cases, during subsequent evolutionary phases. Furthermore, it remains plausible that these disks may already harbor protoplanetary cores, albeit not yet sufficiently massive (> 10 $M_{\oplus}$) to generate detectable substructures (Rosotti et al., 2016).

González-Ruilova et al., 2020 recently published findings on the wide binary system ISO-Oph 2, where the secondary component, identified as a proto-brown dwarf, possesses a transition disk with a dust mass of ~ 0.8 $M_{\oplus}$ for the continuum and a diameter extending to ~ 3.5 au. This source, categorized as a Class II object, serves as a potential evolutionary analog for the younger proto-brown dwarf candidates and their associated protoplanetary disks presented in our study. Notably, observations of this source, conducted as part of the ODISEA project, also failed to detect substructures at the angular resolution employed in our study, emphasizing the necessity for higher angular resolution, and sensitivity, observations ($> 0.05''$) to definitively elucidate the state of planetary formation within the disks in this research.

2.6.3 Statistics between Class I, FS and II sources

In accordance with the selection criteria outlined in Section 2, the identification of proto-BD candidates in this study follows the methodology established by Testi et al., 2016, wherein all Class II sources in the Ophiuchus region with a spectral type M6 or later are considered. Our study now encompasses the observations of substellar Class I, flat spectrum (FS), and Class II sources, allowing for a comprehensive comparison of detection rates and disk mass distributions across infrared (IR) classes.

Figure 2.17 illustrates detection percentages for sources classified into different IR classes within the Ophiuchus region, sourced from Evans et al., 2009. Notably, Class II sources dominate the population, constituting 68.2% of the objects, followed by FS sources at 17.4%, and Class I sources at 14.4%. Upon integrating our proto-BD candidates with those identified by Testi et al., 2016, we observe a relative decrease in the percentage of Class II sources (44.7%) compared to the total young stellar objects (YSOs) within this star-forming region (SFR). This shift implies a relative increase in the proportions of Class I (23.7%) and FS (32.6%) sources. Such a trend prompts considerations regarding the evolutionary timescales and formation mechanisms of proto-BDs within the cloud environment.

Furthermore, Figure 2.18 presents the cumulative distribution of disk masses across different IR classes. Notably, Class II proto-BDs exhibit a more linear and continuous mass distribution compared to Classes I and FS. A notable disparity emerges between the mass distributions of low and high-mass disks for Classes I and FS, with approximately half of the disks possessing masses < 0.4 M_{Jup}, followed by a plateau extending to ∼1 M_{Jup}. This observation suggests potential differences in the formation mechanisms and evolutionary histories between Class II proto-BDs and those in earlier evolutionary stages. Importantly, to bolster sample sizes, upper limits of non-detections (6×10^{-2} M_{Jup}) are included as measurements, aligning with previous methodologies employed by Testi et al., 2016.

It's important to acknowledge that while our findings provide valuable insights into proto-BD populations within the Ophiuchus region, these samples may not be statistically significant for conducting rigorous distribution tests. Future investigations should aim to expand sample sizes by incorporating proto-BD candidates from diverse SFRs, assuming uniformity in disk mass distributions across various molecular cloud environments. Moreover, future deeper observations, particularly improving the sensitivity for dust
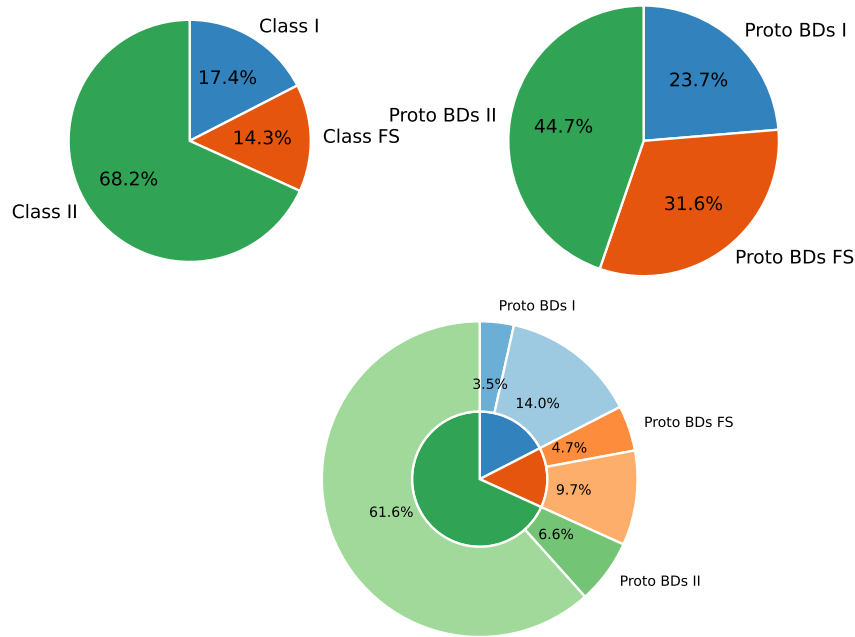
FIGURE 2.17: Pie charts illustrating the recurrence statistics of proto-BD candidates categorized by class (I, FS, and II), juxtaposed with the distribution of total YSOs in the Ophiuchus molecular region. Top-left chart: The percentages of YSOs classified by class according to the c2d program. Top-right chart: The percentages of proto-BD candidates delineated by class. Bottom chart: Combination of the data from the upper charts, with solid colors representing the total YSO distribution at the center, and the proportions of proto-BD candidates by class depicted with smoothed colors along the edges.
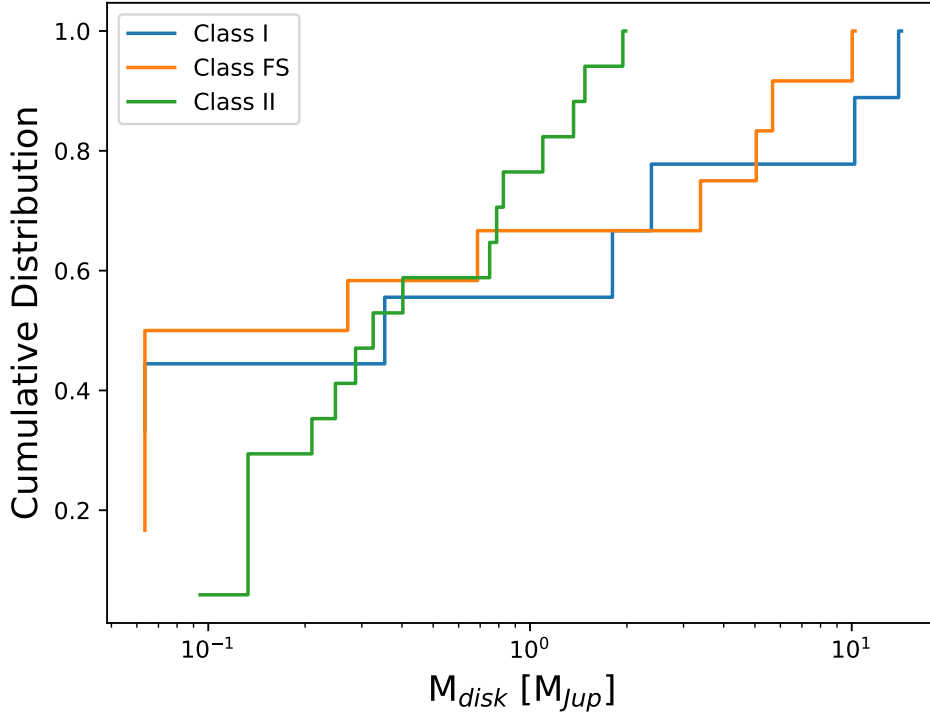
FIGURE 2.18: Empirical Cumulative Distribution Functions (ECDFs) illustrating disk masses in proto-BD candidates categorized by class (I, FS, and II) in the Ophiuchus region. The distribution for Class II proto-BDs is sourced from data presented by Testi et al. (2016).

and gas detections, hold promise for refining our understanding of mass distributions within less massive disks and further elucidating the mechanisms driving proto-BD formation and evolution.

2.7 Conclusions

In this work, we have presented observations of continuum and molecular line emissions for 21 proto-BD candidates in the Ophiuchus cloud, belonging to the ODISEA survey. In general, the main results for extended emission and protoplanetary disks are as follows:

1) We detected 16 sources in the continuum at 225 GHz, with fluxes ranging from 0.1 to 55 mJy, where only 2 could be spatially resolved at 0.3" angular

resolution.

2) The dust mass is sufficient to form planets in most of the detected disks, contradicting previous observations for more evolved Class II sources.

3) Nearly half of the sample, 10 sources, exhibit emission in at least one of the three molecular lines presented here (12CO, 13CO, and C18O). All these sources are associated with extended emissions >150 au, which in some cases correspond to mono and bipolar outflows, possible accretion streamers from the cloud, and more compact rotation disks.

4) The significant contamination of the cloud around the systemic velocity hinders the interpretation of the data for extended gas structures. Deeper observations are necessary to detect and analyze high-velocity emissions, away from cloud contamination.

5) Assuming that the statistics and observations, encompassing Classes I, FS, and II, are representative and cover almost all proto-BDs present in Ophiuchus, we can conclude that there is a higher prevalence of young sources, Class I and FS, compared to the statistical evolution of the rest of the sources in the cloud. The expected result, following the trend of more massive and brighter sources in Ophiuchus, would imply a much larger proportion of Class II proto-BDs than I and FS.

Whether to study planetary formation around proto-BDs or to elucidate the formation mechanisms of these sub-stellar objects, future sub-mm observations with higher angular resolution and sensitivity are necessary. In any case, these observations demonstrate the efficiency of the ALMA radio interferometer, considering that each observation requires <1 minute of integration per source, making it cost-effective to obtain observations that could be crucial for understanding these common sources in the Milky Way.

2.8 Data Availability

The data underlying this article are available in the ALMA archive: `https://almascience.eso.org/aq/`, with Project ID (PID) 2016.1.00545.S.

2.9 Extra Material

Here we present the channel maps, corresponding to the ^{12}CO data cubes of sources discussed in Section 2.5.2. White contours showed in each Figure represent the area of measured the integrated line flux, presented in Table 2.4. The gray plots in some of the figure represent the channels/velocities range where is not emission $\geq 3 \times$ rms. The contours do not consider the whole emission which reach the rms levels mentioned, due the cloud contamination in some cases, we constrained the area of flux emission to avoid, much as possible, the pollution unrelated with the central proto-BD candidates.
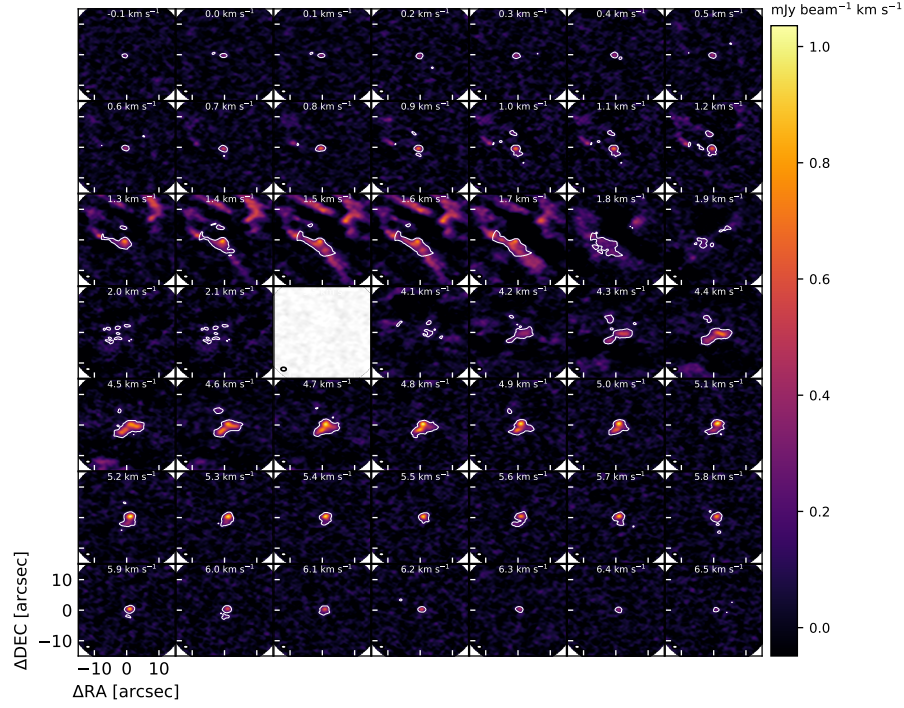
FIGURE 2.19: ^{12}CO channel maps for the source BKLT J162546-242337. White contours are the area, with emission intensity $\geq 3 \times$ rms, considered for the flux integration measurement. In left-bottom corner of each plot, it is the beam size shape in white. The ticks levels are the same in all the plots, the same as in left-bottom plot.
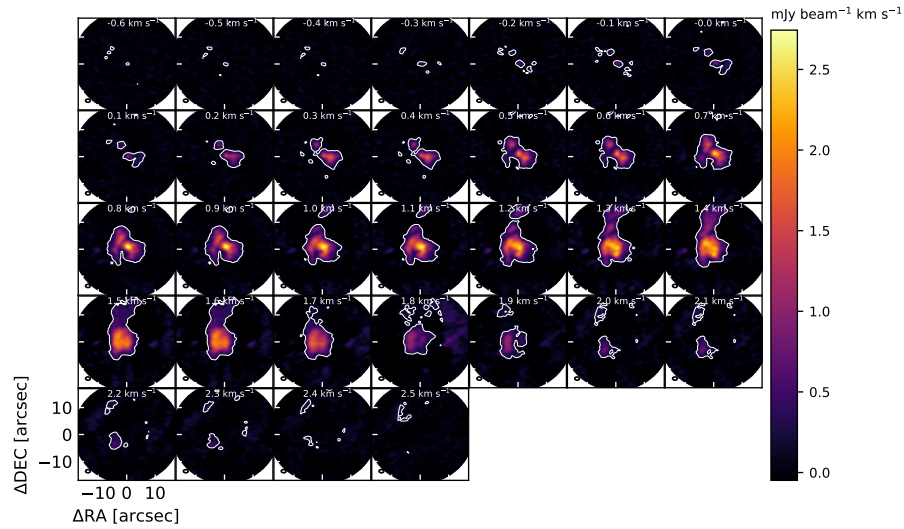
FIGURE 2.20: ^{12}CO channel maps for CRBR 2315.8-1700, analogous to Fig. 2.19
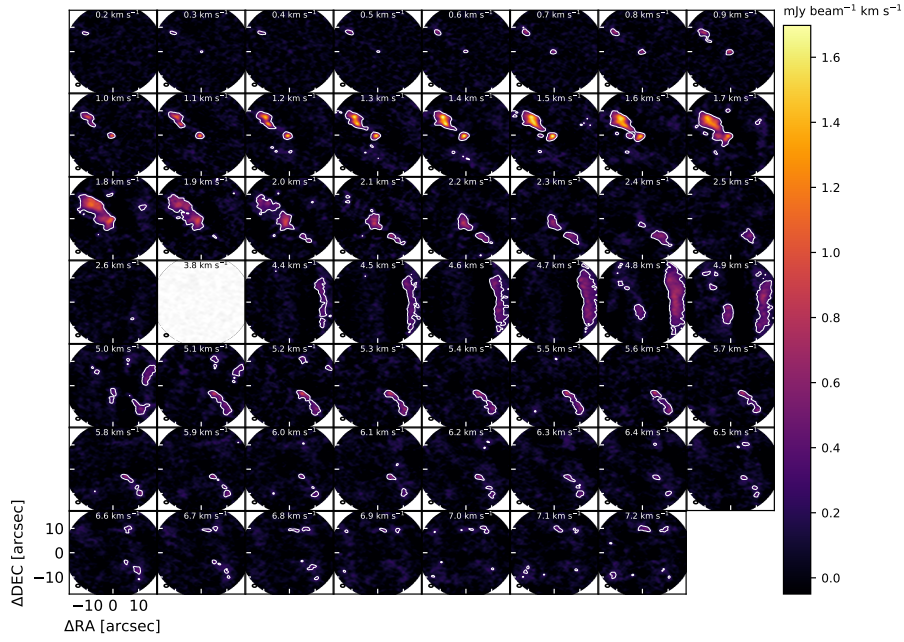
FIGURE 2.21: ^{12}CO channel maps for CRBR 2317.5-1729, analogous to Fig. 2.19
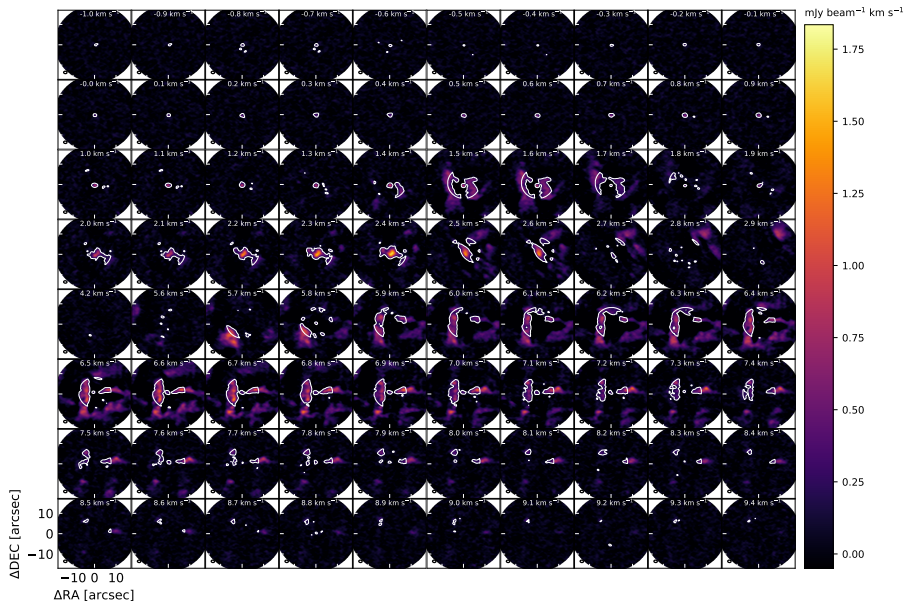
FIGURE 2.22: ^{12}CO channel maps for [GY92] 197, analogous to Fig. 2.19
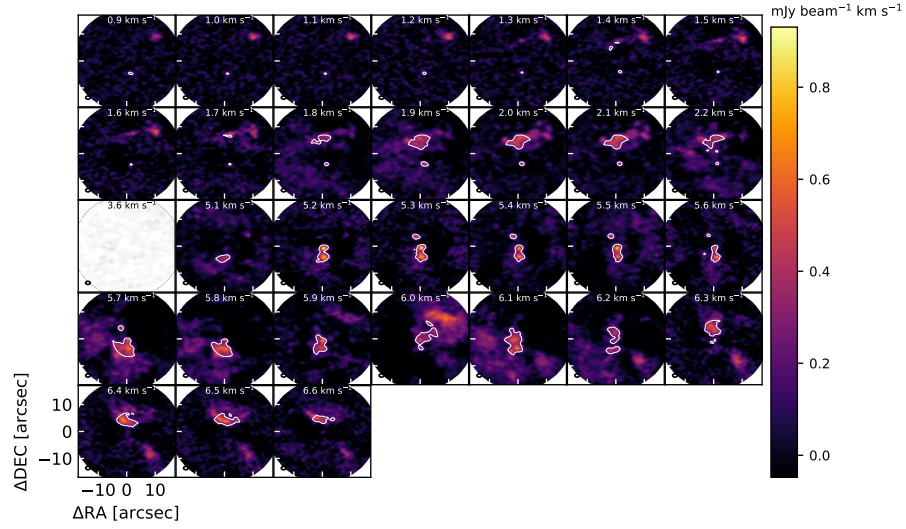
FIGURE 2.23: ^{12}CO channel maps for [GY92] 344, analogous to Fig. 2.19
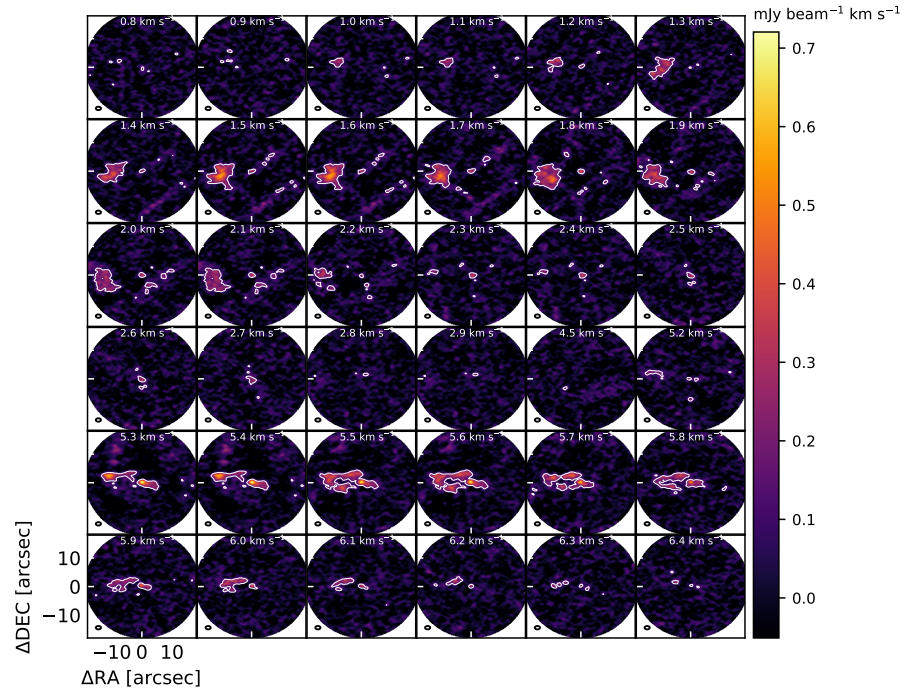
FIGURE 2.24: ^{12}CO channel maps for 2MASS J16274825-2442256, analogous to Fig. 2.19
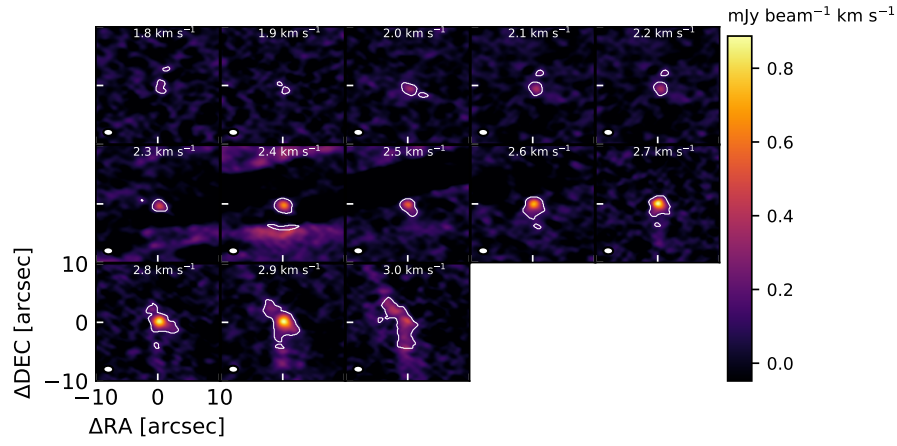
FIGURE 2.25: ^{12}CO channel maps for BKLT J162858-244054, analogous to Fig. 2.19
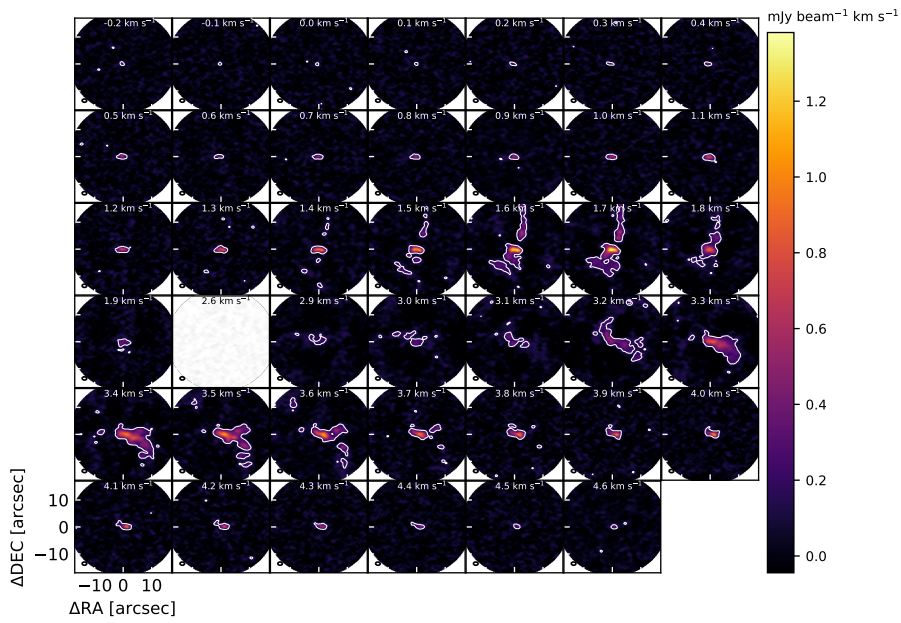
FIGURE 2.26: ^{12}CO channel maps for 2MASS J16313383-2404466, analogous to Fig. 2.19
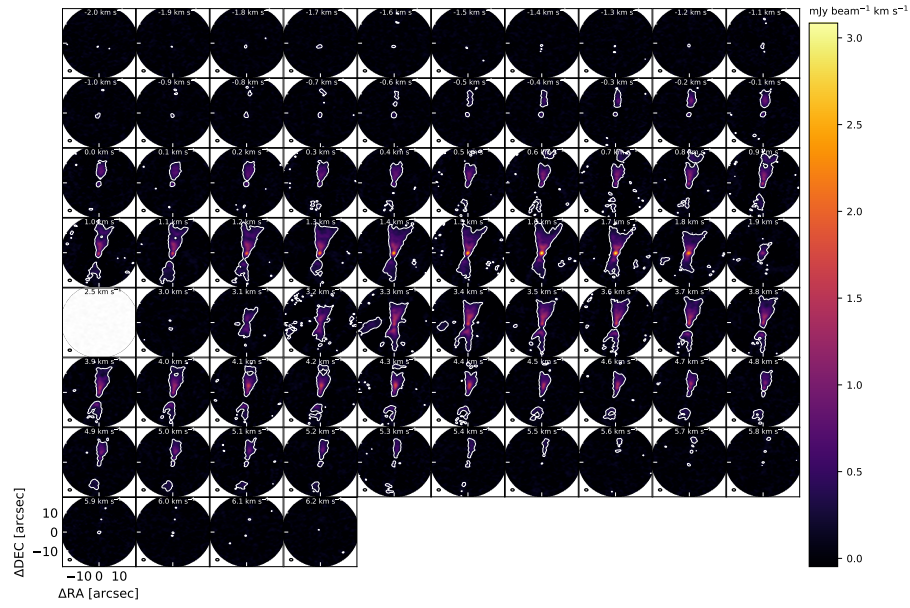
FIGURE 2.27: ^{12}CO channel maps for 2MASS J16313679-2404200, analogous to Fig. 2.19
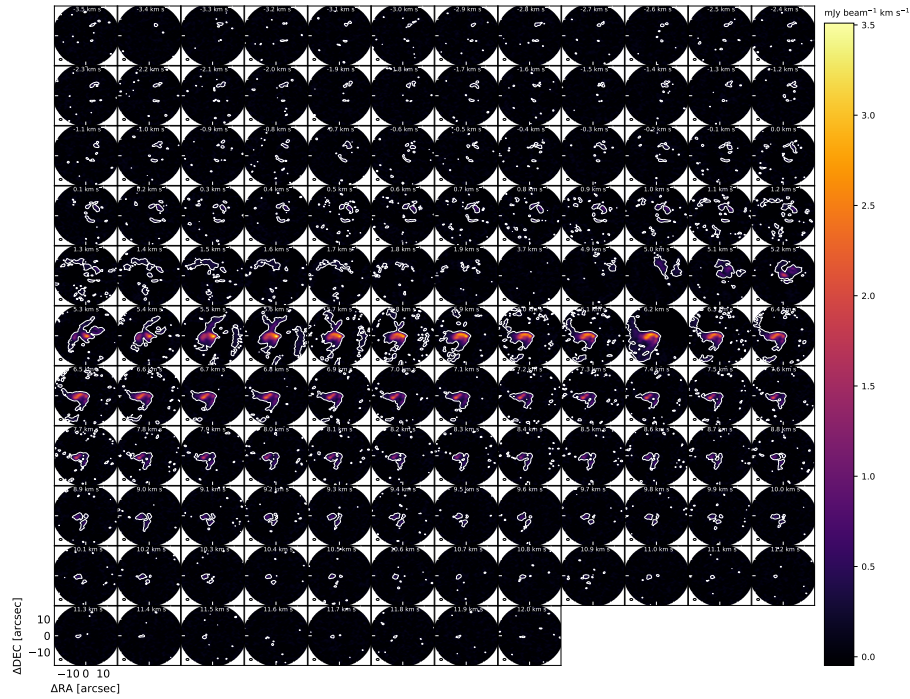
FIGURE 2.28: ^{12}CO channel maps for ISO-Oph 200, analogous to Fig. 2.19
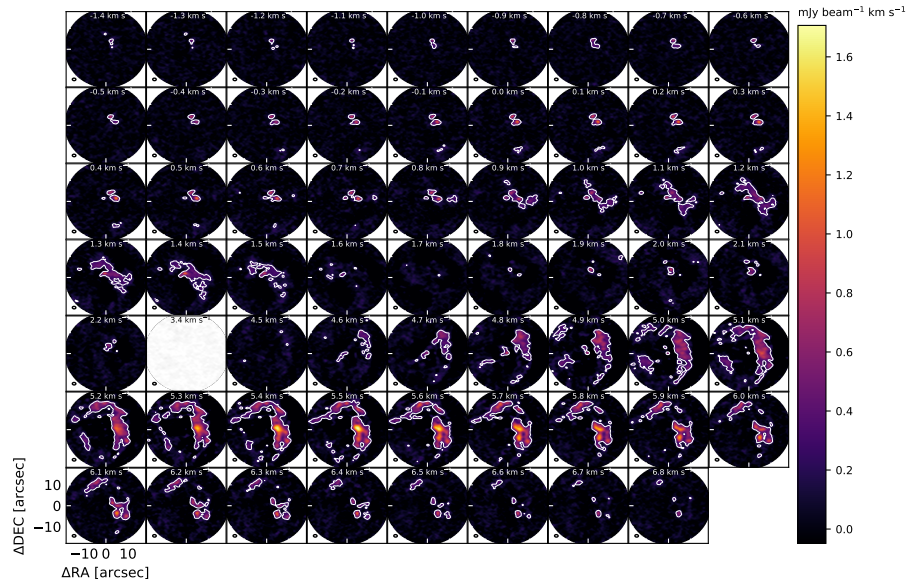
FIGURE 2.29: ^{12}CO channel maps for ISO-Oph 204, analogous to Fig. 2.19
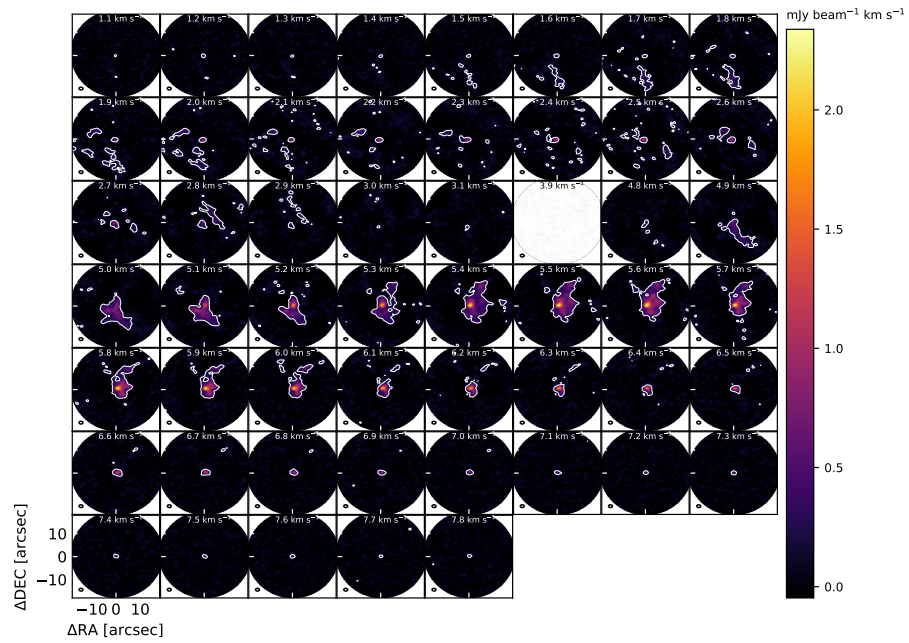
FIGURE 2.30: ^{12}CO channel maps for WLY 2-69, analogous to Fig. 2.19

Chapter 3

A Tale of Two Transition Disks: ALMA long-baseline observations of ISO-Oph 2 reveal two closely packed non-axisymmetric rings and a ~2 au cavity

Chapter 3. A Tale of Two Transition Disks: ALMA long-baseline
94   *observations of ISO-Oph 2 reveal two closely packed non-axisymmetric*
rings and a ~2 au cavity

3.1 Abstract

ISO-Oph 2 is a wide-separation (240 au) binary system where the primary star harbors a massive (M_{dust} ~40 $M_{\oplus}$) ring-like disk with a dust cavity ~50 au in radius and the secondary hosts a much lighter (M_{dust} ~0.8 $M_{\oplus}$) disk. As part of the high-resolution follow-up of the "Ophiuchus Disk Survey Employing ALMA" (ODISEA) project, we present 1.3 mm continuum and ^{12}CO molecular line observations of the system at 0.02" (3 au) resolution. We resolve the disk around the primary into two non-axisymmetric rings and find that the disk around the secondary is only ~7 au across and also has a dust cavity (r ~2.2 au). Based on the infrared flux ratio of the system and the M0 spectral type of the primary, we estimate the mass of the companion to be close to the brown dwarf limit. Hence, we conclude that the ISO-Oph 2 system contains the largest and smallest cavities, the smallest measured disk size, and the resolved cavity around the lowest mass object ($M_{\star}$ ~0.08 $M_{\odot}$) in Ophiuchus. From the ^{12}CO data, we find a bridge of gas connecting both disks. While the morphology of the rings around the primary might be due to an unseen disturber within the cavity, we speculate that the bridge might indicate an alternative scenario in which the secondary has recently flown by the primary star causing the azimuthal asymmetries in its disk. The ISO-Oph 2 system is therefore a remarkable laboratory to study disk evolution, planet formation, and companion-disk interactions.

3.2 Introduction

The Atacama Large Millimeter/submillimeter Array (ALMA) is revolutionizing the field of disk evolution and planet formation by studying large populations of protoplanetary disks in nearby molecular clouds and individual objects in unprecedented detail. On one hand, disk demographic surveys

provide information on fundamental disk properties such as mass and size as a function of stellar mass (Pascucci et al., 2016; Barenfeld et al., 2016), age (Ansdell et al., 2017; Ruíz-Rodríguez et al., 2018), and multiplicity (Cox et al., 2017; Manara et al., 2019; Zurlo et al., 2020). On the other hand, detailed high-resolution studies can deliver images at 3-4 au resolution at the distance of nearby star-forming regions (140–200 pc) such as Taurus, Lupus, Ophiuchus, and Chamaeleon in order to study their substructures (ALMA Partnership et al., 2015; Andrews et al., 2018).

With almost 300 targets, the "Ophiuchus Disk Survey Employing ALMA" (ODISEA) project (Cieza et al., 2019; Williams et al., 2019) is so far the largest of the disk demography surveys in nearby clouds and has identified several interesting objects for high-resolution follow-up observations. One of the most interesting targets identified by ODISEA is ISO-Oph 2, a binary system with a projected separation of 240 au and a flux ratio of 0.08 in the K-band (Ratzka, Köhler, and Leinert, 2005). The primary star has an M0 spectral type and an accretion rate typical of Classical T Tauri stars ($10^{-8.7}$ $M_\odot yr^{-1}$; (Gatti et al., 2006) and hosts a massive ($M_{dust} \sim$40 $M_\oplus$) disk with the largest dust cavity ($\sim$50 au in radius) seen in the Ophiuchus cloud (Cieza et al., 2019). The secondary star, which lacks a spectral classification in the literature, arbors a much lighter ($M_{dust} \sim 0.8$ $M_\oplus$) disk that remained unresolved at 30 au resolution (Cieza et al., 2019).

ISO-Oph 2 was observed with ALMA as part of the high-resolution follow-up of the 10 brightest ODISEA targets that were not included in the ALMA Cycle-4 Large Program DSHARP (Andrews et al., 2018). The full sample of ODISEA targets observed at high-resolution is discussed in Cieza et al. (in prep.). Here we present the initial results of this long-baseline program and show that the ISO-Oph 2 system displays several exceptional properties when observed at 0.02″ (3 au) resolution.

Chapter 3. A Tale of Two Transition Disks: ALMA long-baseline
96   observations of ISO-Oph 2 reveal two closely packed non-axisymmetric
rings and a ∼2 au cavity

3.3   Observations and data analysis

3.3.1   ALMA observations

The long-baseline data of ISO-Oph 2 were obtained during ALMA Cycle 6
under program 2018.1.00028.S. The source was observed in Band-6 (1.3 mm/230
GHz) in two different epochs with baselines up to 16.2 km. The correlator
setup was chosen to maximize the continuum bandwidth (7.5 GHz). Three
spectral windows were configured in Time Division Mode, with spectral res-
olution of 43 $km\,s^{-1}$, and overlap the continuum frequency from the Cycle 4
ODISEA observations at ∼217, 219, and 233 GHz. A fourth baseband was
centered in the ^{12}CO J = 2-1 line (230.538 GHz) and delivers a modest reso-
lution of 1.5 $km\,s^{-1}$, enough to isolate the line (line width ∼5 $km\,s^{-1}$) and
trace the spatial distribution of the gas. The observing log of the Cycle-6
long-baseline observations are shown in Table 3.1, together with relevant in-
formation on Cycle 4 data at lower spatial resolutions (Cieza et al. 2019, PID
= 2016.1.00545.S) that we use to complement our new ^{12}CO observations (see
Section 3.3).

3.3.2   Data analysis

All data sets were calibrated using the ALMA Science Pipeline which in-
cludes Water Vapor Radiometer and system temperature correction, as well
as bandpass, phase, and amplitude calibration.

   Continuum and line imaging was performed using the TCLEAN task in
CASA v.5.6.1 (McMullin et al., 2007), with Briggs weighting and robust pa-
rameter of 0.5. Continuum images were produced using the continuum spec-
tral windows of the high resolution data only, yielding an image with synthe-
sized beam of $0.02'' \times 0.03''$ centered at 225 GHz. Since there are two sources
in the field of view, manual masks around each source were defined during

the CLEANing process. Two iterations of phase-only self-calibration were conducted on each epoch separately using a mask covering both sources. Self calibration improved the signal-to-noise ratio of the final image by a factor of 1.7. The resulting image is shown in Figure 3.1, and its properties are described in Table 3.1.

Line imaging of the ^{12}CO gas was performed combining the datasets with 0.02", 0.2", and 1.1" resolution. The datasets at 0.02" and 0.2" resolution (2019 and 2017 epochs) were recentered using the location of the secondary disc at 0.02″ resolution in the continuum as reference point. The coordinates of the 1.1″ images (2018 epoch) were taken at face value as the secondary disc is only barely detected. Self-calibration of the line data from all epochs and resolutions was done by applying the self-calibration solutions derived from the respective continuum datasets. We used the UVCONTSUB task to substract the continuum from the line data, after which the data was CLEANed using an auto-masking process (for regions up to 3×rms) in TCLEAN to generate line cubes with 1.5 km s^{-1} resolution. To obtain an optimal balance between spatial resolution and sensitivity, we applied an UVTAPER with an UPPERTAPER = 0.1ARCSEC.

3.4 Results

3.4.1 (Sub)stellar masses

In order to estimate the mass of each component in the binary system, we first use the spectral type of the primary star (M0, Gatti et al. 2006) and the infrared photometry to estimate its extinction, mass and age, and then use the flux ratio in the K-band to estimate the mass of the secondary object assuming the same age and extinction. We assume that the observed J-K color from 2MASS (Cutri et al., 2003) is photospheric and calculate the extinction

in K-band as $A_K = 0.53 \times [(J - K) - (J - K)_O]$, where $(J - K)_O$ is the photospheric color of an M0 star. This assumption is supported by the fact that the ALMA data place an upper limit of 0.1 $M_\oplus$ for the mass of an inner disk around ISO-Oph 2A (see Section 3.4.2), but we note that the presence of K-band excess can not be ruled out for neither the A or B component in the system. This approach gives A_K = 1.3 mag and A_V = 14.5 mag. Adopting the BT-Settl models (Allard, Homeier, and Freytag, 2012) and a distance of 144 pc (Gaia Collaboration et al., 2018), we estimate that the primary is a ~1 Myr old star with a mass of 0.5 $M_\odot$ based on its spectral type and extinction corrected absolute K-band magnitude, 2.45. Similarly, the flux ratio indicates that the secondary has a extinction-corrected K-band absolute magnitude of 5.2, corresponding to a T_{eff} of 2900 K and a mass of 0.08 $M_\odot$, right at the stellar/substellar boundary. However, we note that stellar masses and ages of low-mass stars and brown dwarfs are model-dependent and notoriously difficult to estimate for individual objects (Gonzales et al., 2020), and hence that these values must be taken with caution.

3.4.2   Continuum

Primary disk

The disk around the primary star shows a large cavity devoid of millimeter emission and a narrow and structured continuum outer disk (see Fig. 3.2). The outer region is bright and breaks into substructure in the form of two narrow rings, which show spectacular azimuthal asymmetries. The outermost structure peaks toward South of the star and presents a prominent decrement to the North-West. On the other hand, the innermost structure peaks toward the North-West and becomes nearly undetectable toward the South-East. We do not detect emission near the center of the cavity, placing strong constraints on the mass of a putative inner disk. Based on the 5-σ noise (0.18 mJy/beam)

of the continuum observations and adopting the same basic assumptions as in Cieza et al. (2019), this limit corresponds to a dust mass of 0.1 M$_\oplus$ for an unresolved inner disk.

In order to highlight the substructure in the disk, a process of unsharp-masking was applied (Pérez et al., 2020a), which accentuates the narrow rings. This sharper image is obtained by convolving the image with a circular Gaussian kernel to produce a smoothed version of the disk which is later subtracted from the original image.
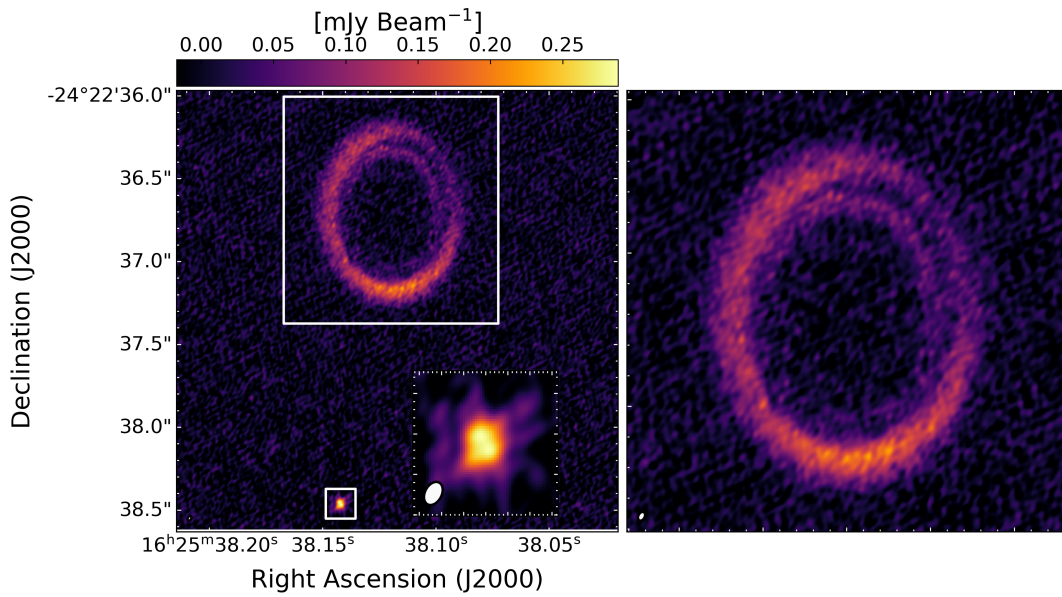
FIGURE 3.1: Left: 1.3 mm image of the ISO-Oph 2 system, including the disks around both stellar components and a zoom-in of the secondary disk where the cavity is marginally resolved. Right: A zoom-in of the primary disk with two non-axisymmetric rings. North is up and East is to the left.

In Figure 3.2, we show the unsharp image of the disk around the primary deprojected to a Position Angle (*PA*) and an inclination (*i*) of 0.0 deg (panel a) and the corresponding radial profile (panel b). To perform the deprojection, we explored a grid of different *PA*, *i*, and centers. We find that a *PA* = 1.0 deg (E of N), and an *i* = 36.4 deg, together with the coordinates from the Gaia Data Release 2 (Gaia Collaboration et al., 2018) corrected for proper motions[1]

---

[1]Ra = 246.408838 deg; Dec = −24.376830 deg; Epoch = 2015.5; pmra = −5.4 mas yr^{-1}; pmdec = −25.2 mas yr^{-1}

Chapter 3. A Tale of Two Transition Disks: ALMA long-baseline
100 *observations of ISO-Oph 2 reveal two closely packed non-axisymmetric*
rings and a ~2 au cavity

provide the most circular deprojected image. This suggests that the primary star is likely to be located at the center of the disk to within ∼15 mas or 2 au). Both rings show azimuthal variations in intensity and/or width, which are difficult to disentangle, but as shown in panel b, when averaged over azimuth, the inner ring extends from a radius of ∼0.3″ to ∼0.4″ (43 to 58 au), while the outer one does from a radius of ∼0.4″ to ∼0.6″ (58 to 86 au).

Figure 3.2 (panel b) additionally includes the K-band 5-σ contrast as a function of radius (dashed-line) corresponding to the VLT-NACO image of ISO-Oph 2 presented in Fig. 6 of Zurlo et al., 2020. While the 2.2 μm NACO data is not particularly deep, it allow us to rule out the presence of an equal brightness binary at the resolution limit of the observations 0.05″ (7 au) and of a 0.08 M$_\odot$ brown dwarf (K-band contrast ∼0.08) at distances larger than 50 au from the primary. In Figure 3.2, we also show the deprojected profile in polar coordinates (panel c), which we also average over the radial range of each ring, 0.3″ – 0.4″ for the inner ring and 0.4″ – 0.6″ for the outer ring (panel d). These radially-averaged azimuthal profiles allow us to better characterize the azimuthal asymmetries. The outer disk has a minimum at a *PA* of ∼50 deg West of North, but emission is detected at all azimuths. The inner ring is fainter and radially narrower. It has an azimuthal extension of ∼260 deg (from *PA* = 100 deg East of North to 160 deg West of North), peaking close to the minimum seen in the outer disk.

Secondary disk

The disk around the secondary star is only 1.3 mJy and remained unresolved in our 0.2″ resolution observations (Cieza et al., 2019).The long-baseline data shows that the disk is very compact, 0.05″ (7 au) across (FWHM measured with the IMFIT routine within CASA) and exhibits the double peak (Fig. 3.1, panel b) characteristic of a transition disk with a marginally resolved inner dust cavity.
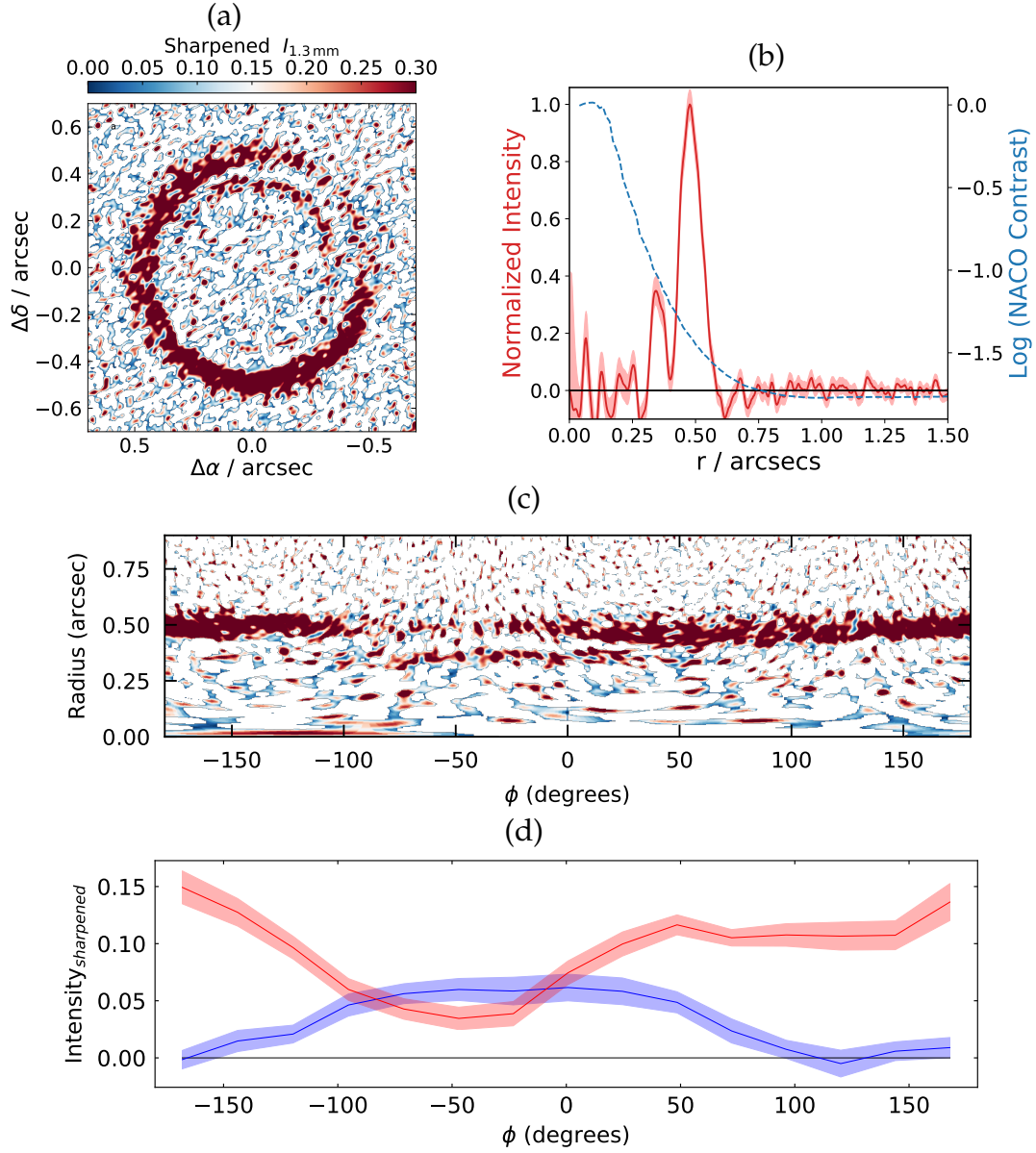
FIGURE 3.2: (a) Deprojected image of the disk around the primary with normalized intensity to 0.3×peak. (b) Average deprojected radial profile of the disk around the primary and the 5-σ contrast curve of the VLT-NACO observations at 2.2 μm reported by Zurlo et al. (2020). (c) Polar radial deprojection from image (a). (d) Same as panel (c), but averaged over radius, between 0.3-0.4″ and 0.4-0.6″, for the inner ring (blue line) and outer ring (red line), respectively. Shaded regions correspond to the errors in the mean.

Chapter 3. A Tale of Two Transition Disks: ALMA long-baseline
102 *observations of ISO-Oph 2 reveal two closely packed non-axisymmetric*
rings and a ∼2 au cavity

Given the small flux and angular size of the disk, which push the limit of ALMA's capabilities, we estimate the size of the dust cavity adopting an analytical approach based on deprojecting the visibilities to 0.0 deg i and 0.0 deg PA in the $u - v$ plane. In particular, the Real component of the visibilities as a function of deprojected $u - v$ distance for a face-on narrow ring is a zeroth-order Bessel function and the imaginary flux components of such a ring is 0.0 at all spatial frequencies. Following Hughes et al. (2007), the location of the first null on the Bessel function, R_{null}, is related to the cavity radius, R_{cav}, as follows:

$$R_{null}(k\lambda) = \frac{77916}{\pi^2} \left(\frac{Distance}{100\ pc} \right) \left(\frac{1\ au}{R_{cav}} \right) \qquad (3.1)$$

The deprojected u-v-distances are given by $R = \sqrt{d_a^2 + d_b^2}$, where $d_a = \sqrt{u^2 + v^2} \sin \phi$ and $d_b = \sqrt{u^2 + v^2} \cos \phi \cos i$, $\phi = \arctan(v/u) - PA$ (Lay, Carlstrom, and Hills, 1997).

In order to construct the visibility profile of the disk around the secondary star, we first subtracted the visibilities of the CLEAN model of the disk around the primary from the visibility data, following Pérez et al. (2020b). We also changed the phase center to the position of the secondary as measured with IMFIT in CASA, which also provided initial approximations for the i and PA of the secondary disk.

More precise values were obtained by minimizing the imaginary components in the imaginary part of the visibility profile. The resulting visibility profile corresponding to an i = 10 deg and PA = 122 deg is shown in Figure 3.3. A null is seen at 5000 ± 500 kλ, which according to Equation 1 corresponds to cavity radius of 2.2± 0.25 au. Given the small size of the outer disk (FWHM/2 = 3.5 au), we conclude that the secondary disk also shows a ring-like morphology like the primary (e.g., with a width smaller than its inner radius).
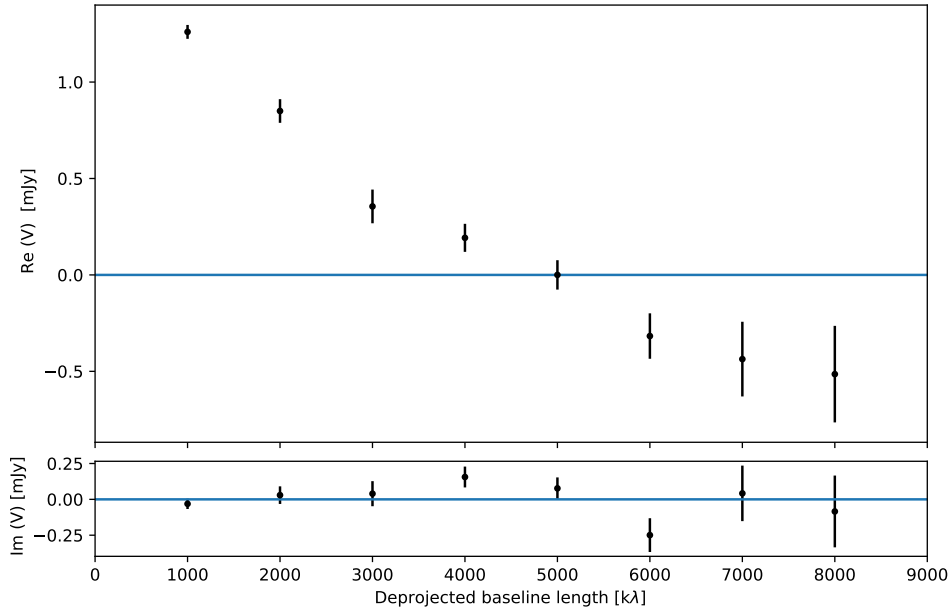
FIGURE 3.3: The deprojected visibility profile of the disk around the secondary. Both the Real (top panel) and the Imaginary (bottom panel) parts are shown. A null is seen at a baseline length of $\sim$5000$\pm$500 kλ (6500 m), indicating a dust cavity with a radius of $\sim$2.2 AU.

3.4.3 Molecular gas (^{12}CO) data

We find that the molecular line data of ISO-Oph 2 system exhibits interesting features as well. The ^{12}CO line peaks inside the cavity, but the emission is shifted toward the south, reaching the secondary (Fig. 3.4, panel a). As shown in the Position-Velocity (P-V) diagram (panel b), the disk around the primary is mostly detected at $\sim$1 and $\sim$4 km/s, while there is significant cloud contamination at velocities between 2 and 3 km/s. The secondary, on the other hand, is mostly detected at $\sim$1.5 km/s. At velocities between 0 and 2 km/s, the P-V diagram also shows what seems to be a bridge of gas connecting both disks. This bridge becomes even more evident in the channel map containing emission between 0.25 and 1.75 km/s (panel c).

Finally, in panel d of Figure 3.4, we show the intensity-weighted mean

Chapter 3. A Tale of Two Transition Disks: ALMA long-baseline
104 *observations of ISO-Oph 2 reveal two closely packed non-axisymmetric*
rings and a ∼2 au cavity

velocity (moment-1) map of the ^{12}CO data. This map is consistent with Keplerian motion as the extreme velocities are observed along the major axis of the disk. We therefore conclude that there is no indication of an inner cavity in the gas, which is consistent with the relatively high accretion rate of the system ($10^{-8.7}$ M$_\odot$yr^{-1}; Gatti et al. 2006). We also note that the kinematic center of the disk (where the minimum and maximum velocities converge) coincides with the expected location of the star based on the position and proper motions from Gaia.

3.5 Discussion

ALMA observations at 3-30 au resolution have shown that protoplanetary disks in general, and transition disks in particular, have diverse substructures. The DSHARP project, the largest long-baseline survey of disks thus far (Andrews et al., 2018) has revealed that narrow rings and gaps are the most common substructure in protoplanetary disks. Unfortunately that project does not include transition objects. More recently, Francis and van der Marel (2020) collected a large sample of ∼40 of disks with large (r > 25 au) dust cavities. Around half of the stars in that sample have dusty inner disks detected, something that is not seen in ISO-Oph 2 A.

Most transition disks are azimuthally symmetric, but several examples with azimuthal asymmetries do exist such as IRS-Oph 48 (van der Marel et al., 2013), HD 142527 (Casassus et al., 2013), HD 135344B (Cazzoletti et al., 2018), SR 21 (Muro-Arena et al., 2020), CIDA 9, RY Lup and HD 34282 (Long et al., 2019; Francis and van der Marel, 2020). These asymmetries are most likely dynamical in nature and can be planet-induced vortices (Hammer et al., 2019) or be produced by stellar companions (Price et al., 2018; Calcino et al., 2019). However, the disk around ISO-Oph 2 A is particularly rare because it shows not one, but two closely packed and azimuthally asymmetric
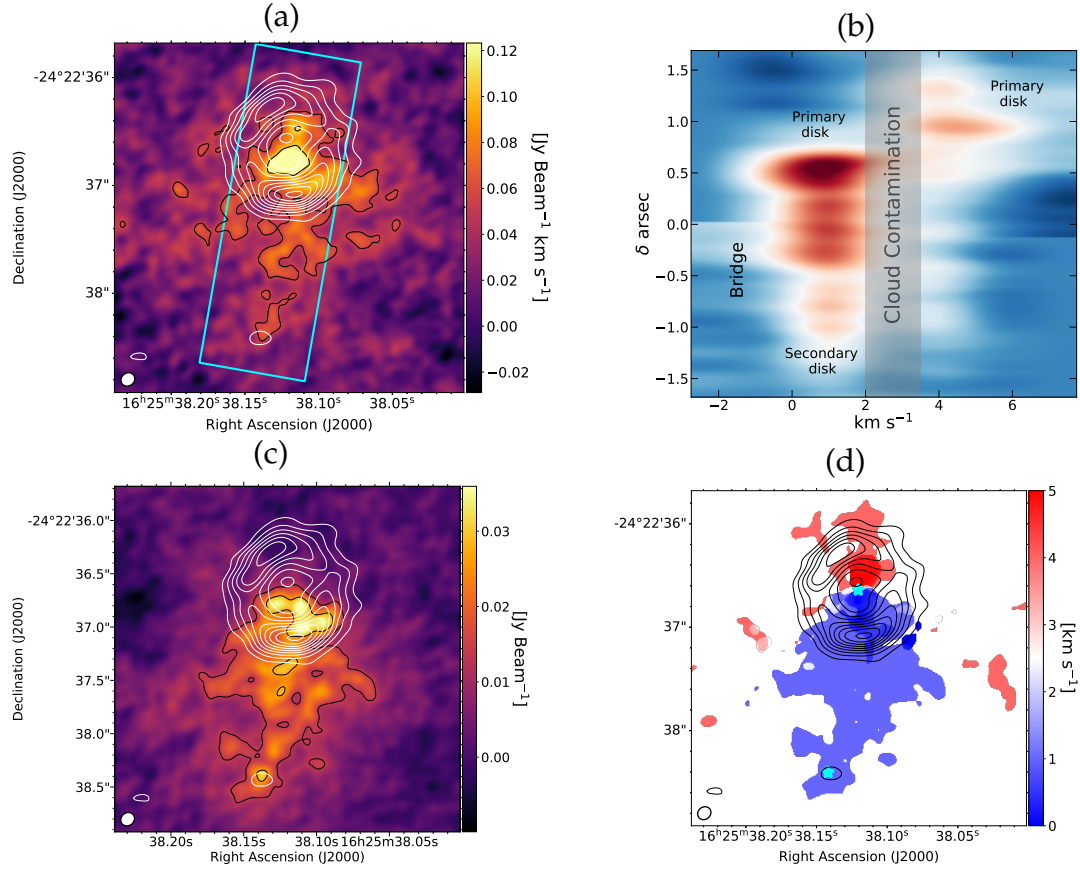
FIGURE 3.4: (a): the Moment-0 map from the combined visibilities at 0.03″, 0.2″ and 1.1″ resolution imaged with an 0.1″ beam. The black contours represent emission at $\geq 3 - \sigma$ with steps of 3-σ. Continuum contours in 0.2″ are shown in white. (b): the Position-Velocity diagram with PA=169°, length=3.4″ and averaging width=1″ (see rectangle in panel a), revealing significant emission connecting both disks at ∼1.5 km/s. (c): the channel map corresponding to velocities between 0.25 and 1.75 km/s. (d): the moment-1 map of the same data from panel (a). The position of the stars from Gaia, corrected for the proper motion of the primary are also indicated.

rings, resembling other very complex systems such as MWC 758 (Dong et al., 2018). As demonstrated by Pérez et al. (2019), a single migrating planet can produce multiple rings, but it remains to be established by future hydrodynamic modeling if the rings produces this way can be as non-axisymmetric as seen in ISO-Oph 2 A.

The possible bridge of gas connecting both disks in the system (Fig. 3.4) might indicate a different origin for the complex structure of the disk around the primary. At its current location, the secondary itself is too far away (240 au) to disturb the primary disc significantly. However, if ISO-Oph 2 is a very eccentric binary system or an unbound flyby, it is possible that some of the structure seen in the primary disk is the result of the recent close approach of ISO-Oph 2 B. Stellar flybys are rare but still statistically possible in low-mass star-forming regions (Cuello et al., 2020). Possible disk flybys reported in the literature include RW Aur (Dai et al., 2015), HV Tau and DO Tau (Winter, Booth, and Clarke, 2018), AS 205 (Kurtovic et al., 2018) and UX Tau A (Ménard et al., 2020). These flybys typically exhibit arcs of gas hundreds of au long connecting the disks in the system, in agreement with the results of hydrodynamic models (e.g. Cuello et al. 2020). The same models show that flybys also trigger spiral arms within the disks. Therefore, we speculate that, *if the initial configuration are two narrow rings*, a close approach could result in azimuthal asymmetries similar to the ones observed in the disc around the ISO-Oph 2 A disk.

Unfortunately the Gaia Data Release 2 only provides proper motions for the primary star and is not possible to constrain the relative motion of ISO-Oph 2 A and ISO-Oph 2 B with enough precision to assess the likelihood of the flyby scenario. However, we note that, assuming the closest encounter occurred 500 yr ago, as in the simulation presented by Cuello et el. (2020), the relative proper motion between the primary an the secondary would be expected to be ∼3.4 mas/yr. The flyby hypothesis could also be tested in the

future with hydrodynamic modeling tailored to the system.

The disk around ISO-Oph 2 B is also very interesting as it has one of the smallest cavities ever resolved at (sub)mm wavelengths. With a radius of just ∼2.2 au, the cavity size is at the limit of ALMA's resolution at the distance of the closest molecular clouds (d ∼ 140 pc). Interestingly, TW Hydra, one of the closest stars to Earth with a protoplanetary disk (d = 60 pc) also hosts a transition disk with a very small cavity, only ∼1 au in radius (Andrews et al., 2016). However, unlike TW Hydra, ISO-Oph 2 B has a disc that seems to be narrow (width/radius < 1.0), resembling the structures of other disks such as ISO-Oph 2 A, Sz 91 (Canovas et al., 2016), and T Cha (Hendler et al., 2018), but in a much smaller scale (by a factor of 15-40 in radius). Furthermore, ISO-Oph 2 B also is the lowest-mass object with a resolved dust cavity in the Ophiuchus molecular cloud, and possible in any region Based on the age (∼1 Myr) and mass (0.08 $M_\odot$) estimates discussed in Section 3.1, ISO-Oph 2 B should have an M6.5 spectral type. However, all the 7 objects that have resolved cavities in the ODISEA sample have earlier spectral types (Ruiz-Rodriguez et al. in prep). That is also the case for all pre-main-sequence stars with transition disks identified in Ophiuchus based on their IR SEDs (Cieza et al., 2010; Merín et al., 2010); and all the transition objects with mm data (from all regions) recently compiled by Francis and van der Marel (2020), and Pinilla, Pascucci, and Marino (2020).

3.6 Summary and Conclusions

We present new 1.3 mm ALMA long-baseline data of the ISO-Oph 2 system at 3 au resolution. Our main results and conclusions are as follow:

1) The ring-like structure of the primary disk is resolved into two non-axysimmetric rings, suggesting dynamical disturbances. Future hydrodynamic modeling could help explaining the origin of these substructures and

establish whether they are due to an internal or an external disturber.

2) The high-resolution continuum observations reveal the disk around the secondary is 7 au across (FHWM) and has an inner cavity just 2.2 au in radius. This implies that ISO-Oph 2 B has the smallest (transition) disk ever imaged in Ophiuchus and likely has a ring-like morphology (width $<$ inner radius).

3) The flux ratio in the of ISO-Oph 2 system at 2.2 μm (0.08) and the spectral type of the primary (M0) implies the secondary is at the brown dwarf mass limit, rendering ISO-Oph 2 B the lowest mass object in the cloud with a resolved dust cavity in its disk.

4) The ^{12}CO observations indicate that there is significant gas within the large cavity in the primary disk and suggest that the two disks might be connected by bridge of gas. This bridge might indicate that the secondary object recently flew by the primary and provides an alternative scenario for the origin of the azimuthal asymmetries in the disk around the primary.

UTC Date	2019-06-21/02:07	2019-06-12/02:15	2018-05-26/06:44	2017-07-13/03:29
Config	C43-8/9	C43-8/9	C40-2	C40-5
Baselines	82 m - 16.2 km	82 m - 16.2 km	14 m - 313 m	16 m - 2.6 km
Mean PWV (mm)	0.85	1.19	1.07	1.8
Calibrators	J1517-2422, J1633-2557, J1642-2849	J1517-2422, J1633-2557, J1642-2849	J1517-2422, Ganymede, J1625-2527	J1517-2422, J1517-2422, J1625-2527
Beam size ($''$)^a	0.02×0.03	0.02×0.03	1.1×1.1	0.2×0.3
Spectral resolution (km s^{-1})	1.5	1.5	0.08	0.08
Continuum rms (mJy beam^{-1})	3.6×10^{-2}	2.7×10^{-2}	2.4×10^{-1}	3.7×10^{-1}
Line rms (mJy beam^{-1} km s^{-1})	26.5	18.7	89.5	53.4

TABLE 3.1: ALMA observations of the ISO-Oph 2 system. (a) beam size corresponds to Briggs weighting and robust parameter of 0.5.

Chapter 4

Conclusions

4.1 Summary

Studying the environments of Young Stellar Objects (YSOs) is crucial for understanding the processes governing the development of evolved planetary systems as we know them. Similarly, comprehending planetary formation within the protoplanetary disk provides insights into the past of our own planet and the solar system.

From the formation of molecular clouds, the environment is chaotic and dynamic, posing challenges even after proto-stars form. Outflows and inflows of material set the stage for the future architecture of stars and orbiting planets. The quantity of available material for accretion by the star or planets within the disk, as well as interactions between the star, disk, envelope, jets, and stellar winds, could all play pivotal roles in explaining and projecting the future of observed planetary systems and those still forming.

In Chapter 2, we studied 21 proto-BD candidates of Class I and FS. A significant proportion (16/21) exhibited continuum detection at a spatial resolution of 0.3" (∼45 au), revealing compact dust disks that were mostly unresolved spatially, as expected given their classes. Moreover, none showed substructures or indications thereof. Regarding gas lines, using observations with higher sensitivity and lower angular resolution (1.1" or 150 au), central source-related signals were detected in 12/21 cases. Eleven sources showed

emission in both continuum and molecular lines, while one exhibited gas emission but not dust emission. For optically thin molecular lines like ^{13}CO and C^{18}O, emission often originated from the protoplanetary disk (PPD), while optically thick ^{12}CO displayed various structures such as outflows, possible streamers, and envelopes. Although the morphologies in most cases were not entirely clear to discern the nature of the detected emission, they provided initial insights into the varying interaction between the envelope, disk, and proto-BD candidate in Class I and FS sources. Lastly, we compared the continuum emission and physical properties of the disks with Class II proto-BD candidates in Ophiuchus, noting a higher prevalence of younger sources (Class I and FS), suggesting either slower evolutionary development or delayed formation compared to other low-mass YSOs in the cloud.

Similarly, the comprehensive census of line detections across all ODISEA sources was promising. However, observations for late Class II and Class III sources lacked the sensitivity to detect signals $>3 \times$ rms, with only one source showing high SNR detection. For the rest, the detection percentages were 65% for ^{12}CO, 37% for ^{13}CO, and only 15% for C^{18}O relative to the complete sample of Class I, FS, and early Class II sources. Almost all emission from optically thin molecules (^{13}CO and C^{18}O) originated from the disk. Rotational keplerian gas allowed mass dynamic curve fitting based on Position-Velocity diagrams in some cases, yielding estimates for the masses of the respective stars. The expected trend was observed for extended structures, with most observed outflows associated with Class I objects, fewer with FS, and very few with Class II.

In light of the findings presented in Chapter 2, this sample constitutes compelling evidence for planetary formation around BDs, based on the amount of material in the disk, comparable to the formation of planets around low-mass stars. Furthermore, consistent with the detection of planets orbiting

BDs, this sample provides information consistent with observations in already evolved systems.

Based on the results obtained for the molecular lines, the presence of Outflows extending thousands of au around the proto-BD candidates is a significant step towards elucidating the early formation environment of BDs. In this environment, stellar cores would be embedded in a material envelope, analogous to low-mass stars. The interaction between the proto-BD and the disk produces jets that traverse and begin to excavate the envelope, giving rise to these large-scale Outflows. While other possible formation scenarios cannot be definitively ruled out, they are less likely due to the requirement of dense and compact material in the form of an envelope from the outset of formation.

Deeper investigations into the relationship between mass outflowing and mass accretion rate could confirm a physical mechanism that interrupts or simply slows down material accretion, either from the early stages of BD core formation.

In Chapter 3, at planetary formation scales, observations at spatial resolutions < 5 au are indispensable for clearly observing the evolution and behavior of substructures within PPDs. In the case of ISO-Oph 2, one of the most intriguing systems in the Ophiuchus molecular cloud, two disks with cavities were observed. The larger cavity had a radius of $\sim$50 au, while the smaller one was $\sim$2.2 au, both observed in Ophiuchus for the first time. The primary source exhibited two non-axisymmetric rings, possibly due to interaction with a planet within the cavity, shadowing from a massive external source, or a recent flyby of the secondary source. Additionally, CO lines present in these observations showed rotating gas within the primary source's cavity and a gas bridge between both sources. The past interaction between both objects might be explained by flyby or disk expulsion models, but deeper and higher angular resolution line observations are needed for

confirmation. Finally, the secondary source is in the sub-stellar regime, so resolving this system could also provide evidence of Brown Dwarf formation.

ISO-Oph 2 emerges as an ideal natural laboratory for studying various physical phenomena, particularly the interaction of YSOs in the early stages of formation within SFRs. While these observations allow for the observation of a molecular gas bridge, the sensitivity is not sufficient to distinguish the morphology and dynamics of this interaction, but at least it would allow possible follow-ups with evolutionary models of flybys between young objects embedded in the cloud.

In the continuum, the non-axisymmetric annular structure of the primary source could have various causes, as recently studied by Casassus et al. (2023), where there would be shading given the brightness emitted from a massive source in the same spatial direction as the asymmetry. However, a deformation of the disk, given a recent previous interaction with the secondary source, is also not ruled out. Whatever the case, there are few examples of transition disks with all these components.

Finally, the large cavity present in the secondary source challenges several existing models of planetary formation. With a diameter of $\gtrsim 80$ au, if the cause of this cavity is the presence of a giant protoplanet within it, then this planet would orbit the central proto-star at a tentative distance of ~ 50 au, which in combination with the low age of the system (~ 1 Myr), would be an impossible protoplanet for most of the planetary formation theories presented in Chapter 1. Additionally, the presence of gas within the cavity could suggest that the potential giant protoplanets would have even more material to accrete, in the case of having reached the critical mass for runaway gas accretion. Models for protoplanets that can carve cavities in transition disks of this type would have masses > 1 M_{Jup}, so they would already have started to accrete gas violently.

4.2 Future Perpectives

4.2.1 Extended Emission around YSOs

To truly understand the evolution of outflows and envelopes around protostars, it is necessary to conduct statistical and parametrized studies of all young sources exhibiting these structures in nearby star-forming regions (SFRs). With the capabilities of state-of-the-art telescopes (e.g., ALMA, JWST), we can detect all these extended structures and measure the physical parameters related to the outflows, such as CO column density, mass outflow rate, dynamical time, size, opening angles, momentum, energy, force, etc. Furthermore, we can compare the structures and their properties in both the infrared (IR) and sub-millimeter (sub-mm) wavelengths, with highly sensitive detections, thus obtaining more precise measurements for the kinematic ranges and morphologies of the outflows.

In 2023, we obtained new data from the Atacama Compact Array (ACA) in ALMA for 20 sources in the Ophiuchus molecular cloud. These young stellar objects (YSOs) exhibit outflows and extended gas emission that have not been fully parameterized with existing observations in the archive. One of the barriers to accurately measuring the extent of these structures is the limited field of view of the ALMA main array (FoV < 40" in diameter). In almost all the sources in these observations, the outflows extended beyond the field of view of the images, requiring observations with smaller antennas to more accurately measure the length of the extended emission. For this reason, we proposed observation time with the ACA. This time was obtained (PID: 2022.1.00450.S) for the Cycle 9 observation, corresponding to the years 2022 and 2023. All details of this successful proposal are provided in Appendix A. While these data have not yet been thoroughly analyzed, it is possible that in some cases, the new field of view and sensitivity may not be

large enough to provide highly precise morphological, dynamic, and kinematic measurements (González-Ruilova in prep.).

However, compared to current main array observations, these data will by far be the most comprehensive dataset for outflows in the Ophiuchus molecular cloud and one of the most extensive for nearby SFRs. For cases where ACA observations continue to be limiting for physically parameterizing the extended structures, observations with NIRCam on the JWST, or single-dish telescopes such as APEX or IRAM, could provide the missing details, thus providing a deeper and more complete big picture of the evolution and presence of outflows in Ophiuchus. Additionally, this will lay the groundwork for conducting analogous studies in other regions of similar ages.

Another continuation of these studies regarding the chemical and physical analysis of disks in sources with outflows is provided by correlations between disk properties and their interaction with the protostar, and the properties of the outflows surrounding these systems. At this point, ALMA's Large Programs such as eDisk (Ohashi et al., 2023), AGE-PRO (Zhang et al., in prep.), and DECO (Cleeves et al., in prep.) will provide key information for young objects of Class 0, I, and FS regarding their disks, such as geometric properties, rotation velocities, mass estimates, among others. These data, along with the confirmation of outflows in the sources, would provide crucial information to discover or confirm correlations between the behavior of the outflows, the disk, and the protostar.

Additionally, new observation programs of the JWST, regarding the same mentioned projects as well as new projects, will allow for a broader view of the chemistry among sources in young evolutionary stages, and more evolved sources (Class II and III), thus providing a clearer idea of how the

interaction between YSOs and the cloud hosting them, through material exchange, could alter the chemistry of the location where planets will subsequently form.

4.2.2 Modelling Protoplanets with Transition Disks

The ODISEA high angular resolution sample mentioned above included transition disks with inner dust cavities (r > 10 au). Figure 1.12 shows transition disks with very interesting radial brightness profiles, already discussed for ISO-Oph 2 in Chapter 3, with either bright rims (DoAr 44, WSB 82, and SR 24S) or narrow rings (RX J1633.9). The origin of these substructures remains to be established, but in principle they can be understood in terms of planet-induced pressure bumps and radial migration of dust (Pinilla et al., 2012). So a logical modelling analysis in those datasets, it is to use numerical models to reproduce the 1.3 mm the substructures of the disks around DoAr 44, WSB 82, and SR 24S and RX J1633.9. The objetives of this future work are to test the planet-disk scenario and confirm that the observed substructures can be reproduced by young giant planets embedded within the disk, and to constrain the location and masses of the putative planets in each disk. Confirming the planetary origin of the substructures would have strong implications for planet formation as it would impose stringent constraints on the formation timescales (1-2 Myr) of giant planets at large distances from their parent stars (tens of au). Furthermore, if the substructures are indeed produced by giant planets in wide orbits, their detailed study would provide a new avenue to investigate a population of planets that remains mostly undetectable by other techniques. Previous studies have been made the same analysis, but just with punctual sources, as similar as the followed methodology outlined in Pinilla et al. (2021), which shows an analysis analogous to the one proposed here. Using ALMA observations at different frequencies

and at high angular resolutions, they studied the disk around the very low mass star (0.1-0.2 $M_{\odot}$) CIDA 1. In this case, they find that planets causing the cavity interior would have a $M_p = 0.5\ M_{\text{Jup}}$ at 12 au.

For the modeling, It can be assumed that the cause of the cavities is a giant planet in formation, which produces a pressure bump near its orbit, thus preventing the rapid drift of dust towards the star. Given this hypothesis, the modeling consists of making, as a starting point, models for protoplanetary disks without any structure, with homogeneous and smooth dust distribution. Combining the properties of the host star, the dust (opacity, grain size distribution, angular momentum, etc.), and the tentative distance for the formation of the protoplanet (from observations), then using hydrodynamic equations (Crida, Morbidelli, and Masset, 2006; Pinilla et al., 2015) we can evolve the initial model in time, obtaining curves for the radial profile of brightness at different times, added to the distribution profiles of density, grain sizes and mass of dust particles.

In any case, there are several other algorithms of dust distribution evolution within the PPDs, those can be used for the purposes of this proposed analysis in the future, looking the gas giants protoplanets that can carve the substructures in Class II and Transition disks.

4.2.3   Planet Formation in situ

As discussed, in part, in Chapters 1 and 3, the formation of planets within PPDs, and their recent detections (Figure 1.5), is a hot topic today. Detection mechanisms, in particular, related to direct imaging (Müller et al., 2018; Benisty et al., 2021), and asymmetries in the emission of Keplerian rotation gas in PPDs (Perez et al., 2015), have been highly sought after, being the main argument of multiple observation programs on different telescopes.

Regarding direct imaging, there are several programs to observe and detect protoplanets directly within the cavities of transition disks. For this purpose, instruments that have emerged in recent years, such as VLTI-ERIS, would provide images with very high angular resolution for transition disks, capable of detecting emission blobs within the disks, corresponding to the brightness of giant protoplanets in young stages. Additionally, along with the upgrades announced for ALMA, ALMA2030, new correlators, the increase in the number of antennas, and the enabling of the most extensive interferometer configuration possible ($\sim$16 km), would allow for much deeper observations, in shorter times, and at higher angular resolutions, making it much easier to detect CPDs within PPDs. Looking further into the future, the operation of the METIS instrument on the Extremely Large Telescope (ELT) could detect, in unprecedented detail, CPDs around YSOs (Oberg et al., 2023).

In the case of indirect observations of CPDs, through gas kinematics, there is currently the large ALMA program, exoALMA (Teague et al., in prep.), which observed 15 transition disks, with high angular resolution and deep sensitivity, to study possible kinks in the gas kinematics in the disks, thereby discovering possible protoplanets causing those kinks. These results are not yet public, but their upcoming release could provide guidelines for the search for protoplanets in disks in the future. For this thesis, the results of exoALMA are relevant for future projects, as the ISO-Oph 2 disk could be a great candidate for conducting analogous observations with high angular resolution, spectral resolution, and deep sensitivity, in search of possible protoplanets forming within the cavity (or on the outer edge of the ring).

Appendix A

A systematic Characterization of the Outflows at Ophiuchus Molecular Cloud

A.1 Abstract

While essentially all nearby ($<$ 200 pc) star-forming regions (Ophiuchus, Lupus, Chamaeleon, and Taurus) have already been surveyed by ALMA in the continuum, a systematic identification and characterization of their molecular outflows is yet to be done. The Ophiuchus molecular cloud is particularly well suitable for such an study as it contains a large number of embedded sources. Using ALMA archival data available for the entire population of young stellar objects in the cloud, we have identified a total of 20 new molecular outflows associated to Class I to Flat spectrum sources. Here we propose a Band-6 project to characterize the morphology and dynamical parameters of the new identified outflows. This will result in the first systematic demographic study of outflows at high angular resolution in a nearby molecular cloud and associated to Class I to Flat spectrum sources, which will help to put into context the many studies of individual outflows already present in the literature.

A.2 Scientific justification

Molecular outflows in young stellar objects are one of the most prominent signposts of star formation, affecting the evolution of the star and disk and influencing the initial conditions for planetary formation. In the current paradigm of low-mass star formation (Shu, Adams, and Lizano, 1987), a dense core accretes material from a surrounding envelope while a bipolar jet is launched from the central protostar, sweeping up the material from the ambient cloud and forming a molecular outflow. Outflows phenomena can extend within less than an au from the central protostar and can reach several parsecs linear size. They are one of the best examples in astrophysics on the connection between small and large scales. Outflows a) play a critical role in disk accretion by carrying the excess of angular momentum from the rotating disk that would otherwise prevent accretion of material onto the central protostar, b) disperse circumstellar envelope material and regulate the star-formation efficiency at the molecular-core scale, and c) affect the dynamics of the cloud as an important source of turbulence (Frank et al., 2014).

Observations of molecular outflows in the submillimetre are a powerful tool to study the evolution of their morphology, kinematics, and dynamical characteristics, as well as the accretion history of the central protostar. The level of outflow activity and the morphology of the outflows evolves with time (Arce and Sargent, 2006). The most powerful outflows are found in the youngest protostars, when they are still embedded in their natal envelope and the outflow activity declines during the later stages of the accretion phase. On the other side the morphological characteristics are also affected by the stage of evolution of the central source, appearing less collimated and widening the outflow cavity with time.

Studies on outflows in the literature expand a wide range of data quality and analysis methods in different star forming regions, which difficult

the combination of results to understand properly the mechanism driving the outflow activity and their evolution with time. More complete and unbiased samples of outflows in any given star forming region are required, and ALMA with its sensitivity and angular resolution capabilities is well suited to perform these studies in a more homogeneous way. In particular the Atacama Compact Array (ACA) in band 6, with resolution ∼5" and LAS∼29" offers a unique opportunity to study outflow interaction at envelope scales (hundreds AU - thousands AU) in nearby star forming regions.

A.2.1 The Ophiuchus disk sample

The Ophiuchus molecular cloud, at a distance of 140±10 pc (Ortiz-León et al., 2017), is particularly well suitable for a systematic study of outflows as it is a southern and nearby star-forming region that contains a large number of young stellar sources, including many tens of embedded objects (Class I and Flat Spectrum sources). As part of the Ophiuchus DIsk Survey Employing ALMA (ODISEA) project (Cieza et al., 2019; Williams et al., 2019; Zurlo et al., 2020), ALMA has already observed the full catalog of 297 Young Stellar Objects (YSOs) in Ophiuchus from the "Cores to Discs" *Spitzer* Legacy Program (Evans et al., 2009).

The ODISEA observations include ^{12}CO(2-1), ^{13}CO(2-1), and C^{18}O(2-1) transitions, with two additional windows dedicated to observe the continuum.

Thus far, all ODISEA papers have focused on the dust continuum, and molecular line data remain unpublished. However, we have recently analyzed the spectral emission line data using ALMA archival data for ODISEA (PID : 2016.1.00545.S) and found ^{12}CO emission that traces clear outflows and envelope structures in 20 of the sources. We find that ∼70% of the sources

with ^{12}CO outflows and/or envelopes are also detected in ^{13}CO and C^{18}O lines.

The available data have spatial resolution ranging from 0.2" to 1" and Maximum Recoverable Scales (MRS) ranging from 3" to 10".

Most of the detected molecular outflows are relatively compact and almost fit within the ALMA 12-m array primary beam in band 6 (~ 30"), with a few of them extended beyond FOV (e.g. Figure A.1). Moreover most of these outflows have not been reported in the literature nor been observed with ALMA before. The small Maximum Recoverable Scales of the ODISEA data implies that a significant fraction of the CO flux are likely to be missed, making new observations with the Compact Array necessarily to properly characterize the morphological and dynamical characteristics of the outflows.

A.2.2   Objectives:

We propose observations using the Atacama Compact Array (ACA) in band 6, which will provide a spatial resolution of $\sim$5" and largest angular scales of $\sim$29" to characterize the gas emission detected in the ODISEA sample. The main goal of this proposal is **to confirm and characterize the gas emission we detected using ALMA archival observations that is associated with molecular outflows and envelopes**. The ACA angular resolution and sensitivity are perfectly suited to complete the objectives of this proposal in a large sample of sources and in a homogeneous way investing a reasonable amount of time. At the distance of Ophiuchus molecular cloud (140 pc), the proposed observations allow to study outflow interaction at envelope scales (hundreds AU - thousands AU). For that we propose to set up the ACA correlator to observe the ^{12}CO (2-1), ^{13}CO (2-1), and C^{18}O (2-1) molecular transitions as primary goal. We also include DCN (3-2) and H$_2$CO lines in our spectral set

up as complimentary secondary goals. The main objectives of the proposal are:

- **A characterization the morphology of the newly detected outflows**: We will measure the cavity opening angle and the extend of the outflow. For that we will use the CO (2-1) transition, which is known to be a sensitive tracer of high velocity outflows (Hartigan et al., 2000). We will compare these morphological characteristics with the different stages of evolution (SED classes) of the driving sources to infer evolutionary trends. Based on the first analysis from ALMA archival, data we expect to most of the outflows will fit within the ACA field of view of $\sim$46". If any outflow is larger than the ACA primary beam, we will infer upper limits and those sources will followed up either with a future ACA mosaic, or ACA+TP observations, or using the Atacama Pathfinder Experiment (APEX) antenna to map the whole extension of the outflow, as needed.

- **Extract dynamical properties of the outflows and correlate them with source properties**: Using CO(2-1) line we will calculate mass, angular momentum, and force of the outflows. ^{13}CO(2-1) line will be used to apply opacity corrections in the line wings of the outflows (e.g. Dunham et al., 2014c; Ruíz-Rodríguez et al., 2017). The less abundant, optically thinner C^{18}O(2-1) will be used to trace the denser envelope material. The mechanical force of the outflows is a key parameter that measures the outflow strength and the rate at which momentum is injected into the envelope by the outflow. We will then search for correlations between the outflow force and the bolometric luminosity of the protostar (which indicates a single mechanism is responsible for driving the outflow studied by Cabrit and Bertout, 1992) and with the envelope mass

to check if the outflow activity declines towards the later stages of the accretion phase, as suggested in the literature (Bontemps et al., 1996).

- **Study episodic ejects and changes in outflow direction.** Episodicity is of great interest since it is invoked in addressing the protostellar luminosity problem. We will search for clumpy or knot-like structures along the outflow (as a sign of episodic ejects) versus a smooth distribution. This will reveal the accretion history of the sample as episodic or continuous. Changes observed in the ejection direction could be produced by variations in the angular momentum of the episodically accreting gas (if drastic changes in the ejection direction) or close binaries interaction (Okoda et al., 2021). The sample size will allow us to look at these phenomena from a statistical perspective.

- **Probe physical conditions on the outflow-envelope interaction regions using H_2CO and DCN:** The main goal of this proposal is to detect the three CO isotopologues proposed, but taking profit on the ALMA correlator capabilities we plan to include transitions of H_2CO and DCN in our spectral setup without the need for additional observing time. **Formaldehyde** (H_2CO) is an ubiquitous complex organic molecule in molecular clouds. It is produced in the surface of dust grains through CO hydrogenation, and shocks and UV heating are responsible for its sublimation (Woon, 2002). In the proposed spectral setup, we can simultaneously tune the three para-H_2CO transition at $\sim 218\,\mathrm{GHz}$ (3_{03}–2_{02}, 3_{22}–2_{21}, and 3_{21}–2_{20}). Since collisions govern the relative populations of the Ka ladders of the H_2CO, the selected H_2CO lines are good tracers of the kinetic temperature around protostars (Mangum and Wootten, 1993), especially in the regime of 50-200 K. In low mass stars H_2CO has been observed in regions where the outflow interacts with the envelope (Schöier et al., 2004). **DCN (J = 3-2 multiplet)** traces higher density gas

than $C^{18}O$ and it is useful to probe the envelope of embedded proto-stars. It also traces the influence of molecular outflows on the circum-stellar envelope (Buckle and Fuller, 2002).

Therefore both additional molecular species are a good complement for the studies proposed here and probe the temperature and density structure of the regions where the outflow interacts with the envelope. We will use the AUTOFIT of the MACUBA software (https://cab.inta-csic.es/madcuba/) to derive the physical parameters of the molecular species (column density, excitation temperature, velocity and linewidths).

These data will provide an homogeneous characterization of new molecular outflows in Ophiuchus cloud associated mostly to Class I and Flat Spectrum sources, and an homogeneous measurement of their morphological and kinematics properties at envelope scales.

A.3 Description of observations

Analogous to the archival data, we request band 6 ACA observations for ^{12}CO, ^{13}CO and $C^{18}O$ (2-1) transitions at 230.580, 219.560 and 220.398 GHz respectively with a bandwith of ~ 150 km s^{-1} enough to detect the highest velocity features of the outflows, and a velocity resolution ~ 0.1 km s^{-1} to map in detail its kinematics. We plan to smooth channels to 0.2 km s^{-1} to increase the signal-to-noise ratio if needed. As a secondary goal and at no further time expenses H_2CO and DCN (3-2) lines will be included in the spectral setup. We request an rms of 50 mJy (over a channel width of 0.2 km s^{-1}), which is twice better the sensitivity Vazzano et al. (2021) used to successfully map with ACA young outflows in Lupus molecular clouds. We want to go deeper in sensitivity because our sample contains more evolved protostars (class I and flat spectrum sources), where it is expected less powerful fainter
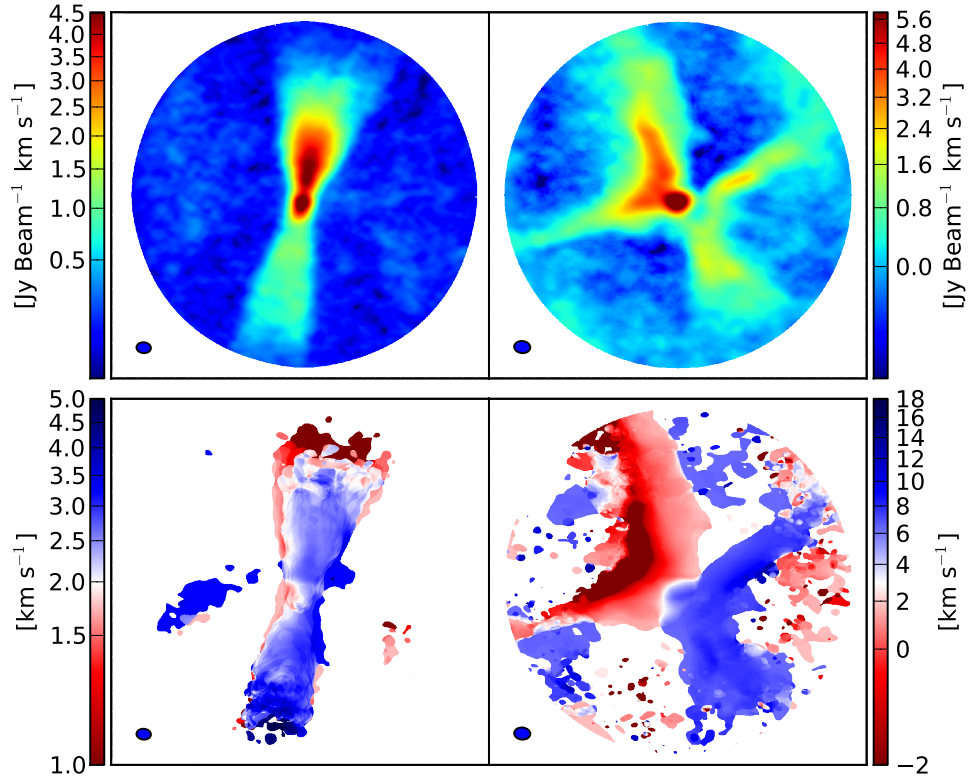
FIGURE A.1: *Top panels: Moment 0 maps for two bipolar outflows in ^{12}CO. Bottom pannels: Moment 1 maps for the same sources and line, using >5×rms emission. In bottom left corner of each panel, it is the beam size, corresponding to 1.1″, or ∼155 au for the Ophiuchus molecular cloud. This data was obtained from 2016.1.00545.S project.*

outflows than for Class 0 sources. The archival data which are the basis of this proposal, have 1.1″ angular resolution, an rms ∼ 30 mJy beam^{-1} with 0.25 km s^{-1} channel width, and Maximum Recoverable Scales of 9.8″ (1400 au). With the ACA observations we will be able to map structures larger than the FoV on the mentioned archival data.

Bibliography

Adams, Fred C., Charles J. Lada, and Frank H. Shu (Jan. 1987). "Spectral Evolution of Young Stellar Objects". In: 312, p. 788. DOI: 10.1086/164924.

Alibert, Y. et al. (Apr. 2005). "Models of giant planet formation with migration and disc evolution". In: 434.1, pp. 343–353. DOI: 10.1051/0004-6361:20042032. arXiv: astro-ph/0412444 [astro-ph].

Allard, F., D. Homeier, and B. Freytag (June 2012). "Models of very-low-mass stars, brown dwarfs and exoplanets". In: *Philosophical Transactions of the Royal Society of London Series A* 370.1968, pp. 2765–2777. DOI: 10.1098/rsta.2011.0269. arXiv: 1112.3591 [astro-ph.SR].

Allen, L. et al. (Jan. 2007). "The Structure and Evolution of Young Stellar Clusters". In: *Protostars and Planets V*. Ed. by Bo Reipurth, David Jewitt, and Klaus Keil, p. 361. DOI: 10.48550/arXiv.astro-ph/0603096. arXiv: astro-ph/0603096 [astro-ph].

ALMA Partnership et al. (July 2015). "The 2014 ALMA Long Baseline Campaign: First Results from High Angular Resolution Observations toward the HL Tau Region". In: 808.1, L3, p. L3. DOI: 10.1088/2041-8205/808/1/L3. arXiv: 1503.02649 [astro-ph.SR].

Alves, J., M. Lombardi, and C. J. Lada (Jan. 2007). "The mass function of dense molecular cores and the origin of the IMF". In: 462.1, pp. L17–L21. DOI: 10.1051/0004-6361:20066389. arXiv: astro-ph/0612126 [astro-ph].

Alves de Oliveira, C. et al. (Mar. 2012). "Spectroscopy of new brown dwarf members of ρ Ophiuchi and an updated initial mass function". In: 539,

A151, A151. DOI: 10.1051/0004-6361/201118230. arXiv: 1201.1912 [astro-ph.GA].

André, Ph. et al. (Sept. 2007). "The initial conditions of star formation in the Ophiuchus main cloud: Kinematics of the protocluster condensations". In: 472.2, pp. 519–535. DOI: 10.1051/0004-6361:20077422. arXiv: 0706.1535 [astro-ph].

André, Ph. et al. (July 2010). "From filamentary clouds to prestellar cores to the stellar IMF: Initial highlights from the Herschel Gould Belt Survey". In: 518, L102, p. L102. DOI: 10.1051/0004-6361/201014666. arXiv: 1005.2618 [astro-ph.GA].

Andre, Philippe, Derek Ward-Thompson, and Mary Barsony (Mar. 1993). "Submillimeter Continuum Observations of rho Ophiuchi A: The Candidate Protostar VLA 1623 and Prestellar Clumps". In: 406, p. 122. DOI: 10.1086/172425.

Andrews, Sean M. et al. (July 2013). "The Mass Dependence between Protoplanetary Disks and their Stellar Hosts". In: 771.2, 129, p. 129. DOI: 10.1088/0004-637X/771/2/129. arXiv: 1305.5262 [astro-ph.SR].

Andrews, Sean M. et al. (Apr. 2016). "Ringed Substructure and a Gap at 1 au in the Nearest Protoplanetary Disk". In: 820.2, L40, p. L40. DOI: 10.3847/2041-8205/820/2/L40. arXiv: 1603.09352 [astro-ph.EP].

Andrews, Sean M. et al. (Dec. 2018). "The Disk Substructures at High Angular Resolution Project (DSHARP). I. Motivation, Sample, Calibration, and Overview". In: 869.2, L41, p. L41. DOI: 10.3847/2041-8213/aaf741. arXiv: 1812.04040 [astro-ph.SR].

Ansdell, M. et al. (Sept. 2016). "ALMA Survey of Lupus Protoplanetary Disks. I. Dust and Gas Masses". In: 828.1, 46, p. 46. DOI: 10.3847/0004-637X/828/1/46. arXiv: 1604.05719 [astro-ph.EP].

Ansdell, M. et al. (May 2017). "An ALMA Survey of Protoplanetary Disks in the σ Orionis Cluster". In: 153.5, 240, p. 240. DOI: 10.3847/1538-3881/aa69c0. arXiv: 1703.08546 [astro-ph.EP].

Antilen, Juanita et al. (June 2023). "Gas distribution in ODISEA sources from ALMA long-baseline observations in ^{12}CO(2-1)". In: 522.2, pp. 2611–2627. DOI: 10.1093/mnras/stad975. arXiv: 2304.15002 [astro-ph.EP].

Antoniucci, S. et al. (Feb. 2014). "On the Mid-infrared Variability of Candidate Eruptive Variables (EXors): A Comparison between Spitzer and WISE Data". In: 782.1, 51, p. 51. DOI: 10.1088/0004-637X/782/1/51. arXiv: 1401.1970 [astro-ph.SR].

Arce, H. G. et al. (Jan. 2007). "Molecular Outflows in Low- and High-Mass Star-forming Regions". In: *Protostars and Planets V*. Ed. by Bo Reipurth, David Jewitt, and Klaus Keil, p. 245. DOI: 10.48550/arXiv.astro-ph/0603071. arXiv: astro-ph/0603071 [astro-ph].

Arce, Héctor G. and Anneila I. Sargent (Aug. 2006). "The Evolution of Outflow-Envelope Interactions in Low-Mass Protostars". In: 646.2, pp. 1070–1085. DOI: 10.1086/505104. arXiv: astro-ph/0605139 [astro-ph].

Avedisova, V. S. (Mar. 2002). "A Catalog of Star-Forming Regions in the Galaxy". In: *Astronomy Reports* 46.3, pp. 193–205. DOI: 10.1134/1.1463097.

Bae, Jaehan, Zhaohuan Zhu, and Lee Hartmann (Dec. 2017). "On the Formation of Multiple Concentric Rings and Gaps in Protoplanetary Disks". In: 850.2, 201, p. 201. DOI: 10.3847/1538-4357/aa9705. arXiv: 1706.03066 [astro-ph.EP].

Bally, J., B. Reipurth, and C. J. Davis (Jan. 2007). "Observations of Jets and Outflows from Young Stars". In: *Protostars and Planets V*. Ed. by Bo Reipurth, David Jewitt, and Klaus Keil, p. 215.

Bally, John (Sept. 2016). "Protostellar Outflows". In: 54, pp. 491–528. DOI: 10.1146/annurev-astro-081915-023341.

Barenfeld, Scott A. et al. (Aug. 2016). "ALMA Observations of Circumstellar Disks in the Upper Scorpius OB Association". In: 827.2, 142, p. 142. DOI: 10.3847/0004-637X/827/2/142. arXiv: 1605.05772 [astro-ph.EP].

Barenfeld, Scott A. et al. (Dec. 2017). "Measurement of Circumstellar Disk Sizes in the Upper Scorpius OB Association with ALMA". In: 851.2, 85, p. 85. DOI: 10.3847/1538-4357/aa989d. arXiv: 1711.04045 [astro-ph.SR].

Beamín, J. C. et al. (Oct. 2014). "Temperature constraints on the coldest brown dwarf known: WISE 0855-0714". In: 570, L8, p. L8. DOI: 10.1051/0004-6361/201424505. arXiv: 1408.5424 [astro-ph.SR].

Benisty, Myriam et al. (July 2021). "A Circumplanetary Disk around PDS70c". In: 916.1, L2, p. L2. DOI: 10.3847/2041-8213/ac0f83. arXiv: 2108.07123 [astro-ph.EP].

Bi, Jiaqing, Min-Kai Lin, and Ruobing Dong (May 2021). "Puffed-up Edges of Planet-opened Gaps in Protoplanetary Disks. I. Hydrodynamic Simulations". In: 912.2, 107, p. 107. DOI: 10.3847/1538-4357/abef6b. arXiv: 2103.09254 [astro-ph.EP].

Birnstiel, T. et al. (June 2010). "Testing the theory of grain growth and fragmentation by millimeter observations of protoplanetary disks". In: 516, L14, p. L14. DOI: 10.1051/0004-6361/201014893. arXiv: 1006.0940 [astro-ph.SR].

Blum, Jürgen and Gerhard Wurm (Jan. 2000). "Experiments on Sticking, Restructuring, and Fragmentation of Preplanetary Dust Aggregates". In: 143.1, pp. 138–146. DOI: 10.1006/icar.1999.6234.

Bohlin, R. C., B. D. Savage, and J. F. Drake (Aug. 1978). "A survey of interstellar H I from Lalpha absorption measurements. II." In: 224, pp. 132–142. DOI: 10.1086/156357.

Bontemps, S. et al. (July 1996). "Evolution of outflow activity around low-mass embedded young stellar objects". In: 311, pp. 858–872.

Boss, A. P. (Jan. 1997). "Giant planet formation by gravitational instability." In: *Science* 276, pp. 1836–1839. DOI: 10.1126/science.276.5320.1836.

Bowler, Brendan P. and Lynne A. Hillenbrand (Oct. 2015). "Near-infrared Spectroscopy of 2M0441+2301 AabBab: A Quadruple System Spanning the Stellar to Planetary Mass Regimes". In: 811.2, L30, p. L30. DOI: 10.1088/2041-8205/811/2/L30. arXiv: 1509.01658 [astro-ph.EP].

Brauer, F., C. P. Dullemond, and Th. Henning (Mar. 2008). "Coagulation, fragmentation and radial motion of solid particles in protoplanetary disks". In: 480.3, pp. 859–877. DOI: 10.1051/0004-6361:20077759. arXiv: 0711.2192 [astro-ph].

Buckle, J. V. and G. A. Fuller (Jan. 2002). "The interaction between protostars and their environment: Carbon-bearing species towards low mass protostars". In: 381, pp. 77–97. DOI: 10.1051/0004-6361:20011300.

Bussmann, R. S. et al. (Mar. 2007). "A CO (J=3-2) Outflow Survey of the Elias 29 Region". In: 657.1, pp. L33–L36. DOI: 10.1086/513101. arXiv: astro-ph/0702745 [astro-ph].

Cabrit, Sylvie and Claude Bertout (July 1992). "CO line formation in bipolar flows. III. The energetics of molecular flows and ionized winds." In: 261, pp. 274–284.

Calcino, Josh et al. (Dec. 2019). "Signatures of an eccentric disc cavity: Dust and gas in IRS 48". In: 490.2, pp. 2579–2587. DOI: 10.1093/mnras/stz2770. arXiv: 1910.00161 [astro-ph.EP].

Calvet, N. et al. (Sept. 2005). "Disks in Transition in the Taurus Population: Spitzer IRS Spectra of GM Aurigae and DM Tauri". In: 630.2, pp. L185–L188. DOI: 10.1086/491652.

Canovas, H. et al. (May 2016). "A ring-like concentration of mm-sized particles in Sz 91". In: 458.1, pp. L29–L33. DOI: 10.1093/mnrasl/slw006. arXiv: 1601.06801 [astro-ph.SR].

Casassus, Simon (Apr. 2016). "Resolved Observations of Transition Disks".
    In: 33, e013, e013. DOI: 10.1017/pasa.2016.7. arXiv: 1602.06523 [astro-ph.SR].

Casassus, Simon et al. (Jan. 2013). "Flows of gas through a protoplanetary
    gap". In: 493.7431, pp. 191–194. DOI: 10.1038/nature11769. arXiv: 1305.6062 [astro-ph.GA].

Casassus, Simon et al. (Oct. 2015). "A Compact Concentration of Large Grains
    in the HD 142527 Protoplanetary Dust Trap". In: 812.2, 126, p. 126. DOI:
    10.1088/0004-637X/812/2/126. arXiv: 1505.07743 [astro-ph.SR].

Casassus, Simon et al. (Nov. 2023). "Azimuthal temperature variations in
    ISO-Oph 2 from multifrequency ALMA observations". In: 526.1, pp. 1545–
    1558. DOI: 10.1093/mnras/stad1981. arXiv: 2307.07416 [astro-ph.EP].

Cazzoletti, P. et al. (Nov. 2018). "Evidence for a massive dust-trapping vor-
    tex connected to spirals. Multi-wavelength analysis of the HD 135344B
    protoplanetary disk". In: 619, A161, A161. DOI: 10.1051/0004-6361/
    201834006. arXiv: 1809.04160 [astro-ph.EP].

Chauvin, G. et al. (Aug. 2005). "A companion to AB Pic at the planet/brown
    dwarf boundary". In: 438.3, pp. L29–L32. DOI: 10.1051/0004-6361:
    200500111. arXiv: astro-ph/0504658 [astro-ph].

Cheng, Yu et al. (July 2022). "Disks and Outflows in the Intermediate-mass
    Star-forming Region NGC 2071 IR". In: 933.2, 178, p. 178. DOI: 10.3847/
    1538-4357/ac7464. arXiv: 2205.15108 [astro-ph.GA].

Cieza, Lucas A. et al. (May 2009). "Primordial Circumstellar Disks in Binary
    Systems: Evidence for Reduced Lifetimes". In: 696.1, pp. L84–L88. DOI:
    10.1088/0004-637X/696/1/L84. arXiv: 0903.3057 [astro-ph.SR].

Cieza, Lucas A. et al. (Apr. 2010). "The Nature of Transition Circumstellar
    Disks. I. The Ophiuchus Molecular Cloud". In: 712.2, pp. 925–941. DOI:
    10.1088/0004-637X/712/2/925. arXiv: 1001.4825 [astro-ph.GA].

Cieza, Lucas A. et al. (July 2016). "Imaging the water snow-line during a pro-tostellar outburst". In: 535.7611, pp. 258–261. DOI: 10.1038/nature18612. arXiv: 1607.03757 [astro-ph.SR].

Cieza, Lucas A. et al. (Jan. 2019). "The Ophiuchus DIsc Survey Employing ALMA (ODISEA) - I: project description and continuum images at 28 au resolution". In: 482.1, pp. 698–714. DOI: 10.1093/mnras/sty2653. arXiv: 1809.08844 [astro-ph.EP].

Cieza, Lucas A. et al. (Feb. 2021). "The Ophiuchus DIsc Survey Employing ALMA (ODISEA) - III. The evolution of substructures in massive discs at 3-5 au resolution". In: 501.2, pp. 2934–2953. DOI: 10.1093/mnras/staa3787. arXiv: 2012.00189 [astro-ph.EP].

Cox, Erin G. et al. (Dec. 2017). "Protoplanetary Disks in ρ Ophiuchus as Seen from ALMA". In: 851.2, 83, p. 83. DOI: 10.3847/1538-4357/aa97e2. arXiv: 1711.03974 [astro-ph.SR].

Crida, A. and B. Bitsch (Mar. 2017). "Runaway gas accretion and gap opening versus type I migration". In: 285, pp. 145–154. DOI: 10.1016/j.icarus.2016.10.017. arXiv: 1610.05403 [astro-ph.EP].

Crida, A., A. Morbidelli, and F. Masset (Apr. 2006). "On the width and shape of gaps in protoplanetary disks". In: 181.2, pp. 587–604. DOI: 10.1016/j.icarus.2005.10.007. arXiv: astro-ph/0511082 [astro-ph].

Cuello, Nicolás et al. (Jan. 2020). "Flybys in protoplanetary discs - II. Observational signatures". In: 491.1, pp. 504–514. DOI: 10.1093/mnras/stz2938. arXiv: 1910.06822 [astro-ph.EP].

Curtis, Emily I. et al. (Nov. 2010). "A submillimetre survey of the kinematics of the Perseus molecular cloud - II. Molecular outflows". In: 408.3, pp. 1516–1539. DOI: 10.1111/j.1365-2966.2010.17214.x. arXiv: 1006.3218 [astro-ph.GA].

Cutri, R. M. et al. (2003). *2MASS All Sky Catalog of point sources.*

Dai, Fei et al. (May 2015). "A tidal encounter caught in the act: modelling a star-disc fly-by in the young RW Aurigae system". In: 449.2, pp. 1996–2009. DOI: 10.1093/mnras/stv403. arXiv: 1502.06649 [astro-ph.SR].

D'Alessio, Paola et al. (Feb. 2006). "Effects of Dust Growth and Settling in T Tauri Disks". In: 638.1, pp. 314–335. DOI: 10.1086/498861. arXiv: astro-ph/0511564 [astro-ph].

Delage, Timmy N. et al. (June 2023). "The impact of dust evolution on the dead zone outer edge in magnetized protoplanetary disks". In: 674, A190, A190. DOI: 10.1051/0004-6361/202244731. arXiv: 2303.15675 [astro-ph.EP].

Dong, Ruobing et al. (July 2017). "Multiple Disk Gaps and Rings Generated by a Single Super-Earth". In: 843.2, 127, p. 127. DOI: 10.3847/1538-4357/aa72f2. arXiv: 1705.04687 [astro-ph.EP].

Dong, Ruobing et al. (June 2018). "The Eccentric Cavity, Triple Rings, Two-armed Spirals, and Double Clumps of the MWC 758 Disk". In: 860.2, 124, p. 124. DOI: 10.3847/1538-4357/aac6cb. arXiv: 1805.12141 [astro-ph.SR].

Doppmann, G. W. et al. (Sept. 2005). "The Physical Natures of Class I and Flat-Spectrum Protostellar Photospheres: A Near-Infrared Spectroscopic Study". In: 130.3, pp. 1145–1170. DOI: 10.1086/431954. arXiv: astro-ph/0505295 [astro-ph].

Dunham, M. M. et al. (Jan. 2014a). "The Evolution of Protostars: Insights from Ten Years of Infrared Surveys with Spitzer and Herschel". In: *Protostars and Planets VI*. Ed. by Henrik Beuther et al., pp. 195–218. DOI: 10.2458/azu_uapress_9780816531240-ch009. arXiv: 1401.1809 [astro-ph.GA].

Dunham, Michael M. et al. (Mar. 2014b). "Molecular Outflows Driven by Low-mass Protostars. I. Correcting for Underestimates When Measuring Outflow Masses and Dynamical Properties". In: 783.1, 29, p. 29. DOI: 10.1088/0004-637X/783/1/29. arXiv: 1401.2391 [astro-ph.GA].

— (Mar. 2014c). "Molecular Outflows Driven by Low-mass Protostars. I. Correcting for Underestimates When Measuring Outflow Masses and Dynamical Properties". In: 783.1, 29, p. 29. DOI: 10.1088/0004-637X/783/1/29. arXiv: 1401.2391 [astro-ph.GA].

Durisen, R. H. et al. (Jan. 2007). "Gravitational Instabilities in Gaseous Protoplanetary Disks and Implications for Giant Planet Formation". In: *Protostars and Planets V*. Ed. by Bo Reipurth, David Jewitt, and Klaus Keil, p. 607. DOI: 10.48550/arXiv.astro-ph/0603179. arXiv: astro-ph/0603179 [astro-ph].

Esplin, T. L. and K. L. Luhman (June 2020). "A Survey for New Stars and Brown Dwarfs in the Ophiuchus Star-forming Complex". In: 159.6, 282, p. 282. DOI: 10.3847/1538-3881/ab8dbd. arXiv: 2005.10096 [astro-ph.SR].

Evans Neal J., II et al. (Apr. 2009). "The Spitzer c2d Legacy Results: Star-Formation Rates and Efficiencies; Evolution and Lifetimes". In: 181.2, pp. 321–350. DOI: 10.1088/0067-0049/181/2/321. arXiv: 0811.1059 [astro-ph].

Francis, Logan and Nienke van der Marel (Apr. 2020). "Dust-depleted Inner Disks in a Large Sample of Transition Disks through Long-baseline ALMA Observations". In: 892.2, 111, p. 111. DOI: 10.3847/1538-4357/ab7b63. arXiv: 2003.00079 [astro-ph.EP].

Frank, A. et al. (Jan. 2014). "Jets and Outflows from Star to Cloud: Observations Confront Theory". In: *Protostars and Planets VI*. Ed. by Henrik Beuther et al., pp. 451–474. DOI: 10.2458/azu_uapress_9780816531240-ch020. arXiv: 1402.3553 [astro-ph.SR].

Gaia Collaboration et al. (Aug. 2018). "Gaia Data Release 2. Summary of the contents and survey properties". In: 616, A1, A1. DOI: 10.1051/0004-6361/201833051. arXiv: 1804.09365 [astro-ph.GA].

Garufi, A. et al. (Feb. 2022). "ALMA chemical survey of disk-outflow sources in Taurus (ALMA-DOT). VI. Accretion shocks in the disk of DG Tau and

HL Tau". In: 658, A104, A104. DOI: 10.1051/0004-6361/202141264. arXiv: 2110.13820 [astro-ph.GA].

Gatti, T. et al. (Dec. 2006). "Accretion in ρ Ophiuchus brown dwarfs: infrared hydrogen line ratios". In: 460.2, pp. 547–553. DOI: 10.1051/0004-6361: 20066095. arXiv: astro-ph/0609291 [astro-ph].

Geers, Vincent et al. (Jan. 2011). "Substellar Objects in Nearby Young Clusters (SONYC). II. The Brown Dwarf Population of ρ Ophiuchi". In: 726.1, 23, p. 23. DOI: 10.1088/0004-637X/726/1/23. arXiv: 1010.5801 [astro-ph.SR].

Gonzales, Erica J. et al. (Apr. 2020). "The TRENDS High-contrast Imaging Survey. VIII. Compendium of Benchmark Objects". In: 893.1, 27, p. 27. DOI: 10.3847/1538-4357/ab71fb.

González-Ruilova, Camilo et al. (Oct. 2020). "A Tale of Two Transition Disks: ALMA Long-baseline Observations of ISO-Oph 2 Reveal Two Closely Packed Nonaxisymmetric Rings and a ∼2 au Cavity". In: 902.2, L33, p. L33. DOI: 10.3847/2041-8213/abbcce. arXiv: 2010.03650 [astro-ph.EP].

Goodman, J. and R. R. Rafikov (May 2001). "Planetary Torques as the Viscosity of Protoplanetary Disks". In: 552.2, pp. 793–802. DOI: 10.1086/320572. arXiv: astro-ph/0010576 [astro-ph].

Greene, Thomas P. et al. (Oct. 1994). "Further Mid-Infrared Study of the rho Ophiuchi Cloud Young Stellar Population: Luminosities and Masses of Pre–Main-Sequence Stars". In: 434, p. 614. DOI: 10.1086/174763.

Guidi, G. et al. (Apr. 2016). "Dust properties across the CO snowline in the HD 163296 disk from ALMA and VLA observations". In: 588, A112, A112. DOI: 10.1051/0004-6361/201527516. arXiv: 1601.07542 [astro-ph.SR].

Gundlach, B. and J. Blum (Jan. 2015). "The Stickiness of Micrometer-sized Water-ice Particles". In: 798.1, 34, p. 34. DOI: 10.1088/0004-637X/798/1/ 34. arXiv: 1410.7199 [astro-ph.EP].

Gupta, A. et al. (Feb. 2023). "Reflections on nebulae around young stars. A systematic search for late-stage infall of material onto Class II disks". In:

670, L8, p. L8. DOI: 10.1051/0004-6361/202245254. arXiv: 2301.02994 [astro-ph.SR].

Gupta, Aashish et al. (Jan. 2024). "TIPSY: Trajectory of Infalling Particles in Streamers around Young stars. Dynamical analysis of the streamers around S CrA and HL Tau". In: *arXiv e-prints*, arXiv:2401.10403, arXiv:2401.10403. DOI: 10.48550/arXiv.2401.10403. arXiv: 2401.10403 [astro-ph.SR].

Gutermuth, R. A. et al. (Sept. 2009). "A Spitzer Survey of Young Stellar Clusters Within One Kiloparsec of the Sun: Cluster Core Extraction and Basic Structural Analysis". In: 184.1, pp. 18–83. DOI: 10.1088/0067-0049/184/1/18. arXiv: 0906.0201 [astro-ph.SR].

Güttler, C. et al. (Apr. 2010). "The outcome of protoplanetary dust growth: pebbles, boulders, or planetesimals?. I. Mapping the zoo of laboratory collision experiments". In: 513, A56, A56. DOI: 10.1051/0004-6361/200912852. arXiv: 0910.4251 [astro-ph.EP].

Habel, Nolan M. et al. (Apr. 2021). "An HST Survey of Protostellar Outflow Cavities: Does Feedback Clear Envelopes?" In: 911.2, 153, p. 153. DOI: 10.3847/1538-4357/abded8. arXiv: 2102.06717 [astro-ph.GA].

Hales, Antonio S. et al. (Sept. 2020). "ALMA Observations of Young Eruptive Stars: Continuum Disk Sizes and Molecular Outflows". In: 900.1, 7, p. 7. DOI: 10.3847/1538-4357/aba3c4. arXiv: 2007.04348 [astro-ph.SR].

Hammer, Michael et al. (Jan. 2019). "Observational diagnostics of elongated planet-induced vortices with realistic planet formation time-scales". In: 482.3, pp. 3609–3621. DOI: 10.1093/mnras/sty2946. arXiv: 1809.07391 [astro-ph.EP].

Haro, Guillermo (May 1952). "Herbig's Nebulous Objects Near NGC 1999." In: 115, p. 572. DOI: 10.1086/145576.

Harsono, D. et al. (Feb. 2014). "Rotationally-supported disks around Class I sources in Taurus: disk formation constraints". In: 562, A77, A77. DOI: 10.1051/0004-6361/201322646. arXiv: 1312.5716 [astro-ph.GA].

Hartigan, Patrick et al. (Apr. 2000). "Kinematics of Herbig-Haro Objects in
the Protostellar Outflow L1551 as Mapped by Fabry-Perot Spectroscopy".
In: 119.4, pp. 1872–1880. DOI: 10.1086/301295.

Hartmann, Lee, Gregory Herczeg, and Nuria Calvet (Sept. 2016). "Accre-
tion onto Pre-Main-Sequence Stars". In: 54, pp. 135–180. DOI: 10.1146/
annurev-astro-081915-023347.

Hasegawa, Yasuhiro et al. (Feb. 2022). "Determining Dispersal Mechanisms
of Protoplanetary Disks Using Accretion and Wind Mass Loss Rates". In:
926.2, L23, p. L23. DOI: 10.3847/2041-8213/ac50aa. arXiv: 2112.02831
[astro-ph.EP].

Hendler, Nathanial P. et al. (Mar. 2018). "A likely planet-induced gap in the
disc around T Cha". In: 475.1, pp. L62–L66. DOI: 10.1093/mnrasl/slx184.

Herbig, G. H. (Sept. 1989). "FU Orionis eruptions." In: *European Southern Ob-
servatory Conference and Workshop Proceedings*. Vol. 33. European Southern
Observatory Conference and Workshop Proceedings, pp. 233–246.

Herbig, George H. (May 1951). "The Spectra of Two Nebulous Objects Near
NGC 1999." In: 113, pp. 697–699. DOI: 10.1086/145440.

Hirano, Shingo and Naoki Yoshida (Jan. 2013). "Radiative Cooling Imple-
mentations in Simulations of Primordial Star Formation". In: 763.1, 52,
p. 52. DOI: 10.1088/0004-637X/763/1/52. arXiv: 1211.6855 [astro-ph.CO].

Hsieh, Cheng-Han et al. (Apr. 2023). "The Evolution of Protostellar Outflow
Cavities, Kinematics, and Angular Distribution of Momentum and En-
ergy in Orion A: Evidence for Dynamical Cores". In: 947.1, 25, p. 25. DOI:
10.3847/1538-4357/acba13. arXiv: 2302.03174 [astro-ph.SR].

Hsieh, Tien-Hao, Shih-Ping Lai, and Arnaud Belloche (Apr. 2017). "Widening
of Protostellar Outflows: An Infrared Outflow Survey in Low-luminosity
Objects". In: 153.4, 173, p. 173. DOI: 10.3847/1538-3881/aa5ff8. arXiv:
1702.02732 [astro-ph.GA].

Huang, Jane et al. (Dec. 2018a). "The Disk Substructures at High Angular Resolution Project (DSHARP). II. Characteristics of Annular Substructures". In: 869.2, L42, p. L42. DOI: 10.3847/2041-8213/aaf740. arXiv: 1812.04041 [astro-ph.EP].

Huang, Jane et al. (Dec. 2018b). "The Disk Substructures at High Angular Resolution Project (DSHARP). III. Spiral Structures in the Millimeter Continuum of the Elias 27, IM Lup, and WaOph 6 Disks". In: 869.2, L43, p. L43. DOI: 10.3847/2041-8213/aaf7a0. arXiv: 1812.04193 [astro-ph.SR].

Huang, Jane et al. (Feb. 2023). "Molecular Mapping of DR Tau's Protoplanetary Disk, Envelope, Outflow, and Large-scale Spiral Arm". In: 943.2, 107, p. 107. DOI: 10.3847/1538-4357/aca89c. arXiv: 2301.02674 [astro-ph.SR].

Hughes, A. M. et al. (July 2007). "An Inner Hole in the Disk around TW Hydrae Resolved in 7 mm Dust Emission". In: 664.1, pp. 536–542. DOI: 10.1086/518885. arXiv: 0704.2422 [astro-ph].

Hughes, A. Meredith, Gaspard Duchêne, and Brenda C. Matthews (Sept. 2018). "Debris Disks: Structure, Composition, and Variability". In: 56, pp. 541–591. DOI: 10.1146/annurev-astro-081817-052035. arXiv: 1802.04313 [astro-ph.EP].

Ikoma, Masahiro, Kiyoshi Nakazawa, and Hiroyuki Emori (July 2000). "Formation of Giant Planets: Dependences on Core Accretion Rate and Grain Opacity". In: 537.2, pp. 1013–1025. DOI: 10.1086/309050.

Kenyon, Scott J. et al. (Mar. 1990). "An IRAS Survey of the Taurus-Auriga Molecular Cloud". In: 99, p. 869. DOI: 10.1086/115380.

Keppler, M. et al. (Sept. 2018). "Discovery of a planetary-mass companion within the gap of the transition disk around PDS 70". In: 617, A44, A44. DOI: 10.1051/0004-6361/201832957. arXiv: 1806.11568 [astro-ph.EP].

Khanzadyan, T. et al. (Oct. 2004). "An unbiased search for the signatures of protostars in the ρ Ophiuchi A molecular cloud. I. Near-infrared observations". In: 426, pp. 171–183. DOI: 10.1051/0004-6361:20041241.

Krijt, S. et al. (Feb. 2015). "Erosion and the limits to planetesimal growth". In: 574, A83, A83. DOI: 10.1051/0004-6361/201425222. arXiv: 1412.3593 [astro-ph.EP].

Kumar, Shiv S. (May 1963). "The Structure of Stars of Very Low Mass." In: 137, p. 1121. DOI: 10.1086/147589.

Kurtovic, Nicolás T. et al. (Dec. 2018). "The Disk Substructures at High Angular Resolution Project (DSHARP). IV. Characterizing Substructures and Interactions in Disks around Multiple Star Systems". In: 869.2, L44, p. L44. DOI: 10.3847/2041-8213/aaf746. arXiv: 1812.04536 [astro-ph.SR].

Kwon, Woojin, Leslie W. Looney, and Lee G. Mundy (Nov. 2011). "Resolving the Circumstellar Disk of HL Tauri at Millimeter Wavelengths". In: 741.1, 3, p. 3. DOI: 10.1088/0004-637X/741/1/3. arXiv: 1107.5275 [astro-ph.SR].

Kwon, Woojin et al. (May 2009). "Grain Growth and Density Distribution of the Youngest Protostellar Systems". In: 696.1, pp. 841–852. DOI: 10.1088/0004-637X/696/1/841. arXiv: 0902.2008 [astro-ph.SR].

Lada, C. J. and B. A. Wilking (Dec. 1984). "The nature of the embedded population in the rho Ophiuchi dark cloud : mid-infrared observations." In: 287, pp. 610–621. DOI: 10.1086/162719.

Lada, Charles J. (Jan. 1987). "Star formation: from OB associations to protostars." In: *Star Forming Regions*. Ed. by Manuel Peimbert and Jun Jugaku. Vol. 115, p. 1.

Ladjelate, B. et al. (June 2020). "The Herschel view of the dense core population in the Ophiuchus molecular cloud". In: 638, A74, A74. DOI: 10.1051/0004-6361/201936442. arXiv: 2001.11036 [astro-ph.GA].

Lambrechts, M. and A. Johansen (Aug. 2012). "Rapid growth of gas-giant cores by pebble accretion". In: 544, A32, A32. DOI: 10.1051/0004-6361/201219127. arXiv: 1205.3030 [astro-ph.EP].

Lay, O. P., J. E. Carlstrom, and R. E. Hills (Nov. 1997). "Constraints on the HL Tauri Protostellar Disk from Millimeter- and Submillimeter-Wave Interferometry". In: 489.2, pp. 917–927. DOI: 10.1086/304815.

Lissauer, Jack J. (Jan. 1993). "Planet formation." In: 31, pp. 129–174. DOI: 10.1146/annurev.aa.31.090193.001021.

Lodato, Giuseppe et al. (Dec. 2017). "Protoplanetary disc 'isochrones' and the evolution of discs in the $\dot{M}$-M_d plane". In: 472.4, pp. 4700–4706. DOI: 10.1093/mnras/stx2273. arXiv: 1708.09467 [astro-ph.SR].

Lombardi, Marco et al. (June 2014). "Herschel-Planck dust optical-depth and column-density maps. I. Method description and results for Orion". In: 566, A45, A45. DOI: 10.1051/0004-6361/201323293. arXiv: 1404.0032 [astro-ph.SR].

Long, Feng et al. (Sept. 2019). "Compact Disks in a High-resolution ALMA Survey of Dust Structures in the Taurus Molecular Cloud". In: 882.1, 49, p. 49. DOI: 10.3847/1538-4357/ab2d2d. arXiv: 1906.10809 [astro-ph.SR].

Machida, Masahiro N. and Takashi Hosokawa (May 2013). "Evolution of protostellar outflow around low-mass protostar". In: 431.2, pp. 1719–1744. DOI: 10.1093/mnras/stt291. arXiv: 1302.4176 [astro-ph.SR].

Machida, Masahiro N., Shu-ichiro Inutsuka, and Tomoaki Matsumoto (July 2009). "First Direct Simulation of Brown Dwarf Formation in a Compact Cloud Core". In: 699.2, pp. L157–L160. DOI: 10.1088/0004-637X/699/2/L157. arXiv: 0907.3255 [astro-ph.SR].

Manara, C. F. et al. (July 2015). "X-Shooter study of accretion in ρ-Ophiucus: very low-mass stars and brown dwarfs". In: 579, A66, A66. DOI: 10.1051/0004-6361/201526169. arXiv: 1505.04046 [astro-ph.SR].

Manara, C. F. et al. (Aug. 2019). "Observational constraints on dust disk sizes in tidally truncated protoplanetary disks in multiple systems in the Taurus region". In: 628, A95, A95. DOI: 10.1051/0004-6361/201935964. arXiv: 1907.03846 [astro-ph.EP].

Mangum, Jeffrey G. and Alwyn Wootten (Nov. 1993). "Formaldehyde as a Probe of Physical Conditions in Dense Molecular Clouds". In: 89, p. 123. DOI: 10.1086/191841.

Maret, S. et al. (Mar. 2020). "Searching for kinematic evidence of Keplerian disks around Class 0 protostars with CALYPSO". In: 635, A15, A15. DOI: 10.1051/0004-6361/201936798. arXiv: 2001.06355 [astro-ph.SR].

Matrà, L. et al. (Apr. 2019). "Kuiper Belt-like Hot and Cold Populations of Planetesimal Inclinations in the β Pictoris Belt Revealed by ALMA". In: 157.4, 135, p. 135. DOI: 10.3847/1538-3881/ab06c0. arXiv: 1902.04081 [astro-ph.EP].

McMullin, J. P. et al. (Oct. 2007). "CASA Architecture and Applications". In: *Astronomical Data Analysis Software and Systems XVI*. Ed. by R. A. Shaw, F. Hill, and D. J. Bell. Vol. 376. Astronomical Society of the Pacific Conference Series, p. 127.

Ménard, F. et al. (July 2020). "Ongoing flyby in the young multiple system UX Tauri". In: 639, L1, p. L1. DOI: 10.1051/0004-6361/202038356. arXiv: 2006.02439 [astro-ph.SR].

Merín, Bruno et al. (Aug. 2010). "A Spitzer c2d Legacy Survey to Identify and Characterize Disks with Inner Dust Holes". In: 718.2, pp. 1200–1223. DOI: 10.1088/0004-637X/718/2/1200. arXiv: 1008.2428 [astro-ph.SR].

Moór, Attila et al. (Nov. 2017). "Molecular Gas in Debris Disks around Young A-type Stars". In: 849.2, 123, p. 123. DOI: 10.3847/1538-4357/aa8e4e. arXiv: 1709.08414 [astro-ph.SR].

Motte, F. et al. (June 2022). "ALMA-IMF. I. Investigating the origin of stellar masses: Introduction to the Large Program and first results". In: 662, A8, A8. DOI: 10.1051/0004-6361/202141677. arXiv: 2112.08182 [astro-ph.GA].

Motte, Frédérique, Sylvain Bontemps, and Fabien Louvet (Sept. 2018). "High-Mass Star and Massive Cluster Formation in the Milky Way". In: 56, pp. 41–

82. DOI: 10.1146/annurev-astro-091916-055235. arXiv: 1706.00118 [astro-ph.GA].

Mottram, J. C. et al. (Oct. 2013). "Waterfalls around protostars. Infall motions towards Class 0/I envelopes as probed by water". In: 558, A126, A126. DOI: 10.1051/0004-6361/201321828. arXiv: 1308.5119 [astro-ph.GA].

Müller, A. et al. (Sept. 2018). "Orbital and atmospheric characterization of the planet within the gap of the PDS 70 transition disk". In: 617, L2, p. L2. DOI: 10.1051/0004-6361/201833584. arXiv: 1806.11567 [astro-ph.EP].

Muro-Arena, G. A. et al. (Apr. 2020). "Spirals inside the millimeter cavity of transition disk SR 21". In: 636, L4, p. L4. DOI: 10.1051/0004-6361/202037656. arXiv: 2003.08189 [astro-ph.EP].

Mužić, Koraljka et al. (Nov. 2017). "The low-mass content of the massive young star cluster RCW 38". In: 471.3, pp. 3699–3712. DOI: 10.1093/mnras/stx1906. arXiv: 1707.00277 [astro-ph.SR].

Myers, P. C. et al. (Aug. 1987). "Near-Infrared and Optical Observations of IRAS Sources in and near Dense Cores". In: 319, p. 340. DOI: 10.1086/165458.

Oberg, N. et al. (Feb. 2023). "Observing circumplanetary disks with METIS". In: 670, A74, A74. DOI: 10.1051/0004-6361/202244845. arXiv: 2212.03007 [astro-ph.EP].

Offner, Stella S. R. and Héctor G. Arce (Mar. 2014). "Investigations of Protostellar Outflow Launching and Gas Entrainment: Hydrodynamic Simulations and Molecular Emission". In: 784.1, 61, p. 61. DOI: 10.1088/0004-637X/784/1/61. arXiv: 1312.0951 [astro-ph.SR].

Ohashi, Nagayoshi et al. (July 2023). "Early Planet Formation in Embedded Disks (eDisk). I. Overview of the Program and First Results". In: 951.1, 8, p. 8. DOI: 10.3847/1538-4357/acd384. arXiv: 2306.15406 [astro-ph.EP].

Ohashi, Satoshi et al. (Mar. 2022). "Misaligned Rotations of the Envelope, Outflow, and Disks in the Multiple Protostellar System of VLA 1623-2417:

FAUST. III". In: 927.1, 54, p. 54. DOI: 10.3847/1538-4357/ac4cae. arXiv: 2201.07334 [astro-ph.GA].

Okoda, Yuki et al. (Mar. 2021). "FAUST. II. Discovery of a Secondary Outflow in IRAS 15398-3359: Variability in Outflow Direction during the Earliest Stage of Star Formation?" In: 910.1, 11, p. 11. DOI: 10.3847/1538-4357/abddb1. arXiv: 2101.07404 [astro-ph.SR].

Ormel, C. W. and H. H. Klahr (Sept. 2010). "The effect of gas drag on the growth of protoplanets. Analytical expressions for the accretion of small bodies in laminar disks". In: 520, A43, A43. DOI: 10.1051/0004-6361/201014903. arXiv: 1007.0916 [astro-ph.EP].

Ortiz-León, Gisela N. et al. (Jan. 2017). "The Gould's Belt Distances Survey (GOBELINS). I. Trigonometric Parallax Distances and Depth of the Ophiuchus Complex". In: 834.2, 141, p. 141. DOI: 10.3847/1538-4357/834/2/141. arXiv: 1611.06466 [astro-ph.SR].

Ortiz-León, Gisela N. et al. (Dec. 2018). "Gaia-DR2 Confirms VLBA Parallaxes in Ophiuchus, Serpens, and Aquila". In: 869.2, L33, p. L33. DOI: 10.3847/2041-8213/aaf6ad. arXiv: 1812.02360 [astro-ph.SR].

Pascucci, I. et al. (Nov. 2016). "A Steeper than Linear Disk Mass-Stellar Mass Scaling Relation". In: 831.2, 125, p. 125. DOI: 10.3847/0004-637X/831/2/125. arXiv: 1608.03621 [astro-ph.EP].

Pascucci, Ilaria et al. (Aug. 2023). "Large Myr-old Disks Are Not Severely Depleted of Gas-phase CO or Carbon". In: 953.2, 183, p. 183. DOI: 10.3847/1538-4357/ace4bf. arXiv: 2307.02704 [astro-ph.SR].

Perez, Sebastian et al. (Sept. 2015). "Planet Formation Signposts: Observability of Circumplanetary Disks via Gas Kinematics". In: 811.1, L5, p. L5. DOI: 10.1088/2041-8205/811/1/L5. arXiv: 1505.06808 [astro-ph.EP].

Pérez, Sebastián et al. (July 2019). "Dust Unveils the Formation of a Mini-Neptune Planet in a Protoplanetary Ring". In: 158.1, 15, p. 15. DOI: 10.3847/1538-3881/ab1f88. arXiv: 1902.05143 [astro-ph.EP].

Pérez, Sebastián et al. (Jan. 2020a). "Long Baseline Observations of the HD 100546 Protoplanetary Disk with ALMA". In: 889.1, L24, p. L24. DOI: 10.3847/2041-8213/ab6b2b. arXiv: 1906.06305 [astro-ph.EP].

Pérez, Sebastián et al. (Jan. 2020b). "Resolving the FU Orionis System with ALMA: Interacting Twin Disks?" In: 889.1, 59, p. 59. DOI: 10.3847/1538-4357/ab5c1b. arXiv: 1911.11282 [astro-ph.EP].

Pineda, J. E. et al. (July 2023). "From Bubbles and Filaments to Cores and Disks: Gas Gathering and Growth of Structure Leading to the Formation of Stellar Systems". In: *Protostars and Planets VII*. Ed. by S. Inutsuka et al. Vol. 534. Astronomical Society of the Pacific Conference Series, p. 233. DOI: 10.48550/arXiv.2205.03935. arXiv: 2205.03935 [astro-ph.GA].

Pineda, Jaime E. et al. (Jan. 2020). "A protostellar system fed by a streamer of 10,500 au length". In: *Nature Astronomy* 4, pp. 1158–1163. DOI: 10.1038/s41550-020-1150-z. arXiv: 2007.13430 [astro-ph.GA].

Pinilla, P. et al. (Feb. 2012). "Trapping dust particles in the outer regions of protoplanetary disks". In: 538, A114, A114. DOI: 10.1051/0004-6361/201118204. arXiv: 1112.2349 [astro-ph.EP].

Pinilla, P. et al. (Jan. 2015). "Gas and dust structures in protoplanetary disks hosting multiple planets". In: 573, A9, A9. DOI: 10.1051/0004-6361/201424679. arXiv: 1410.5963 [astro-ph.EP].

Pinilla, P. et al. (Aug. 2017). "Dust Density Distribution and Imaging Analysis of Different Ice Lines in Protoplanetary Disks". In: 845.1, 68, p. 68. DOI: 10.3847/1538-4357/aa7edb. arXiv: 1707.02321 [astro-ph.EP].

Pinilla, P. et al. (May 2021). "A bright inner disk and structures in the transition disk around the very low-mass star CIDA 1". In: 649, A122, A122. DOI: 10.1051/0004-6361/202140371. arXiv: 2103.10465 [astro-ph.EP].

Pinilla, Paola (Nov. 2022). "First steps of planet formation around very low mass stars and brown dwarfs". In: *European Physical Journal Plus* 137.11,

1206, p. 1206. DOI: 10.1140/epjp/s13360-022-03384-1. arXiv: 2210. 06560 [astro-ph.EP].

Pinilla, Paola, Ilaria Pascucci, and Sebastian Marino (Mar. 2020). "Hints on the origins of particle traps in protoplanetary disks given by the M_{dust} - $M_\star$ relation". In: 635, A105, A105. DOI: 10.1051/0004-6361/201937003. arXiv: 2001.11045 [astro-ph.EP].

Pinilla, Paola et al. (Dec. 2016). "Can dead zones create structures like a transition disk?" In: 596, A81, A81. DOI: 10.1051/0004-6361/201628441. arXiv: 1610.02044 [astro-ph.EP].

Pinte, C. et al. (Feb. 2020). "Nine Localized Deviations from Keplerian Rotation in the DSHARP Circumstellar Disks: Kinematic Evidence for Protoplanets Carving the Gaps". In: 890.1, L9, p. L9. DOI: 10.3847/2041-8213/ab6dda. arXiv: 2001.07720 [astro-ph.SR].

Piso, Ana-Maria A. and Andrew N. Youdin (May 2014). "On the Minimum Core Mass for Giant Planet Formation at Wide Separations". In: 786.1, 21, p. 21. DOI: 10.1088/0004-637X/786/1/21. arXiv: 1311.0011 [astro-ph.EP].

Pollack, James B. et al. (Nov. 1996). "Formation of the Giant Planets by Concurrent Accretion of Solids and Gas". In: 124.1, pp. 62–85. DOI: 10.1006/icar.1996.0190.

Price, Daniel J. et al. (June 2018). "Circumbinary, not transitional: on the spiral arms, cavity, shadows, fast radial flows, streamers, and horseshoe in the HD 142527 disc". In: 477.1, pp. 1270–1284. DOI: 10.1093/mnras/sty647. arXiv: 1803.02484 [astro-ph.SR].

Ratzka, T., R. Köhler, and Ch. Leinert (July 2005). "A multiplicity survey of the ρ Ophiuchi molecular clouds". In: 437.2, pp. 611–626. DOI: 10.1051/0004-6361:20042107. arXiv: astro-ph/0504593 [astro-ph].

Ray, T. et al. (Jan. 2007). "Toward Resolving the Outflow Engine: An Observational Perspective". In: *Protostars and Planets V*. Ed. by Bo Reipurth, David

Jewitt, and Klaus Keil, p. 231. DOI: `10.48550/arXiv.astro-ph/0605597`. arXiv: `astro-ph/0605597 [astro-ph]`.

Raymond, Sean N. and Alessandro Morbidelli (Jan. 2022). "Planet Formation: Key Mechanisms and Global Models". In: *Demographics of Exoplanetary Systems, Lecture Notes of the 3rd Advanced School on Exoplanetary Science*. Ed. by Katia Biazzo et al. Vol. 466. Astrophysics and Space Science Library, pp. 3–82. DOI: `10.1007/978-3-030-88124-5_1`. arXiv: `2002.05756 [astro-ph.EP]`.

Rebolo, R., M. R. Zapatero Osorio, and E. L. Martín (Sept. 1995). "Discovery of a brown dwarf in the Pleiades star cluster". In: 377.6545, pp. 129–131. DOI: `10.1038/377129a0`.

Reipurth, Bo and Cathie Clarke (July 2001). "The Formation of Brown Dwarfs as Ejected Stellar Embryos". In: 122.1, pp. 432–439. DOI: `10.1086/321121`. arXiv: `astro-ph/0103019 [astro-ph]`.

Riaz, B. and J. Bally (Mar. 2021). "Accretion and outflow activity in proto-brown dwarfs". In: 501.3, pp. 3781–3805. DOI: `10.1093/mnras/staa3905`. arXiv: `2012.08612 [astro-ph.SR]`.

Riaz, B. and M. N. Machida (July 2021). "Complex structure of a proto-brown dwarf". In: 504.4, pp. 6049–6066. DOI: `10.1093/mnras/stab547`. arXiv: `2102.09640 [astro-ph.SR]`.

Rice, W. K. M. et al. (Mar. 2003). "The effect of cooling on the global stability of self-gravitating protoplanetary discs". In: 339.4, pp. 1025–1030. DOI: `10.1046/j.1365-8711.2003.06253.x`. arXiv: `astro-ph/0211088 [astro-ph]`.

Rice, W. K. M. et al. (Dec. 2006). "Dust filtration at gap edges: implications for the spectral energy distributions of discs with embedded planets". In: 373.4, pp. 1619–1626. DOI: `10.1111/j.1365-2966.2006.11113.x`. arXiv: `astro-ph/0609808 [astro-ph]`.

Rich, Evan A. et al. (Sept. 2022). "Gemini-LIGHTS: Herbig Ae/Be and Massive T Tauri Protoplanetary Disks Imaged with Gemini Planet Imager".

In: 164.3, 109, p. 109. DOI: 10.3847/1538-3881/ac7be4. arXiv: 2206.05815
[astro-ph.EP].

Rosen, Anna L. and Mark R. Krumholz (Aug. 2020). "The Role of Outflows,
Radiation Pressure, and Magnetic Fields in Massive Star Formation". In:
160.2, 78, p. 78. DOI: 10.3847/1538-3881/ab9abf. arXiv: 2006.04829
[astro-ph.SR].

Rosotti, Giovanni P. et al. (July 2016). "The minimum mass of detectable plan-
ets in protoplanetary discs and the derivation of planetary masses from
high-resolution observations". In: 459.3, pp. 2790–2805. DOI: 10.1093/
mnras/stw691. arXiv: 1603.02141 [astro-ph.EP].

Ruíz-Rodríguez, D. et al. (Apr. 2017). "The ALMA early science view of FUor/EXor
objects - II. The very wide outflow driven by HBC 494". In: 466.3, pp. 3519–
3532. DOI: 10.1093/mnras/stw3378. arXiv: 1612.08799 [astro-ph.SR].

Ruíz-Rodríguez, D. et al. (Aug. 2018). "ALMA survey of circumstellar discs
in the young stellar cluster IC 348". In: 478.3, pp. 3674–3692. DOI: 10.
1093/mnras/sty1351. arXiv: 1805.07590 [astro-ph.SR].

Ruíz-Rodríguez, Dary A. et al. (Oct. 2022). "Discovery of a Brown Dwarf with
Quasi-spherical Mass Loss". In: 938.1, 54, p. 54. DOI: 10.3847/1538-4357/
ac8ff5. arXiv: 2209.00759 [astro-ph.SR].

Santamaría-Miranda, A. et al. (Aug. 2020). "Bipolar molecular outflow of the
very low-mass star Par-Lup3-4. Evidence for scaled-down low-mass star
formation". In: 640, A13, A13. DOI: 10.1051/0004-6361/202038128.
arXiv: 2006.03063 [astro-ph.SR].

Santamaría-Miranda, A. et al. (Feb. 2021). "ALMA observations of the early
stages of substellar formation in the Lupus 1 and 3 molecular clouds". In:
646, A10, A10. DOI: 10.1051/0004-6361/202039419. arXiv: 2012.03985
[astro-ph.GA].

Schöier, F. L. et al. (Apr. 2004). "On the origin of H_2CO abundance enhancements in low-mass protostars". In: 418, pp. 185–202. DOI: 10.1051/0004-6361:20035769. arXiv: astro-ph/0401635 [astro-ph].

Schwartz, R. D. (Feb. 1977). "Evidence of star formation triggered by expansion of the Gum Nebula." In: 212, pp. L25–L26. DOI: 10.1086/182367.

Segura-Cox, Dominique M. et al. (Oct. 2020). "Four annular structures in a protostellar disk less than 500,000 years old". In: 586.7828, pp. 228–231. DOI: 10.1038/s41586-020-2779-6. arXiv: 2010.03657 [astro-ph.EP].

Shirley, Yancy L. et al. (Feb. 2011). "Mustang 3.3 mm Continuum Observations of Class 0 Protostars". In: 141.2, 39, p. 39. DOI: 10.1088/0004-6256/141/2/39. arXiv: 1011.3817 [astro-ph.GA].

Shu, Frank H., Fred C. Adams, and Susana Lizano (Jan. 1987). "Star formation in molecular clouds: observation and theory." In: 25, pp. 23–81. DOI: 10.1146/annurev.aa.25.090187.000323.

Somigliana, Alice et al. (Aug. 2022). "On the time evolution of the M_d-$M_\star$ and -$M_\star$ correlations for protoplanetary discs: the viscous time-scale increases with stellar mass". In: 514.4, pp. 5927–5940. DOI: 10.1093/mnras/stac1587. arXiv: 2206.04136 [astro-ph.EP].

Stamatellos, Dimitris and Anthony P. Whitworth (Jan. 2009). "The properties of brown dwarfs and low-mass hydrogen-burning stars formed by disc fragmentation". In: 392.1, pp. 413–427. DOI: 10.1111/j.1365-2966.2008.14069.x. arXiv: 0810.1687 [astro-ph].

Strom, Karen M. et al. (May 1989). "Circumstellar Material Associated with Solar-Type Pre-Main-Sequence Stars: A Possible Constraint on the Timescale for Planet Building". In: 97, p. 1451. DOI: 10.1086/115085.

Takami, Michihiro et al. (Sept. 2018). "Near-infrared High-resolution Imaging Polarimetry of FU Ori-type Objects: Toward a Unified Scheme for Low-mass Protostellar Evolution". In: 864.1, 20, p. 20. DOI: 10.3847/1538-4357/aad2e1. arXiv: 1807.03499 [astro-ph.SR].

Takami, Michihiro et al. (Oct. 2019). "An ALMA Study of the FU Ori-type Object V900 Mon: Implications for the Progenitor". In: 884.2, 146, p. 146. DOI: 10.3847/1538-4357/ab43c8. arXiv: 1909.05520 [astro-ph.SR].

Tan, J. C. et al. (Jan. 2014). "Massive Star Formation". In: *Protostars and Planets VI*. Ed. by Henrik Beuther et al., pp. 149–172. DOI: 10.2458/azu_uapress_9780816531240-ch007. arXiv: 1402.0919 [astro-ph.GA].

Tarter, J. C. (Sept. 1976). "Brown Dwarfs, Lilliputian Stars, Giant Planets and Missing Mass Problems." In: *Bulletin of the American Astronomical Society*. Vol. 8, p. 517.

Teague, Richard and Daniel Foreman-Mackey (Sept. 2018). "A Robust Method to Measure Centroids of Spectral Lines". In: *Research Notes of the American Astronomical Society* 2, 173, p. 173. DOI: 10.3847/2515-5172/aae265.

Testi, L. et al. (Oct. 2016). "Brown dwarf disks with ALMA: Evidence for truncated dust disks in Ophiuchus". In: 593, A111, A111. DOI: 10.1051/0004-6361/201628623. arXiv: 1606.06448 [astro-ph.SR].

Tobin, John J. et al. (Mar. 2012). "Complex Structure in Class 0 Protostellar Envelopes. III. Velocity Gradients in Non-axisymmetric Envelopes, Infall, or Rotation?" In: 748.1, 16, p. 16. DOI: 10.1088/0004-637X/748/1/16. arXiv: 1201.2174 [astro-ph.GA].

Tobin, John J. et al. (Feb. 2020). "The VLA/ALMA Nascent Disk and Multiplicity (VANDAM) Survey of Orion Protostars. II. A Statistical Characterization of Class 0 and Class I Protostellar Disks". In: 890.2, 130, p. 130. DOI: 10.3847/1538-4357/ab6f64. arXiv: 2001.04468 [astro-ph.GA].

Toomre, A. (May 1964). "On the gravitational stability of a disk of stars." In: 139, pp. 1217–1238. DOI: 10.1086/147861.

Tsukamoto, Y. et al. (July 2023). "The Role of Magnetic Fields in the Formation of Protostars, Disks, and Outflows". In: *Protostars and Planets VII*. Ed. by S. Inutsuka et al. Vol. 534. Astronomical Society of the Pacific Conference Series, p. 317.

van der Marel, N. et al. (Aug. 2013). "Outflow forces of low-mass embedded objects in Ophiuchus: a quantitative comparison of analysis methods". In: 556, A76, A76. DOI: 10.1051/0004-6361/201220717. arXiv: 1305.6453 [astro-ph.SR].

van der Marel, Nienke (Mar. 2023). "Transition disks: the observational revolution from SEDs to imaging". In: *European Physical Journal Plus* 138.3, 225, p. 225. DOI: 10.1140/epjp/s13360-022-03628-0. arXiv: 2210.05539 [astro-ph.EP].

van't Hoff, Merel L. R. et al. (July 2023). "Early Planet Formation in Embedded Disks (eDisk). III. A First High-resolution View of Submillimeter Continuum and Molecular Line Emission toward the Class 0 Protostar L1527 IRS". In: 951.1, 10, p. 10. DOI: 10.3847/1538-4357/accf87. arXiv: 2306.15407 [astro-ph.EP].

Vázquez-Semadeni, Enrique et al. (Dec. 2019). "Global hierarchical collapse in molecular clouds. Towards a comprehensive scenario". In: 490.3, pp. 3061–3097. DOI: 10.1093/mnras/stz2736. arXiv: 1903.11247 [astro-ph.GA].

Vazzano, M. M. et al. (Apr. 2021). "Outflows, envelopes, and disks as evolutionary indicators in Lupus young stellar objects". In: 648, A41, A41. DOI: 10.1051/0004-6361/202039228. arXiv: 2101.05330 [astro-ph.SR].

Velusamy, T., W. D. Langer, and T. Thompson (Mar. 2014). "HiRes Deconvolved Spitzer Images of 89 Protostellar Jets and Outflows: New Data on the Evolution of the Outflow Morphology". In: 783.1, 6, p. 6. DOI: 10.1088/0004-637X/783/1/6. arXiv: 1312.0978 [astro-ph.SR].

Wada, Koji et al. (May 2007). "Numerical Simulation of Dust Aggregate Collisions. I. Compression and Disruption of Two-Dimensional Aggregates". In: 661.1, pp. 320–333. DOI: 10.1086/514332.

— (Apr. 2008). "Numerical Simulation of Dust Aggregate Collisions. II. Compression and Disruption of Three-Dimensional Aggregates in Head-on Collisions". In: 677.2, pp. 1296–1308. DOI: 10.1086/529511.

Ward-Thompson, D. et al. (May 1994). "A Submillimetre Continuum Survey of Pre Protostellar Cores". In: 268, p. 276. DOI: 10.1093/mnras/268.1.276.

White, Jacob Aaron et al. (Apr. 2017). "1.3-mm ALMA observations of the Fomalhaut debris system". In: 466.4, pp. 4201–4210. DOI: 10.1093/mnras/stw3303. arXiv: 1612.01648 [astro-ph.EP].

Whitworth, A. P. and H. Zinnecker (Nov. 2004). "The formation of free-floating brown dwarves and planetary-mass objects by photo-erosion of prestellar cores". In: 427, pp. 299–306. DOI: 10.1051/0004-6361:20041131. arXiv: astro-ph/0408522 [astro-ph].

Wilking, B. A., M. Gagné, and L. E. Allen (2008). "Star Formation in the ρ Ophiuchi Molecular Cloud". In: *Handbook of Star Forming Regions, Volume II*. Vol. 5, p. 351. DOI: 10.48550/arXiv.0811.0005.

Williams, Jonathan P. and William M. J. Best (June 2014). "A Parametric Modeling Approach to Measuring the Gas Masses of Circumstellar Disks". In: 788.1, 59, p. 59. DOI: 10.1088/0004-637X/788/1/59. arXiv: 1312.0151 [astro-ph.EP].

Williams, Jonathan P. et al. (Apr. 2019). "The Ophiuchus DIsk Survey Employing ALMA (ODISEA): Disk Dust Mass Distributions across Protostellar Evolutionary Classes". In: 875.2, L9, p. L9. DOI: 10.3847/2041-8213/ab1338. arXiv: 1904.06471 [astro-ph.SR].

Winter, Andrew J., Richard A. Booth, and Cathie J. Clarke (Oct. 2018). "Evidence of a past disc-disc encounter: HV and DO Tau". In: 479.4, pp. 5522–5531. DOI: 10.1093/mnras/sty1866. arXiv: 1807.04295 [astro-ph.SR].

Woon, David E. (Apr. 2002). "Modeling Gas-Grain Chemistry with Quantum Chemical Cluster Calculations. I. Heterogeneous Hydrogenation of CO and H_2CO on Icy Grain Mantles". In: 569.1, pp. 541–548. DOI: 10.1086/339279.

Wyatt, M. C. et al. (June 2015). "Five steps in the evolution from protoplanetary to debris disk". In: 357.2, 103, p. 103. DOI: 10.1007/s10509-015-2315-6. arXiv: 1412.5598 [astro-ph.EP].

Zhang, Ke (Jan. 2015). "Volatiles in Protoplanetary Disks". PhD thesis. California Institute of Technology.

Zhang, M. et al. (May 2013). "Proper motions of molecular hydrogen outflows in the ρ Ophiuchi molecular cloud". In: 553, A41, A41. DOI: 10.1051/0004-6361/201220342. arXiv: 1304.0195 [astro-ph.SR].

Zhang, Yichen et al. (Dec. 2016). "ALMA Cycle 1 Observations of the HH46/47 Molecular Outflow: Structure, Entrainment, and Core Impact". In: 832.2, 158, p. 158. DOI: 10.3847/0004-637X/832/2/158. arXiv: 1602.02388 [astro-ph.SR].

Zhu, Zhaohuan et al. (Feb. 2012). "Challenges in Forming Planets by Gravitational Instability: Disk Irradiation and Clump Migration, Accretion, and Tidal Destruction". In: 746.1, 110, p. 110. DOI: 10.1088/0004-637X/746/1/110. arXiv: 1111.6943 [astro-ph.SR].

Zinnecker, Hans, Mark J. McCaughrean, and John T. Rayner (Aug. 1998). "A symmetrically pulsed jet of gas from an invisible protostar in Orion". In: 394.6696, pp. 862–865. DOI: 10.1038/29716.

Zucker, Catherine et al. (July 2019). "A Large Catalog of Accurate Distances to Local Molecular Clouds: The Gaia DR2 Edition". In: 879.2, 125, p. 125. DOI: 10.3847/1538-4357/ab2388. arXiv: 1902.01425 [astro-ph.GA].

Zurlo, Alice et al. (Aug. 2020). "The Ophiuchus DIsc Survey Employing ALMA (ODISEA) - II. The effect of stellar multiplicity on disc properties". In: 496.4, pp. 5089–5100. DOI: 10.1093/mnras/staa1886. arXiv: 2006.16259 [astro-ph.SR].